



저작자표시-비영리-변경금지 2.0 대한민국

이용자는 아래의 조건을 따르는 경우에 한하여 자유롭게

- 이 저작물을 복제, 배포, 전송, 전시, 공연 및 방송할 수 있습니다.

다음과 같은 조건을 따라야 합니다:



저작자표시. 귀하는 원저작자를 표시하여야 합니다.



비영리. 귀하는 이 저작물을 영리 목적으로 이용할 수 없습니다.



변경금지. 귀하는 이 저작물을 개작, 변형 또는 가공할 수 없습니다.

- 귀하는, 이 저작물의 재이용이나 배포의 경우, 이 저작물에 적용된 이용허락조건을 명확하게 나타내어야 합니다.
- 저작권자로부터 별도의 허가를 받으면 이러한 조건들은 적용되지 않습니다.

저작권법에 따른 이용자의 권리는 위의 내용에 의하여 영향을 받지 않습니다.

이것은 [이용허락규약\(Legal Code\)](#)을 이해하기 쉽게 요약한 것입니다.

[Disclaimer](#)

공학박사학위논문

상대습도가 천음속 압축기 캐스케이드
공력 성능에 미치는 영향

Humidity Effects on the Aerodynamic Performance of
a Transonic Compressor Cascade

2019 년 8 월

서울대학교 대학원

기계항공공학부

이재민

Abstract

Gas turbines which operate in the humid condition experience performance change. In the previous researches, the properties of working fluid change, an inlet duct condensation, and stage mismatching are discussed for the reasons of the gas turbine performance change. However, understandings of the compressor flow field change due to humidity (ex. condensation & evaporation) are still lacking.

This study has been conducted to investigate the humidity effects on the transonic compressor flow field. For an experimental study, a transonic wind tunnel has been built, and the cascade device has been adopted to investigate compressor flow field. For six different relative humidity (RH) conditions (20, 32, 42, 45, 49, 53%), transonic compressor cascade performance has been investigated by measuring blade pressure coefficient distribution, deviation distribution, and loss coefficient distribution at a Mach number 1.11, and incidence of $+5^\circ$. As relative humidity increases, pressure coefficients on the suction surface have been increased due to condensation, shock has been shifted downstream, and the mass averaged loss coefficient have been increased up to 29% at 53% RH condition due to thermodynamic loss. However, there are negligible effects on the deviation. Numerical study has been conducted for the detailed understandings of the experimental results. To simulate the non-equilibrium condensation/evaporation phenomenon in a transonic flow field, the Classical Nucleation Theory (CNT), and the Hertz-Knudsen droplet growth model has been adopted, and applied to the commercial program of ANSYS FLUENT v. 17.0. The effects of humidity on the pressure coefficient on the blade, and the shock location shift have been verified due

to condensation, and the latent heat addition thereby. By comparing the loss coefficient evolution following a streamline, decreasing shock loss and increasing thermodynamic loss have been captured as relative humidity increases. However, as thermodynamic loss increases at a faster rate than decreasing rate of shock loss, the mass averaged loss coefficient has been increased as relative humidity increases.

Keyword: Transonic compressor, Cascade, Aerodynamic performance, Humidity, Non-equilibrium condensation.

Student Number: 2013-20697

Table of Contents

Abstract	i
List of Figures	v
List of Tables	ix
Nomenclatures	x
Chapter 1. Introduction	1
1.1. Transonic compressor cascade aerodynamic characteristics	1
1.2. Literature review	1 0
1.3. Motivation and Research Objectives	2 5
1.4. Thesis Organization	2 7
Chapter 2. Physics of Condensation	2 8
2.1 Introduction	2 8
2.2 Condensation	2 9
2.3 Governing equations	3 7
2.4 Material properties	4 5
Chapter 3. Experimental Facility	5 0
3.1 Transonic compressor cascade tunnel	5 0
3.2. Transonic wind tunnel	5 0
3.3. Test section	5 4
3.4. Test blade	5 6
3.5. Instrumentation	5 7
3.6. Wind tunnel flow quality	6 1
Chapter 4. Experimental Results	6 8
4.1 Test matrix	6 8
4.2 Cascade flow quality	6 8
4.3 Blade loading distribution	7 2
4.4 Deviation	7 6
4.5 Loss coefficient	7 8
Chapter 5. Numerical Method	8 2
5.1 Introduction	8 2
5.2 Mesh construction	8 2
5.3 Solver setting	8 4
5.4 Strategy of condensation modelling	8 5
5.5 Validation of Numerical Method	8 7

Chapter 6. Numerical Results	9 0
6.1 Introduction	9 0
6.2 Validation Results	9 1
6.3 Blade loading distribution	9 4
6.4 Deviation	1 0 0
6.5 Loss coefficient	1 0 4
Chapter 7. Conclusions	1 1 2
7.1 Summary	1 1 2
7.2 Recommendations	1 1 3
References	1 1 5
Appendix A. Test Facility	1 2 2
Appendix B. Instrumentation	1 3 3
Appendix C. 3-hole Probe Calibration	1 3 6
Appendix D. Uncertainty Analysis	1 4 2
Appendix E. Axial Velocity Density Ratio	1 4 4
Appendix F. Rayleigh Flow	1 4 6
Appendix G. The effects of vapor mass reduction on the static pressure field	1 4 7
Appendix H. Water injection rate	1 4 8
Appendix I. Limitations in capturing deviation distribution	1 4 9
요약 (국문초록)	1 5 1
감사의 글	1 5 3

List of Figures

Figure 1. 1. Applications of a gas turbine: (a) Aviation (GE Aviation), (b) Power plant (Mitsubishi Hitachi Power Systems).	2
Figure 1. 2. Gas turbine operation in a humid condition: (a) inlet fogging device in power plant application, (b) condensation at engine inlet duct.	3
Figure 1. 3. Type of compressor: (a) axial compressor, (b) centrifugal compressor.	4
Figure 1. 4. Velocity triangle for a stage of axial compressor.	6
Figure 1. 5. Flow characteristics of a transonic compressor cascade.....	7
Figure 1. 6. Cascade notations.	9
Figure 1. 7. Humidity correction factor: (a) compressor speed, (b) fuel flow, (c) Turbine inlet temperature, (d) trust.	1 3
Figure 1. 8. Effects of humidity on engine performance.	1 4
Figure 1. 9. JT9D-7 engine test: (a) atmospheric condition, (b) specific fuel consumption rise.	1 5
Figure 1. 10. Compressor map shift due to re-evaporation.	1 7
Figure 1. 11. Interferograms for the laval nozzle flow of a mixture of water vapor and air, a) absolute humidity 4g/kg, b) absolute humidity 8g/kg.	1 8
Figure 1. 12. Density distributions along the nozzle axis for different condensation models.	1 9
Figure 1. 13. Isentropic Mach number distribution over the bump at inlet Mach number 0.8.	2 0
Figure 1. 14. Schlieren images of shock waves over the bump: (a) RH= 50%, (b) RH= 44%, (c) RH= 38%, (d) RH=32%.	2 0
Figure 1. 15 Condensation effects on the aerodynamic performance of a airfoil: (a) lift coefficient, (b) drag coefficient.	2 1
Figure 1. 16. Condensation effects on Mach number contour: (a) dry, (b) RH 80%.	2 3
Figure 1. 17. Condensation effects on the pressure coefficient distribution.	2 3
Figure 1. 18. Humidity effects on the compressor cascade aerodynamic characteristics: (a) isentropic Mach number distribution, (b) loss coefficient.	2 4
Figure 2. 1 P-T diagram of water.	2 8
Figure 2. 2. Non-equilibrium condensation in F-18 aircraft.	2 9
Figure 2. 3. Free energy of forming a cluster with n molecules.	3 2
Figure 2. 4. Surface tension of liquid water and its extrapolations.	4 6
Figure 2. 5. Liquid density of water.	4 8

Figure 2. 6. Equilibrium vapor pressure of water.....	4 9
Figure 3. 1. A new transonic cascade wind tunnel.	5 0
Figure 3. 2. Schematic of wind tunnel.....	5 2
Figure 3. 3. Schematic of water supply system	5 3
Figure 3. 4. Test section: (a) picture, (b) schematic.	5 5
Figure 3. 5. Test blades.	5 6
Figure 3. 6. Schematic of Schlieren device.	6 0
Figure 3. 7. Static tap location.	6 2
Figure 3. 8. Flow quality at the nozzle inlet & outlet: (a) Ma=0.6, (b) Ma=1.0.	6 4
Figure 3. 9. Measurements location at test section.	6 5
Figure 3. 10. Span wise Mach number distribution at test section: (a) Ma=0.6 (b) Ma=1.0.	6 6
Figure 3. 11. Spanwise normalized total pressure distribution at test section: (a) Ma=0.6 (b) Ma=1.0.	6 7
Figure 4. 1. Inlet periodicity.....	6 9
Figure 4. 2. Outlet periodicity.....	7 0
Figure 4. 3. Pressure coefficient distribution vs. axial location.	7 4
Figure 4. 4. Schlieren images: (a) RH= 20%, (b) RH=32%, (c) RH= 42%, (d) RH= 45%, (e) RH= 49% (f) RH= 53%.	7 6
Figure 4. 5. Mid-span deviation distribution vs. pitch at $x/C_x=1.4$	7 7
Figure 4. 6. Mid-span loss coefficient distribution vs. pitch at $x/C_x=1.4$	7 9
Figure 4. 7. Loss composition.	8 1
Figure 5. 1. Mesh.....	8 3
Figure 5. 2. Grid independence test.	8 4
Figure 5. 3. Calculation strategy.....	8 7
Figure 5. 4. Mesh geometry – NACA0012.	8 8
Figure 5. 5. Nucleation rate distribution at 50% RH condition.	8 9
Figure 5. 6. Pressure coefficient distribution (RH= 0, 50%).	8 9
Figure 6. 1. CFD validation results - pressure coefficient distributions.	9 2
Figure 6. 2. CFD validation results - deviation distribution.	9 3
Figure 6. 3. CFD validation results - loss coefficient distribution.	9 4
Figure 6. 4. CFD result – pressure coefficient distribution vs axial chord wise location.	9 7
Figure 6. 5. CFD result – condensate mass fraction contour: (a) RH=20%, (b) RH=32%, (c) RH=42%, (d) RH=45%, (e) RH=49%, (f) RH = 53%.	9 9
Figure 6. 6. CFD result – deviation distribution vs pitch-wise location	

.....	1 0 1
Figure 6. 7. CFD result – Mach number contour: (a) RH=20%, (b) RH=32%, (c) RH=42%, (d) RH=45%, (e) RH=49%, (f) RH = 53%.	1 0 3
.....	1 0 3
Figure 6. 8. CFD result – loss coefficient distribution vs pitch-wise location.....	1 0 5
Figure 6. 9. CFD result – entropy contours: (a) RH= 20%, (b) RH= 32%, (c) RH= 42%, (d) RH= 45%, (e) RH= 49%, (f) RH= 53%.	1 0 7
Figure 6. 10. CFD result – loss coefficient evolution following a streamline.	1 1 0
.....	1 1 0
Figure 6. 11. Cascade loss composition.	1 1 1
Figure A. 1. Schematic of transonic wind tunnel.	1 2 2
Figure A. 2. Pressure regulator.	1 2 3
Figure A. 3. Pressure valve.	1 2 3
Figure A. 4. Inlet duct.	1 2 4
Figure A. 5. Water nozzles.	1 2 4
Figure A. 6. Inlet diffuser.	1 2 5
Figure A. 7. Settling chamber,	1 2 5
Figure A. 8. Test section,	1 2 6
Figure A. 9. Throttle valve,	1 2 6
Figure A. 10. Silencer.	1 2 7
Figure A. 11. Schematic of test section.	1 2 8
Figure A. 12. Test section.	1 2 8
Figure A. 13. Supersonic nozzle.	1 2 9
Figure A. 14. Schematic of sidewall boundary layer bleeding slot.	1 2 9
Figure A. 15. Schematic of transonic wall	1 3 0
Figure A. 16. Lower bypass flow valve.	1 3 0
Figure A. 17. Upper bypass flow valve.	1 3 1
Figure A. 18. Sidewall boundary layer bleeding flow valve.	1 3 1
Figure A. 19. Transonic wall flow valve.	1 3 2
Figure A. 20. Light source & parabolic mirror.	1 3 4
Figure A. 21. Parabolic mirror.	1 3 4
Figure A. 22. Plane mirror.	1 3 5
Figure A. 23. Camera & Knife edge.	1 3 5
Figure A. 24. 3-hole probe geometry	1 3 6
Figure A. 25. Flow angle vs. flow angle coefficient (Ma=0.6).	1 3 7
Figure A. 26. Flow angle vs. flow angle coefficient (Ma=0.8).	1 3 7
Figure A. 27. Flow angle vs. flow angle coefficient (Ma=0.95).	1 3 8
Figure A. 28. C_t vs. C_b (Ma=0.6).	1 3 9

Figure A. 29. C_t vs. C_b (Ma=0.8).....	1 3 9
Figure A. 30. C_t vs. C_b (Ma=0.95).....	1 4 0
Figure A. 31. C_s vs. C_b (Ma=0.6).....	1 4 0
Figure A. 32. C_s vs. C_b (Ma=0.8).....	1 4 1
Figure A. 33. C_s vs. C_b (Ma=0.95).....	1 4 1
Figure A. 35. Control volume.....	1 4 7
Figure A. 34. Re-constructed mesh.	1 4 9
Figure A. 35. Deviation distributions for the EXP, and CFD results of reference mesh, new-mesh, and high incidence angle ($i = +6^\circ$)....	1 5 0

List of Tables

Table 1. 1. Cascade parameters	9
Table 1. 2. Cascade performance parameters	1 0
Table 2. 1. Constants for liquid density equation	4 8
Table 2. 2. Constants for equilibrium vapor pressure	4 8
Table 3. 1. Blade geometry parameters	5 6
Table 3. 2. Data reduction	5 7
Table 3. 3. Measurement variables and method	5 8
Table 3. 4. Uncertainty of measurement variables	6 1
Table 3. 5. Location of static taps	6 3
Table 3. 6. Location of static/total pressure measurement	6 5
Table 4. 1. Test conditions	6 8
Table 4. 2. AVDR values	7 1
Table 4. 3. Mass averaged deviation	7 7
Table 4. 4. Normalized wake displacement thickness	7 8
Table 4. 5. Mass averaged loss coefficient	8 0
Table 5. 1. Boundary condition	8 5
Table 5. 2. Inlet conditions	8 8
Table 6. 1. Shock strength	1 0 0
Table 6. 2. Mass averaged deviation	1 0 1
Table 6. 3. Mass-averaged loss coefficient	1 0 5
Table 6. 4. CFD results - Contribution of each loss in percentage.	1 1 0
Table A. 1. Blade static tap location	1 3 3
Table A. 2. Heat addition effects on flow properties	1 4 6
Table A. 3. The effects of condensation on the flow properties	1 4 7
Table A. 4. Water injection rate	1 4 8

Nomenclatures

Symbols

a_0	Molecular surface are [m^2]
C	Absolute velocity, [m/s]
c	Chord length
C_p	Pressure coefficient, $\frac{P-\overline{P_{s,1}}}{P_t-\overline{P_{s,1}}}$
c_p	Isobaric specific heat constant, [J/(K · kg)]
c_v	Isochoric specific heat constant, [J/(K · kg)]
e	Specific internal energy, J/kg]
G	Gibbs energy, [J]
g	Condensate mass fraction, $\frac{M_l}{M}$
H	Wind tunnel height
h	Specific enthalpy, [J/kg]
i	Incidence angle, [°]
J	Nucleation rate, [# of nuclei/(s, m^3)]
k_B	Boltzmann constant, 1.38×10^{-23} [$m^2 kgs^{-2} T^{-1}$]
Kn	Knudsen number, $l/2r$
L	Latent heat, [J]
l	Length of mean free path, [m]
M	Mass
Ma	Mach number
\dot{m}	Mass flow rate, [kg/s]
n	Number of molecules
N_A	Avogadro's number, 6.02×10^{23} [mol^{-1}]
P	Pressure, [Pa]
R	Gas constant
Q_i	Auxiliary parameter, $\rho Q_i = \int_{-\infty}^t \rho(t)r(t,\tau)^n J(\tau)/\rho(\tau) dt$
RH	Relative humidity
r	Droplet radius, [m]
S	Pitch length
s	Supersaturation rate, $\frac{P_v}{P_{v,eq}}$
T	Temperature, [K]
t	time, [s]
U	Rotational speed [m/s]
u	Cartesian velocity component in x-direction, [m/s]
V	Volume, [m^3]
v	Cartesian velocity component in y-direction, [m/s]
v	Velocity, [m/s]
v_l	Liquid molecular volume, [m^3]
W	Relative velocity
w	Cartesian velocity component in z-direction, [m/s]
Y_p	Loss coefficient, $\frac{\Delta P_t}{P_t-\overline{P_{s,1}}}$
Z	Blade span

Greek

α	Inlet flow angle, [$^{\circ}$]
β	Blade metal angle, [$^{\circ}$]
γ	Specific heat ratio
δ	Deviation, [$^{\circ}$]
θ	Dimensionless surface tension, $\sigma a_0/k_B T$
ρ	Density, [kg/m^3]
ϱ	Density, material property, [kg/m^3]
σ	Surface tension, [N/m]
τ	Shear stress, [N/m]
\emptyset	Diameter, [m]
Ω	Rotational speed [rad/s]

Subscript

0	Stagnation quantity
1	Inlet quantity
2	Outlet quantity
a	Air
C	Critical value
d	Droplet
eq	Equilibrium condition
l	Liquid
max	Maximum
n	n molecules
r	Droplet radius
s	Static quantity
t	Total quantity
Tr	Triple point
v	Vapor
θ	Tangential quantity
x,y,z	Cartesian component

Superscript

*	Critical value
---	----------------

Chapter 1. Introduction

1.1. Transonic compressor cascade aerodynamic characteristics

1.1.1. A gas turbine operates in a humid condition

A gas turbine is a device for producing power which consists of a compressor, a combustor, and a turbine. In the compressor part, as a first part of a gas turbine, ambient air is sucked, and mechanical energy is transferred to it. Depending on the application, the air is pressurized up to 40 bar by multi-staged compressor. Downstream of the compressor, pressurized air enters the combustor. In this part, combustion occurs, thus, chemical energy is transferred to the air. In the modern gas turbines, to get a higher thermal efficiency, the temperature of working fluid reaches about 1900K, and even higher. This high-pressure and high-temperature working fluid enters the turbine transferring its energy to the turbine blade in form of mechanical work. Some of the extracted energy is used to drive a compressor, and the remaining energy is used differently depending on the applications. If the gas turbine is to be used in the power plant, another shaft is connected to the generator, thus, the remaining energy is used for power generation. If the gas turbine is to be used in the aircraft, a nozzle is located downstream of the turbine generating the thrust.

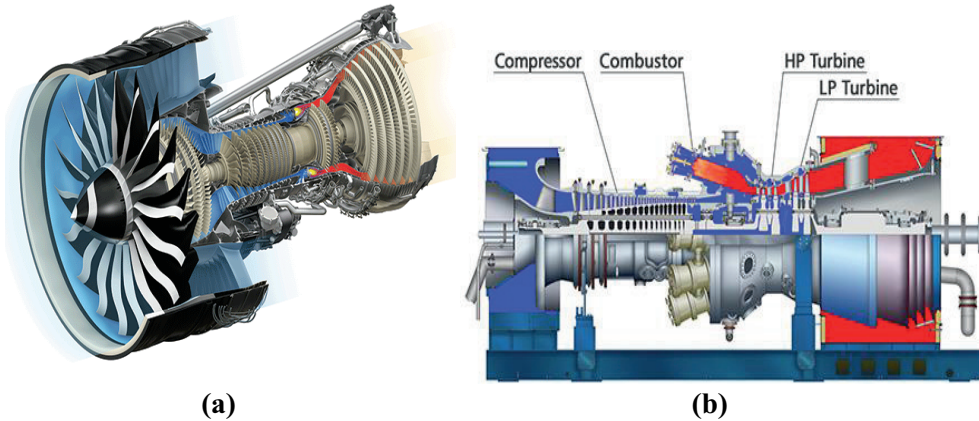


Figure 1.1. Applications of a gas turbine: (a) Aviation (GE Aviation), (b) Power plant (Mitsubishi Hitachi Power Systems).

Since a gas turbine sucks the ambient air and uses it as a working fluid, atmospheric conditions affects the gas turbine performance. Especially, a gas turbine power output is susceptible to the ambient air temperature which brings about the power declining 0.5 ~ 0.9% for every 1 °C rise [1]. Thus, to solve the power reduction problem during the gas turbine operation in high ambient temperature, for a power plant application, various cooling technics are adopted, such as an inlet fogging and a wet compression. These cooling technics make use of injecting water into the air using water droplets' evaporation to cool down the air temperature. It has been discovered that water spraying in the gas turbine inlet can effectively enhance power output by decreasing the inlet temperature [2 ~ 7]. These methods of injecting water droplets at gas turbine inlet are divided by inlet fogging [8, 9] and wet compression [10, 11] depending on the presence of water droplets in the compressor. Therefore, for a gas turbine adopting these cooling technics operates in highly humid condition. On the other hand, for a gas turbine applied to the aircraft, operation in humid condition frequently occurs due to weather condition, such as rain, and storm.

Figure 1.2 shows the examples of gas turbine operation in a humid condition both for power plant and aviation.



(a)



(b)

Figure 1. 2. Gas turbine operation in a humid condition: (a) inlet fogging device in power plant application, (b) condensation at engine inlet duct.

1.1.2. Transonic axial compressor

The compressor is the first part of a gas turbine where the sucked air meets. Therefore, the compressor performance is directly affected by the air condition. The compressor compress its working fluid by acceleration by a row of rotating blades called rotor, and then by diffusion in a row of stationary blades called stator. The type of compressor is divided into two types according to the direction of flow (Figure 1.3). A compressor of the type in which the flow enters the axial direction of the compressor and then goes out in the axial direction is called an axial compressor, and is called a centrifugal compressor when the flow comes in the axial direction and then goes out in the radial direction. In axial compressors, pressure ratio per stage is lower than that of centrifugal compressors, but it is widely used in power generation and aviation fields because it has larger flow rate, and it is easy to construct with multiple stages.

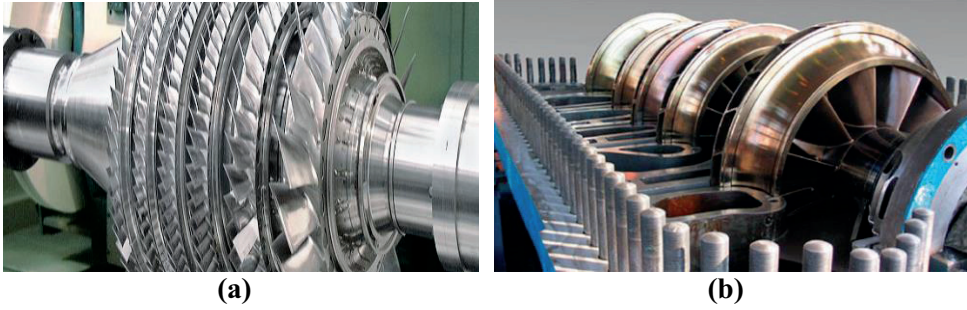


Figure 1. 3. Type of compressor: (a) axial compressor, (b) centrifugal compressor.

In the modern gas turbine industry, the compressor design is continuously pushing the current design limits. Engine companies want to produce an engine that are stronger, lighter, and has a greater efficiency. Especially in aviation engine, engine weight is an important factor. Thus, in the modern gas turbine, the compressor is designed for higher loading at greater efficiency. Higher loading implies less stages for a given pressure ratio, which results in producing lighter compressor, thereby helping to increase the engine thrust to weight ratio. Two ways to achieve higher pressure ratios with a fewer stages are illustrated in Equation 1.1 which is referred as Euler turbine equation.

$$\frac{Work}{\dot{m}} = \Delta h_0 = \Omega((rv_\theta)_2 - (rv_\theta)_1) \quad (0.1)$$

The specific work of the compressor ($Work/\dot{m}$) is proportional to both the amount of flow turning (Δrv_θ) and compressor shaft speed (Ω). Thus, to get a higher stage pressure ratio compressor, shaft speed and flow turning have to be increased. However, in the compressor flow field, due to the adverse pressure gradient and

aerodynamic loss, there are limits in flow turning. On the other hand, as the shaft speed increases, the flow of the rotor along the span changes from a relative subsonic to a relative supersonic. The compressor which exhibits relative supersonic inlet flow at the tip and relative subsonic inlet flow at the hub is called transonic compressor [12]. The shock structure in the relative supersonic inlet flow is a unique characteristic

1.1.3. Blade to blade flow

To get clear understandings of flow in a compressor, the flow field can be expressed by velocity triangles as in Figure 1.4. The fluid enters the rotor with an absolute velocity, C_1 , and has an angle, α_1 , from the axial direction. Combining the absolute velocity with the blade speed, U , gives the relative velocity, W_1 , with its relative angle, β_1 . The mechanical energy from the rotating rotors will be transferred to the working fluid. This energy will increase the absolute velocity of the fluid. After leaving the rotor, the fluid will have a relative velocity, W_2 , with a relative angle, β_2 , determined by the blade outlet angle. The fluid leaving the rotor is the fluid entering the stator, thus, the velocity triangle can be drawn similar to as in the rotor. Here, the relative velocity, W_2 will be diffused and leaving the stator with a velocity, C_3 at an angle of α_3 .

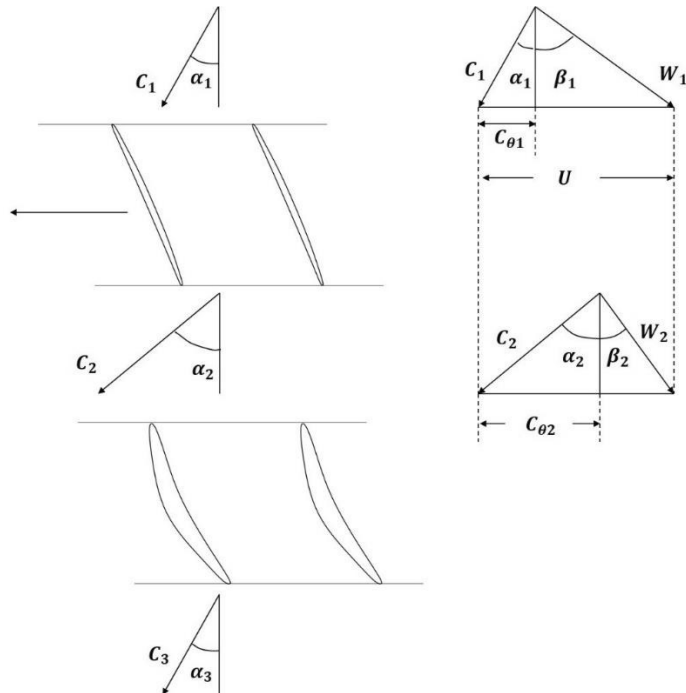


Figure 1. 4. Velocity triangle for a stage of axial compressor.

For a supersonic inlet flow (ex. flow in the blade tip region of a transonic compressor), a shock structure is a unique feature. Figure 1.5 shows a shock structure in a transonic compressor cascade flow at inlet Mach number of 1.2. First of all, due to the supersonic inlet flow, bow shock occurs upstream of leading edge. Downstream of the bow shock, flow accelerates following the suction surface and meets a passage shock which is connected to the bow shock. The passage shock is a main shock which makes a pressure rise, thus, downstream of the passage shock, flow diffuses to subsonic. Because the shock introduces an additional shock loss, and shock-induced boundary layer separation, there have been lots of studies which tried to understand the shock related flow characteristics in the compressor flow field, and the studies which tried to decrease the shock front Mach number by controlling the acceleration following the suction surface.



Figure 1. 5. Flow characteristics of a transonic compressor cascade.

1.1.4. Cascade flow field

For the researches about compressor flow field, traditionally, two methods have been adopted depending on the purpose of research. For example, for a research about compressor efficiency, unsteadiness effects of rotor, tip clearance flow, and stall, rig test (i.e. real or scale downed compressor) is adopted. However, there are limitations of difficulties of detailed flow field measurements and its expensive cost. Contrary to the rig test, cascade device is a non-rotating device which simulates the compressor flow field at a specific span location. Therefore, the detailed measurements are possible using a probe, hot-wire, or laser device (ex. LDV, PIV), and it is easy to control the independent variables which the researchers are interested in. Therefore, the cascade device is frequently adopted for the basic researches in turbomachinery.

In the cascade device, to simulate the compressor flow field, which shows periodic inlet & outlet flow, cascade is designed with many blades. Gostelow [13]

recommended more than 7 blades for cascade experiments. However, depending on the dimensional limits or wind tunnel specifications, the cascade composed of 4 blades is often used. The cascade is a stationary device, thus, to make a compressor inlet flow, the relative velocity in Figure 1.4 is given at the cascade inlet. Figure 1.6 shows the cascade parameters and Table 1.1 describes the definition of that. The inlet flow comes with velocity same as W_1 in Figure 1.4. In the conventional cascade notations, flow angles are described by the incidence and deviation. The incidence angle, i , is defined as the flow angle difference between inlet flow angle, α_1 , and the blade camber angle at the leading edge, β_1 . The deviation, δ is defined by the flow angle difference between outlet flow angle, α_2 , and blade camber angle at the trailing edge, β_2 . The other geometry parameter, stagger angle, γ , is same as target compressor geometry, however, the scale of chord, c , and pitch length, S , can be changed keeping its ratio constant. Its ratio is called solidity, c/S .

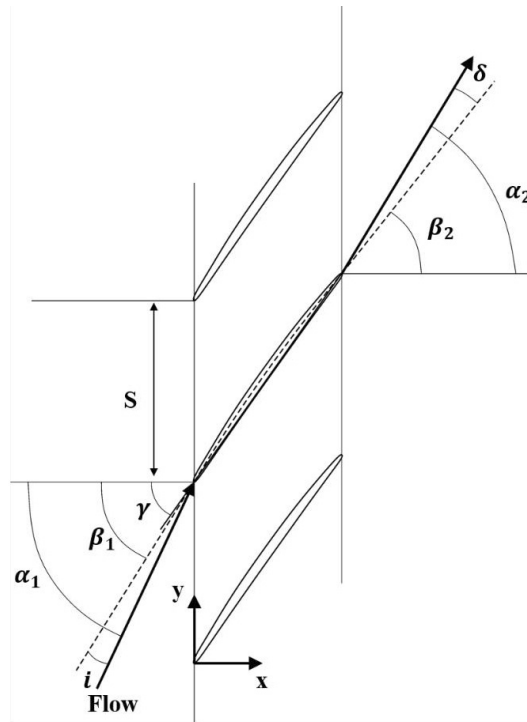


Figure 1. 6. Cascade notations.

Table 1. 1. Cascade parameters

Parameters	Definition
Incidence angle, i	$i = \alpha_1 - \beta_1$
Deviation, δ	$\delta = \alpha_2 - \beta_2$

1.1.5. Cascade performance parameters

Cascade device is usually used for the investigation of flow field of newly designed blade geometry or for the basic researches about effects of Reynolds number, roughness, turbulence intensity and humidity. These effects on the compressor cascade flow field can be categorized as cascade performance parameters which are directly used in designing a compressor blade: blade pressure coefficient distribution, loss coefficient, and deviation. Each definitions are listed in Table 1.2. The blade

pressure coefficient distribution represents the normalized pressure distribution on the blade surface. Therefore, from this information, the characteristics of flow field on the blade can be analyzed. The loss coefficient represents the total pressure reduction in the compressor passage, thus, it represents the aerodynamic loss which directly connected to the compressor efficiency. The deviation represents the flow angle difference from the blade metal angle, thus, it directly connected to the stage matching.

Table 1. 2. Cascade performance parameters

Parameters	Definition
Pressure coefficient	$C_p = \frac{P - \overline{P}_{s,1}}{P_t - \overline{P}_{s,1}}$
Loss coefficient	$Y_p = \frac{\Delta P_t}{P_t - \overline{P}_{s,1}}$
Deviation	$\delta = \alpha_2 - \beta_2$

1.2. Literature review

To understand the humidity effects on the transonic compressor cascade performance, various studies were performed. The previous studies are categorized into the humidity effects on the gas turbine engine performance, the humidity effects on the transonic flow field (nozzle, airfoil), and the humidity effects on the compressor cascade flow field.

1.2.1. Humidity effects on the gas turbine engine performance

The humidity effects on the gas turbine engine performance can be categorized by two points of view: i) the performance change due to the different gas properties, ii) the performance change due to the condensation at engine inlet.

The first effects of humidity on the gas turbine engine performance are come from the presence of water vapor in the air. Thereby, gas properties, such as specific heat C_p , gas constant R , and specific heat ratio γ , are changed. Samuels and Gale [14] derived correction factors based on the definition of the thermodynamic properties of humid air. They derived one-dimensional expressions for performance parameters, such as engine speed, airflow, fuel flow, and jet thrust, as functions of inlet flow parameters. The approximate humidity correction factors from moist air conditions (m) to dry air conditions (n) are as follows.

$$\text{Engine speed: } \frac{N_n \sqrt{\theta}}{N_m \sqrt{\theta}} = \frac{\sqrt{\gamma_{c,n} R_{c,n}}}{\sqrt{\gamma_{c,m} R_{c,m}}} \quad (1.2)$$

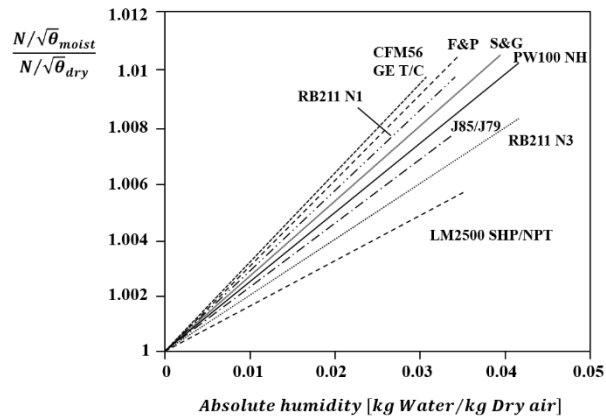
$$\text{Airflow: } \frac{W_{air,n} \sqrt{\theta}/\delta}{W_{air,m} \sqrt{\theta}/\delta} = \frac{\sqrt{\gamma_{c,n} R_{c,m}}}{\sqrt{\gamma_{c,m} R_{c,n}}} \quad (1.3)$$

$$\text{Fuel flow: } \frac{W_{fuel,n} \sqrt{\theta}/\delta}{W_{fuel,m} \sqrt{\theta}/\delta} = \frac{\sqrt{\gamma_{c,n} R_{c,m}}}{\sqrt{\gamma_{c,m} R_{c,n}}} \frac{C_{p,b,n}}{C_{p,b,m}} \quad (1.4)$$

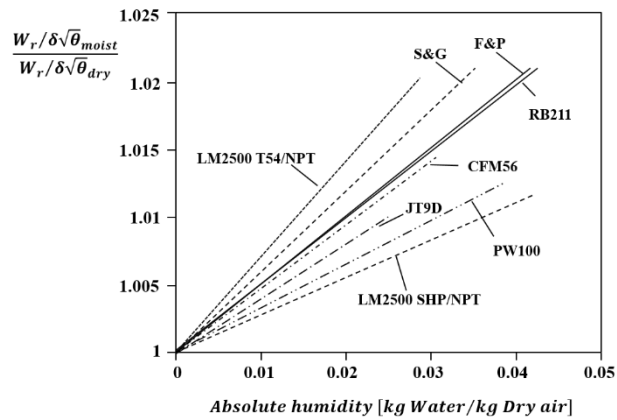
$$\text{Jet thrust: } \frac{F_n/\delta}{F_m/\delta} = \frac{\gamma_{e,n}}{\gamma_{e,m}} \quad (1.5)$$

The engine components are identified by subscripts as compressor c, combustion chamber b, and exhaust nozzle e. For the ratios of inlet to reference condition for pressure δ , and for temperature θ are used. These theoretical analyses were

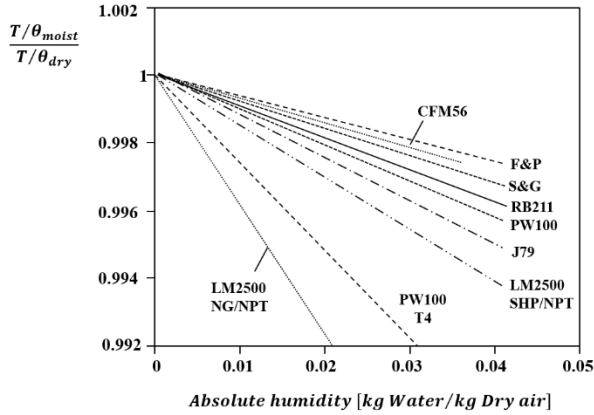
validated with engine test with all data corrected to constant engine speed. The agreement between the experimental and the theoretical prediction showed good agreement under the 0.5 % differences. Figure 1.5 shows the results of prediction as linear functions of absolute humidity.



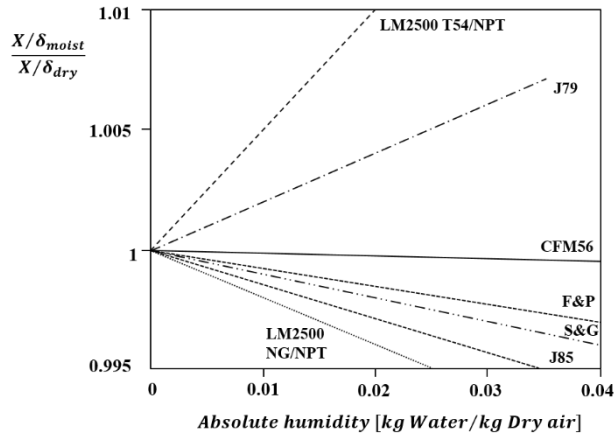
(a)



(b)



(c)



(d)

Figure 1. 7. Humidity correction factor: (a) compressor speed, (b) fuel flow, (c) Turbine inlet temperature, (d) trust.

Fishbeyn and Pervyshin [15] also investigated the effects of atmospheric humidity on the characteristics of turbofan engine. They generated a series of humidity correction factors for major performance parameters as a quadratic functions of absolute humidity, H .

$$\text{Engine speed: } C_N = 1 + 0.2607H - 0.1538H^2 \quad (1.6)$$

$$\text{Air flow: } C_A = 1 - 0.3352H - 0.4010H^2 \quad (1.7)$$

$$\text{Fuel flow: } C_F = 1 + 0.4882H + 0.3828H^2 \quad (1.8)$$

$$\text{Thrust: } C_T = 1 - 0.0826H - 0.0021H^2 \quad (1.9)$$

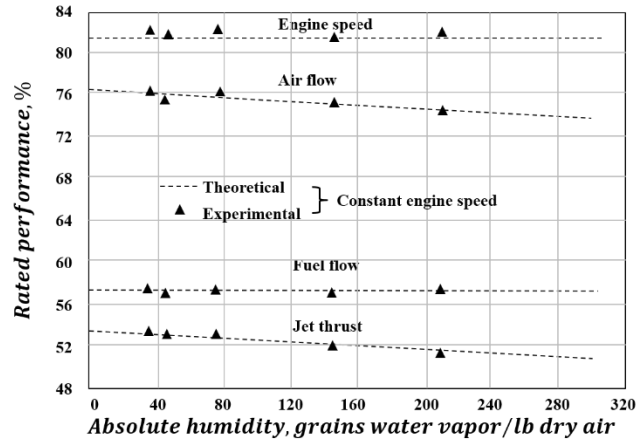


Figure 1. 8. Effects of humidity on engine performance.

Both results showed that all corrections had the same trend for a given parameter and good agreement exist between the two models. At a reasonable high absolute humidity condition, 0.0223 (100% relative humidity condition at 300K), differences in correction factors are at most 0.15% for the thrust and 0.2% for fuel flow.

The second effects of humidity on the gas turbine engine performance are come from the condensation at the engine inlet. As the flow is sucked into the engine inlet, due to the acceleration, temperature can fall down below the dew point. When the change of state and the consequent release of latent heat occurs, total temperature increases and total pressure decreases, thus, it adversely affects the performance of engine. Spencer and Archer [16] studied the effects of condensation in the long air inlet duct of the A-7 aircraft with a TF30 engine, operating in a humid environment. This investigation reported relative humidity from 30 to 60% in daytime and 90 to

95% in night time caused an increase in turbine inlet temperature of up to 50K. Blake [17] conducted an experimental test program using a JT9D-7 engine to establish empirically the effect of inlet condensation on specific fuel consumption. The results from a total 47 engine calibrations over a range of ambient conditions are shown in Figure 1.9 and the percentage change in specific fuel consumption was compared to the analytically derived ideal temperature rise in the inlet due to condensation. The results show a penalty of +0.34% SFC on a typical summer day with an ideal inlet temperature rise of 4K.

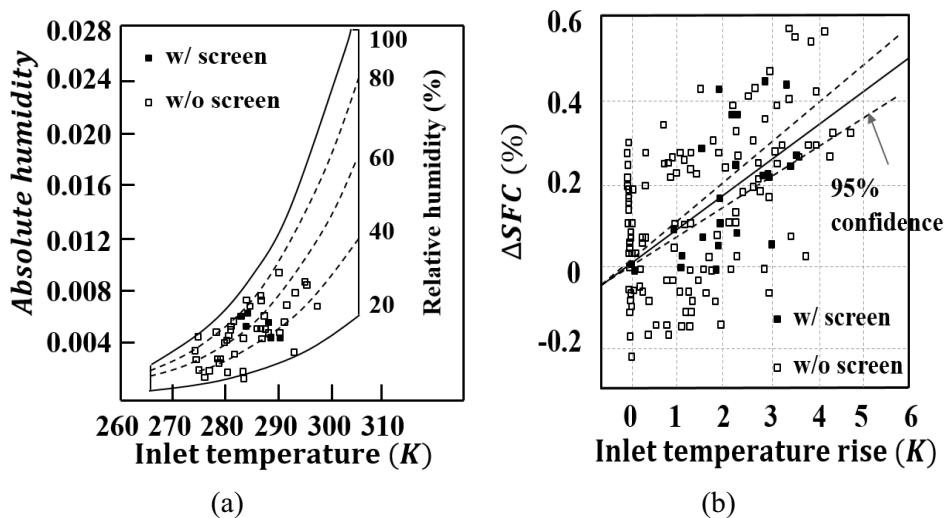


Figure 1. 9. JT9D-7 engine test: (a) atmospheric composition, (b) specific fuel consumption rise.

Since the humidity affects the gas turbine performance, Bird and Grabe [18] reported that during a cell correlation program, using a GE F404 turbofan engine, the following psychrometric conditions were specified by the engine manufacturer: 1) relative humidity less than 75%, 2) absolute humidity less than 0.01428, 3) no visible moisture in the air.

For the additional effects of condensation, AGARD Advisory report [19] pointed out the compressor stage mismatching due to the droplet evaporation in the compressor passage. As the droplets pass into the compressor, the air is heated by the work of compressor. This will gradually cause re-evaporation of the droplets, eventually creating dry conditions somewhere within the compressor. The temperature rise across the first stage of modern gas turbines is typically 50K which would be sufficient to re-evaporate any droplets created in the inlet. However, if larger droplets enter the compressor, for example due to rain, quite extensive regions of the compressor may operate with liquid present. The net effect of inlet condensate in the flow is to increase the total mass flow for a particular non-dimensional operating condition. These inlet conditions, however, no longer define the incidence distribution throughout the compressor as the re-evaporating flow modifies the volume flow and incidence distribution. Thus, if the stage matching has been optimized for dry air, the condensation and re-evaporation process will cause stage mismatch, possibly resulting in reduced efficiency. The general influence will be that evaporation within the compressor will have the effect of increasing the mass of gaseous flow, however the evaporation process absorbs heat so that the flow has a lower temperature. The increase in gaseous mass flow rate will tend to increase the velocity while the reduced temperature will increase density which tends to reduce the volume flow rate (reducing flow coefficient). The reduced temperature also increases the corrected operating speed, thereby increasing the stage pressure rise and density (reducing the axial velocity and flow coefficient). Furthermore the presence of evaporation tends to make the compression process more isothermal and so increase the pressure rise for a specific work input, further increasing density and

reducing the stage flow coefficient. Therefore, if the compressor is operating at design condition, the rear stages will operate near peak efficiency in dry conditions. The influence of condensation at the inlet, and re-evaporation within the compressor, appears to cause these rear stages to rematch at reduced flow coefficients (i.e. towards stall). Thus, this narrower operating range can be introduced. Figure 1.10 shows the compressor map change due to condensation & re-evaporation phenomenon in the compressor.

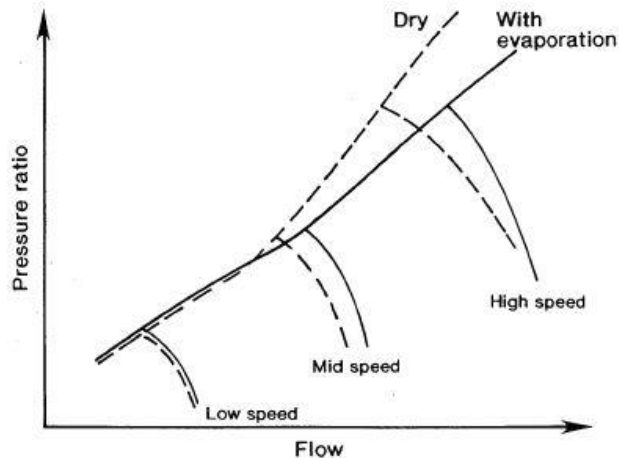


Figure 1. 10. Compressor map shift due to re-evaporation.

1.2.2. Humidity effects on the transonic flow field

If a moist air experiences a strong expansion (ex. Prandtl-Meyer expansion), a condensation zone develops due to the high cooling rate (order of $10^5 K/s$). The latent heat is released during the condensation process, thereby it affects the flow field. The effects of released latent heat can be analyzed by the Rayleigh flow which describes the 1-dimensional heat addition effects on the flow field. There are lots of

researches which studied the condensation effects on the transonic/supersonic flow field using supersonic nozzle, single airfoil and etc. The condensation phenomenon in the supersonic nozzle was first described in all essential details by Oswatitsch [20], and many experimental results by Wegner [21], Schnerr and Dohrmann [22], Frank [23], Lamanna [24], and Huang [25] were followed. Frank [23] studied condensation effects on the supersonic flow field by changing the relative humidity conditions. The condensation effects were describe by the density gradient change as shown in Figure 1.11, and the theoretical analysis was conducted and validated with experimental data.

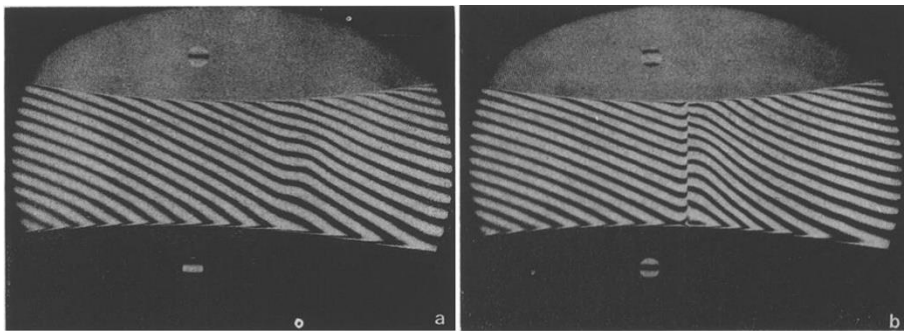


Figure 1. 11. Interferograms for the laval nozzle flow of a mixture of water vapor and air, a) absolute humidity 4g/kg, b) absolute humidity 8g/kg.

Lamanna [24] did experimental & numerical study using a supersonic nozzle. In this study, experimental data shows density profile following a nozzle axis, and the abrupt density increase is captured at the condensation location. Furthermore, the numerical results for various condensation models show good agreements. Figure 1.12 shows both experimental and numerical results of the density distribution along the nozzle axis.

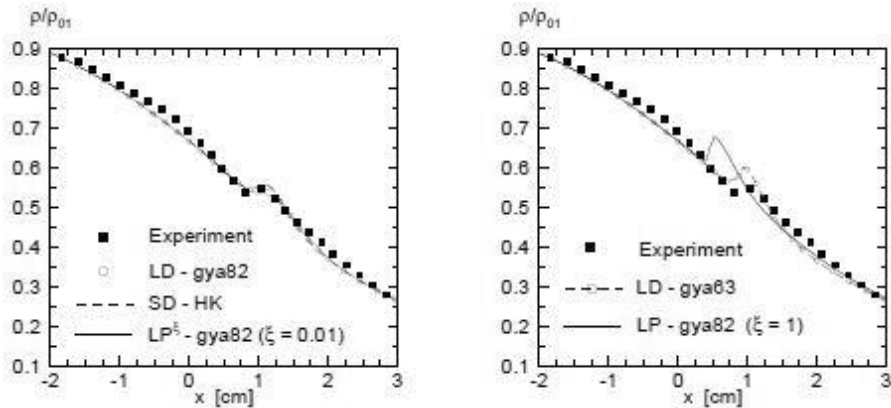


Figure 1.12. Density distributions along the nozzle axis for different condensation models.

Huang studied the condensation effects on transonic flow field using a bump. Inlet Mach number is 0.8, however, due to the local acceleration on the bump, supersonic flow was made and condensation occurred. In this experiment, the static pressure on the bump was directly measured, thus depending on the relative humidity conditions, condensation effects on the pressure field were shown. Figure 1.13 shows the isentropic Mach number distribution which is calculated with the static pressure and inlet total pressure using isentropic equation. As the relative humidity increased, consequently, more condensation occurred, the peak Mach number decreased and the Mach number downstream of shock decreased. This phenomenon can be analyzed by the Rayleigh flow which tells the Mach number decrease due to heat addition in a supersonic flow. Huang also showed the peak Mach number decrease about 10% and the shock strength reduction about 30% at 50% relative humidity condition. Schlieren method was adopted for the shock image capturing (Figure 1.14). For higher humidity condition (relative humidity higher than 44%), another shock was captured upstream of the aerodynamic shock which is called condensation shock. As relative humidity increased, location of aerodynamic shock moved

upstream until condensation shock appeared. However, due to the condensation shock, aerodynamic shock was pushed downstream as relative humidity increased over 44%

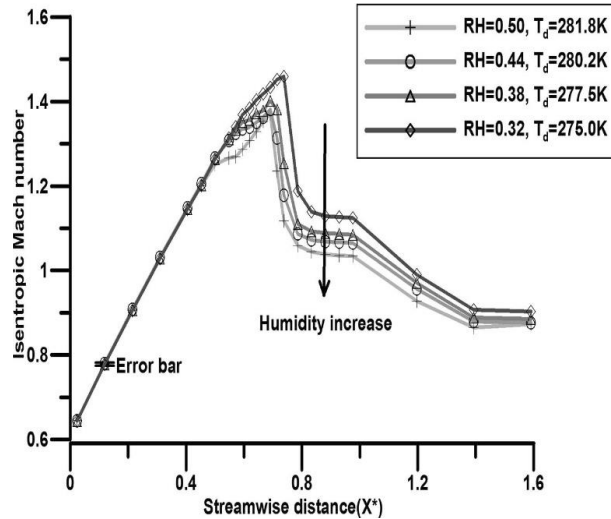


Figure 1.13. Isentropic Mach number distribution over the bump at inlet Mach number 0.8.

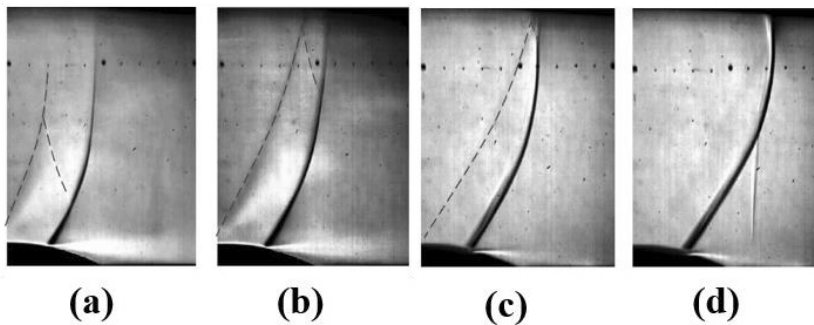
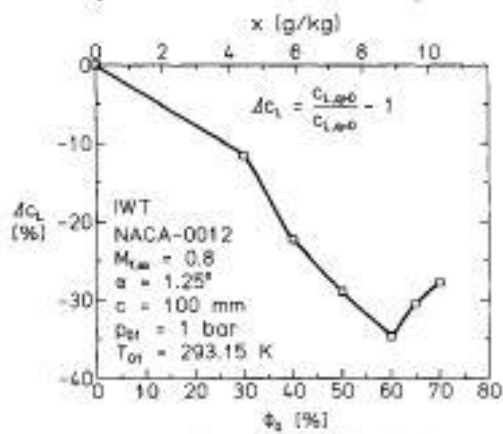


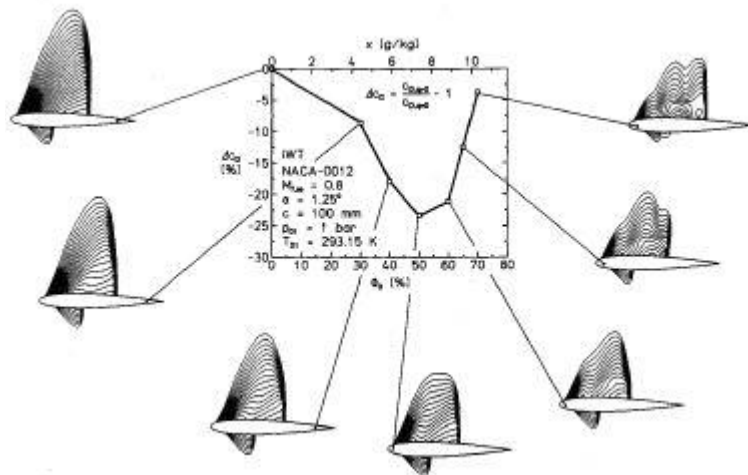
Figure 1.14. Schlieren images of shock waves over the bump: (a) RH= 50%, (b) RH= 44%, (c) RH= 38%, (d) RH=32%.

For humidity effects on a single airfoil flow field, Schnerr and Dohrmann [26, 27] did experimental and numerical works, and the pressure distribution on the airfoil and lift & drag coefficient were investigated. As the condensation occurred on the

suction surface, pressure increased; lift coefficient decreased up to 35% at relative humidity condition of 60%. At the same time, due to the shock strength reduction, drag coefficient decreased up to about 25%. However, as relative humidity increased over 60%, where condensation shock appeared, drag coefficient abruptly increased. The numerical results showed good agreements with experimental results, and Figure 1.15 shows the results of that.



(a)



(b)

Figure 1. 15 Condensation effects on the aerodynamic performance of a airfoil: (a) lift coefficient, (b) drag coefficient.

1.2.3. Humidity effects on the compressor cascade flow field

Although the significant effects of condensation on the transonic flow field (as seen in the previous section), there are only few studies which investigated the humidity effects on the compressor cascade flow field. Yashiro et al. [28], Sun et al [29] and Yamamoto et al. [30] did numerical simulation using a blade geometry of Schreiber et al.'s [31]. Yashiro et al. [28] showed Mach number contour for one relative humidity condition of 80% (Figure 1.16), and found the shock location shifts downstream. Sun et al. [29] did similar calculation for a relative humidity condition of 70%. The change of static pressure coefficient distributions were discussed (Figure 1.17): the increase of pressure coefficient upstream of shock and the decrease of peak Mach number. Yamamoto et al. [30] studied the condensation effects for 4 different humid conditions, and the changes in pressure coefficient distribution and Mach number contour were discussed. The results also showed the shock location shift as other researchers' calculation results. All the previous CFD researches showed consistent results: i) condensation occurs ii) peak Mach number decrease, and iii) shock location shifts, however, focus was on the blade loading and/or Mach number distribution change, but detailed flow analysis was limited. Furthermore, these numerical researches conducted without experimental validation.

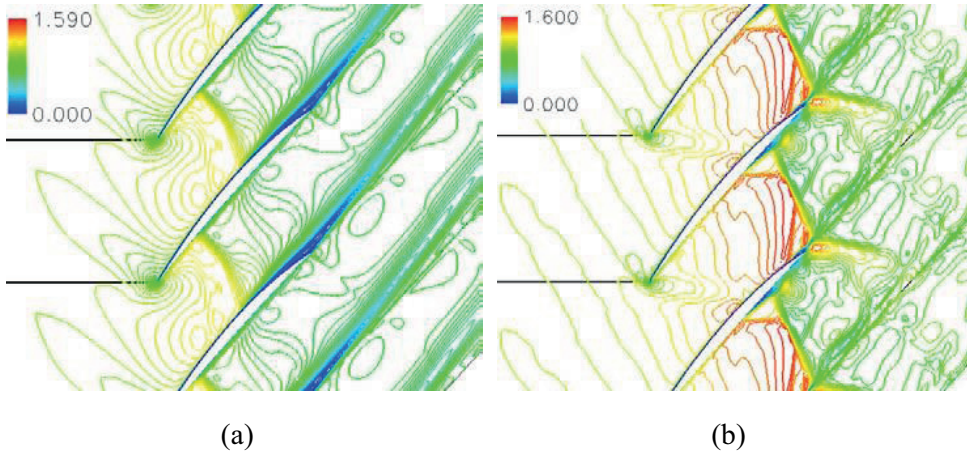


Figure 1. 16. Condensation effects on Mach number contour: (a) dry, (b) RH 80%.

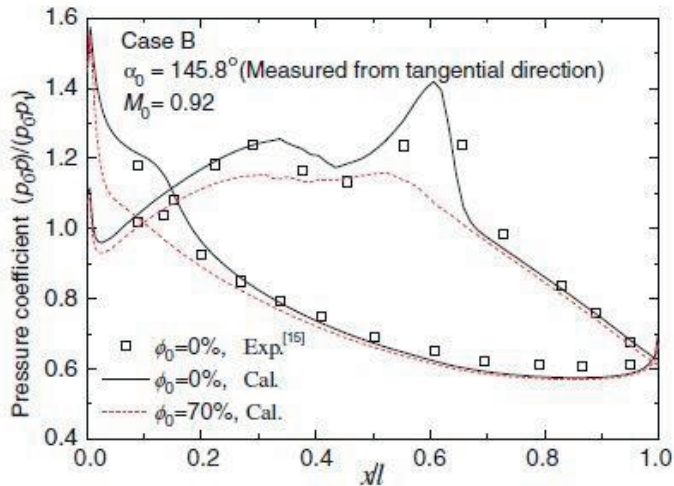
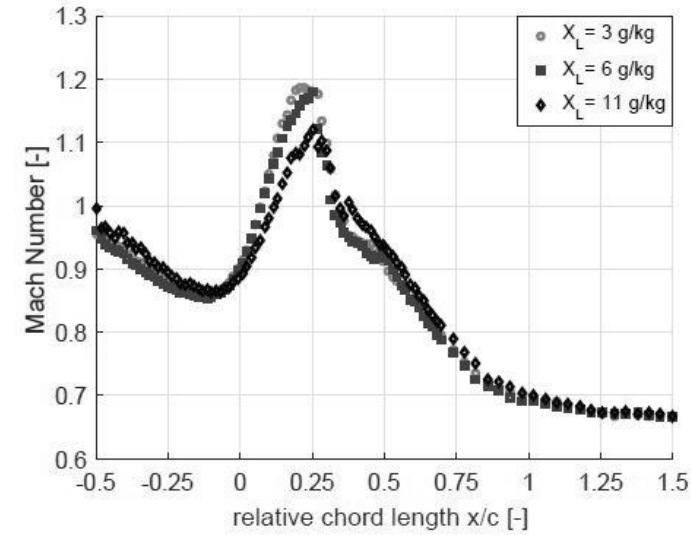


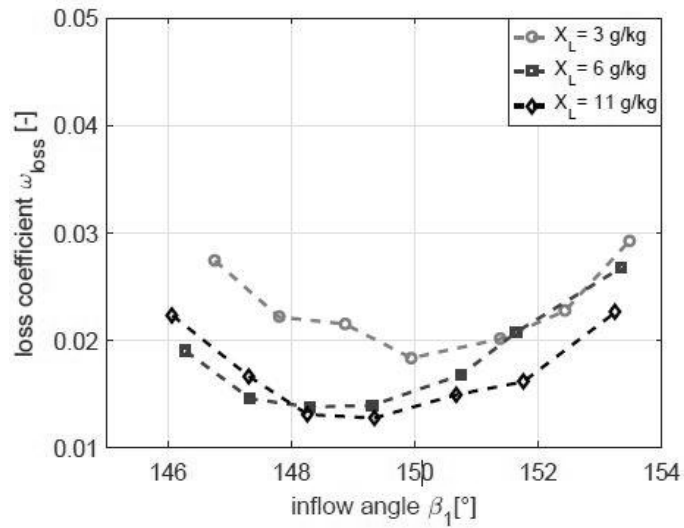
Figure 1. 17. Condensation effects on the pressure coefficient distribution.

Geist et al. [32], for the first time, conducted an experiment about the humidity effects on the transonic compressor cascade flow field. They measured velocity field for varying humidity, and calculated Mach number and loss coefficient from the velocity data. As humidity increased, peak Mach number upstream of shock was decreased due to heat addition from condensation, and loss coefficient was predicted to decrease due to the reduced shock strength. However, such loss coefficient estimation using momentum deficit considered only the profile loss and did not

consider thermodynamic loss. Furthermore, humidity effects on blade loading distribution and deviation were not measured.



(a)



(b)

Figure 1. 18. Humidity effects on the compressor cascade aerodynamic characteristics: (a) isentropic Mach number distribution, (b) loss coefficient.

1.3. Motivation and Research Objectives

From the early beginning of gas turbines, it was recognized that humidity in the air could potentially affect the gas turbine performance. However, since reliability and operability received more attention than performance, humidity effects were considered to be of secondary importance and were usually neglected. However, with the commercial competition and development of high performance engine, attention has been focused again on the humidity. Furthermore, as inlet fogging or wet compression device has been widely adopted in a power plant, gas turbines are increasingly exposed to humid environments.

Traditionally, the gas turbine performance change due to humidity in the air has been analyzed with two points of view. First view is the gas properties change, and the second view is a condensation at engine inlet. Samuels and Gale [14] derived correction factors for engine speed, airflow, fuel flow, and jet thrust, and validated with turbojet engines. Fishbeyn and Pervyshin [15] also derived correction factors as Samuels and Gale using turbofan engine. Both results showed decreasing thrust as increasing the absolute humidity, up to 0.5% of thrust decreased at absolute humidity of 0.03. For the condensation effects at the engine inlet, Spencer and Archer [16] and Blake [17] conducted engine test for various humidity conditions. They found that due to the engine inlet temperature rise from condensation, there is a penalty of specific fuel consumption (SFC) about 0.34% at engine inlet temperature rise of 4K. However, there are very limited previous researches about humidity effects on the compressor flow field. Although from the CFD researches [28, 29, 30] and an experimental research [32] using a cascade device, the understandings about humidity effects on the compressor flow field are very limited. Even in the Geist et

al.'s experimental research, the thermodynamic loss from condensation was not reflected in calculated loss coefficient, and the humidity effects on blade loading distribution and deviation were not measured.

Therefore, the object of this study is to investigate the humidity effects on the aerodynamic performance of a transonic compressor cascade. Experimentally, using a cascade device, the humidity effects on the pressure coefficient distribution, deviation, and loss coefficient have been measured. Numerically, adopting a Classical Nucleation Theory model and Hertz-Knudsen droplet growth model, non-equilibrium condensation has been simulated to help the understandings of humidity effects on the cascade flow field.

1.4. Thesis Organization

This thesis consists of the following seven chapters.

Chapter 1. introduces keywords of the thesis such as gas turbine, transonic compressor, blade to blade flow, and cascade performance. Also, previous studies in humidity effects on gas turbine performance and on transonic flow field are reviewed. Based on the background information, research motivation and objectives are stated.

Chapter 2. presents the physics of condensation which is the most interested phenomenon in this thesis including condensation models.

Chapter 3. presents experimental facility including a newly developed transonic wind tunnel, water supply system, test section and instrumentations.

Chapter 4. describes experimental results including test matrix, cascade flow quality, and cascade performance.

Chapter 5. presents numerical method including mesh, solver setting, and validation results.

Chapter 6. describes numerical results which support and help the understandings of experimental results.

Chapter 7. summarizes contributions of this thesis and recommends future work.

Chapter 2. Physics of Condensation

2.1 Introduction

A pure water can exist in three different phases in nature: gas, liquid, and solid. Figure 2.1 shows the P-T diagram of it. There are three phase curves in the diagram: 1) the vapor curve which is representing the equilibrium between the gas and liquid phase, 2) the melting curve which is representing the equilibrium between the liquid and solid phase, and 3) sublimation curve which is representing the equilibrium between the gas and solid phase.

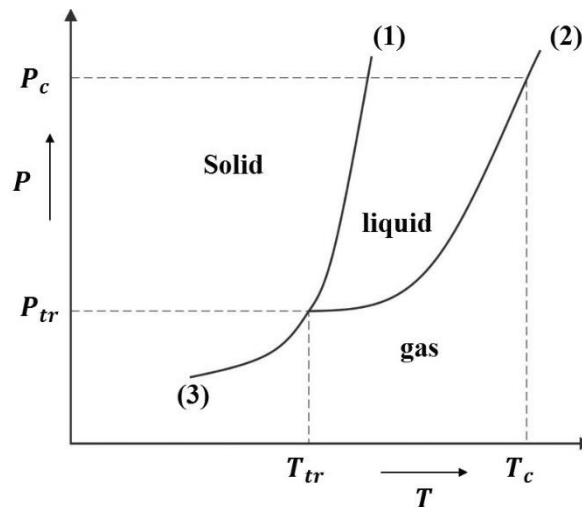


Figure 2. 1 P-T diagram of water.

When water experiences a slow thermodynamic state change, its thermodynamic state changes continuously from previous equilibrium state to another thermodynamic state, and every time a thermodynamic state changes, water

maintains its equilibrium state. However, when thermodynamic state changes rapidly, such as rapid expansion in a supersonic nozzle, its thermodynamic state radically departs from the equilibrium state and slowly recover to its equilibrium state. A phase transition accompanied by a non-equilibrium state is called “non-equilibrium phase transition”. Among various phase transition, vapor phase to liquid phase transition (i.e., condensation) will be discussed in this chapter.

2.2 Condensation

2.2.1. Non-equilibrium condensation



Figure 2. 2. Non-equilibrium condensation in F-18 aircraft.

When a flow experiences rapid expansion, temperature decreases rapidly (typically $10^6/s$). Then, thermodynamic state of vapor radically departs from the equilibrium state because characteristic time scale for condensation is larger than the characteristic time of temperature change. Therefore, vapor maintains its phase in a non-equilibrium state for a while, and then, phase transition occurs, and recovers its

thermodynamic state to equilibrium state. The extent of non-equilibrium is usually expressed in terms of supersaturation ratio, which is defined as the ratio between vapor pressure and saturated vapor pressure.

$$s = \frac{P_v}{P_{v,eq}} \quad (2.1)$$

When $s > 1$, it is called supersaturation, and even it reaches order of 2 in rapid expansion flows until condensation occurs. The first stage of condensation is called nucleation which represents a step of forming stable clusters (i.e., nuclei) from vapor molecules. This step is driven by a statistical fluctuation, and divided into two depending on whether foreign particles (such as dust and ions) are involved in the formation of nuclei – homogeneous nucleation and heterogeneous nucleation. Heiler [33] proved that heterogeneous effects is negligible in laboratory experiments due to the comparatively low concentration of foreign particles. Therefore, in this study, foreign particles effects in nucleation are not considered, thus, homogeneous condensation is solely considered. The second step of condensation is called droplet growth which represents a step that vapor molecules attach on the stable clusters. In this step, thermodynamic equilibrium state quickly established, thus, most formation heat (i.e., latent heat) is transferred between vapor and liquid. Due to the large formation heat of water, heat transfer from liquid to vapor phase highly affects flow field. For example, for a supersonic, flow heat addition increases pressure and temperature both, thus, Mach number decreases. For a subsonic flow heat addition increases temperature, however, decreases pressure, thus Mach number increases.

2.2.2. Homogeneous nucleation

Homogeneous nucleation involves the formation of meta-stable clusters, from a molecules in a supersaturated state. The driving potential is the supersaturation, and free energy difference between gas and liquid phases. The free energy of formation of a cluster containing n molecules can be expressed as Luijten [34], and expression is as follows.

$$\Delta G_n = \sigma a_0 n^{2/3} - nk_B T \ln(s) \quad (2.2)$$

Where, k_B is a Boltzmann constant, σ is a surface tension of a flat surface, and a_0 is a molecular surface area which is defined as:

$$a_0 = (36\pi)^{1/3} v_l^{2/3} \quad (2.3)$$

Where, v_l is the liquid molecular volume, defined as a follow.

$$v_l = \frac{M_{molar}}{N_A \rho_l} \quad (2.4)$$

Thus, first term of Eq. (2.2) represents the increase in free energy due to the formation of the interface between liquid and gas phases, thus, it increases with respect to n as an order of $2/3$. Second term represents the free energy reduction due to phase transition from high energy state (gas) to low energy state (liquid). Therefore, it increases with respect to n as an order of 1. When $s < 1$, the free

energy of formation monotonically increases as the number of molecules in a cluster increases. Thus, stable cluster cannot be formulated. However, when $s > 1$, there is a competing between the free energy increase for making the interface (first term in Eq. 2.2) and the free energy decrease for moving to lower thermodynamic state (second term in Eq. 2.2). The difference of free energy is plotted vs. number of molecules in a cluster in Figure 2.3.

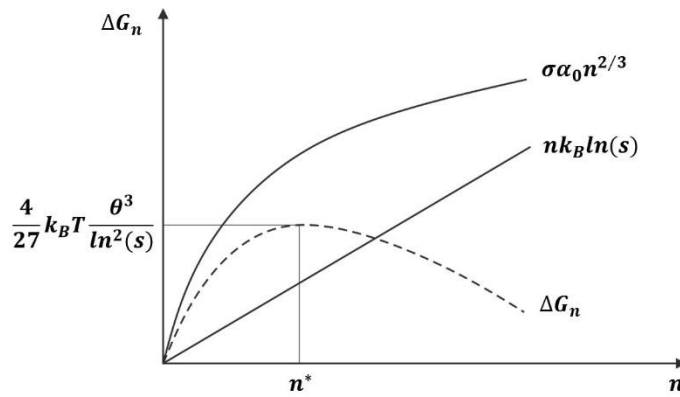


Figure 2. 3. Free energy of formatting a cluster with n molecules.

The formation energy increases until a critical value (n^*), and then, decreases as a number of molecules increases. This critical value can be calculated by differentiating the formation energy by molecular number n (i.e., $(\partial\Delta G_n/\partial n)_{n^*} = 0$), then results are as follows.

$$n^* = \left(\frac{2\theta}{3 \ln(s)}\right)^3 \quad (2.5)$$

Where, $\theta = \sigma a_0/k_B T$, dimensionless surface tension which represents the relative importance of surface to thermal energy. Therefore, clusters consisting of

molecules smaller than the critical value n^* , it cannot grow to droplets, and will be disappeared due to unfavorable free energy change. Only the clusters consisting of molecules larger than the critical value, it will grow to droplets. Therefore, in the nucleation step, clusters consisting of molecules larger than the critical value are counted, and its theoretical models are discussed in next section.

2.2.3. Nucleation theory

A nucleation theory represents the rate of formation of stable clusters per unit time. By thermodynamics consideration, it can be derived with a closed expression [34, 35, 36]. The nucleation model has a form of follows:

$$J = K \cdot \exp(\Delta G_{n^*}/k_B T) \quad (2.6)$$

Where, K is a kinetic constant which is derived from impingement rate of monomers and dissociation rate of polymers. Therefore, nucleation model is divided with two parts – kinetic part and thermodynamic part, and there are many nucleation models depending on the explicit form for the K , and ΔG_{n^*} . In this section, two different models are considered: The Classical Nucleation Theory (CNT) and the Internally Consistent Classical Theory (ICCT).

$$\text{CNT-model:} \quad J_{CNT} = \frac{\rho_v^2}{\rho_l} \sqrt{\frac{2\sigma}{\pi m^3}} e^{-\frac{4}{27} \frac{\theta^3}{\ln^2(S)}} \quad (2.7)$$

$$\text{ICCT-model:} \quad J_{ICCT} = \frac{1}{s} \frac{\rho_v^2}{\rho_l} \sqrt{\frac{2\sigma}{\pi m^3}} e^{-\frac{4}{27} \frac{\theta^3}{\ln^2(S)}} e^\theta \quad (2.8)$$

The two models differ each other with the presence of the factor $1/s$ and the exponential factor e^θ . The exponential factor is directly connected to the issue of self-consistency in modelling the formation energy [34], thus, it corrects the formation energy of monomer nuclei as 0 which is not in CNT model (i.e. $\Delta G_1 = 0$). However, on this issue, there are no general agreement. Rather, the performance of a certain nucleation model strongly depends on the temperature range with in which nucleation takes place. Furthermore, the nucleation rate depends exponentially on the third power of the surface tension, thus, accurate measurements of surface tension is more important than the nucleation model itself. However, until now, there are not exact surface tension data of super-cooled liquid under 250K [33]. Many researchers interpolate surface tension data under 250K with various methods [26, 34, 37, 38], thus, both nucleation models show poor predictions about order of 2 differences. Therefore, there is not sound justification for preferring the ICCT model to the CNT model. Thus, in this study, Wolk et al.'s results have been adopted for deciding nucleation model. He measured the nucleation rate for temperature range from 220K to 260K, and compared it with predictions of CNT model. A correction factor was introduced which compensates temperature dependence of nucleation model, and it is adopted to this study. The equation is as follows.

$$J = e^{-27.56+6500/T} \frac{\rho_v^2}{\rho_l} \sqrt{\frac{2\sigma}{\pi m^3}} e^{-\frac{4}{27} \frac{\theta^3}{\ln^2(S)}} \quad (2.9)$$

As a concluding remarks, the above two nucleation models are derived based on

the assumptions of macroscopic property of cluster. In adopting surface tension data, surface tension of bulk liquid is adopted and it is called capillarity approximation. Also the nucleation rate is derived by steady state solution which means the rate of change in number density of clusters is independent with cluster size. The first issue is resolved because experimental correction factor is adopted in nucleation rate model. About the second issue, Abraham [39] discussed a steady state solution for the nucleation rate is reached with a characteristic time of 10^{-7} to 10^{-6} seconds. In this study, cooling rates are about $1 \text{ K}/\mu\text{s}$, thus, implying the steady state nucleation formulation can be adopted.

2.2.4. Droplet growth theory

Once a stable cluster has been formed, it grows to a droplet. In this process, Knudsen number ($\text{Kn} = l/2r$) governs which is a dimensionless number defined by the ratio between mean free path l , and droplet diameter $2r$. For small Kn, i.e. large droplets, droplets grow by a diffusion of vapor molecules in a continuous way. Therefore, this regime is called continuous regime. For large Kn, i.e. small droplets, droplets grow in a way of kinetic process of impingement. Therefore, this regime is called free molecular regime. And between these regimes is called transition regime. There are many droplet growth models describing the droplet growth process such as Gyarmathy [40], Young [41], and Hertz-Knudsen [42, 43] model. But there are not global agreements which one is preferable between these models. Peeters et al. [44] found Gyarmathy's model predicts their experimental droplet growth curve better than Young's model for large Kn ($\text{Kn} > 0.1$), but low Kn, Young's model predicts better. In addition, Lamanna [37] found that the classical nucleation

model/Hertz-Knudsen droplet growth model combination showed predictions most similar to the wave tube experimental data. In this study, droplets are expected to be small because of short compressor cascade passage length, and Gyarmathy's model in a free molecular regime is coincide with Hertz-Knudsen model, thus, Hertz-Knudsen model is adopted and the equation is as follows.

Hertz-Knudsen model:

$$\frac{dr}{dt} = \frac{1}{\rho_l} \left(\frac{P_v}{\sqrt{2\pi R_v T}} - \frac{P_{v,r}}{\sqrt{2\pi R_v T_d}} \right) \quad (2.10)$$

The Hertz-Knudsen's droplet growth model is based on a balance between impingement of a monomer onto a droplet (i.e. condensation) and detachment of a monomer from a droplet (i.e. evaporation). Therefore, first term means a condensation, and the second term means an evaporation. T_d represents the droplets' temperature, and in this study, temperature difference between droplets and surrounding gas is neglected (i.e. $T_d = T$) because when considering the condensation/evaporation phenomenon with a carrier gas, such as condensation in humid air, carrier gas acts as heat resolver, thus, temperature difference between droplets and carrier gas can be neglected [45]. $P_{v,r}$ is the partial super saturated vapor pressure over the droplets which radius is r . It is derived from the Kelvin relation, and expression is as follows.

$$P_{v,r} = P_{v,eq} \exp(2\sigma/r\rho_l R_v T_d) \quad (2.11)$$

Where, subscript eq represents an equilibrium state, thus, this term describes

droplet radius effects on the droplet growth rate.

2.3 Governing equations

2.3.1. Thermodynamic properties

The Objective of this section is to define the thermodynamic properties of mixture which is composed of an inert gas (i.e. carrier gas, air in this case) and a condensable vapor (water in this case). Before defining the thermodynamic properties of mixture, validating whether previous thermodynamic equations can be adopted for describing condensing flow is important because if local thermodynamic equilibrium is not satisfied, it is theoretically impossible to describe the state of the mixture by means of simple thermodynamic relations (ex. Equation of state, internal specific energy e , specific heat, speed of sounds, etc. [37]).

For the general behavior of non-equilibrium condensing flow, Marble [46] first discussed from the relaxation gas dynamics and Young et al. [41] extends it in more general conditions. Summarization of this issue as follows. First, until the nucleation occurs, mixture is in a metastable equilibrium condition. Thus, standard thermodynamic relations can be applied to each gas components. Second, after the nucleation occurs, droplets are formed, and droplet grows. Thus, in this stage, mixture is not in the thermodynamic equilibrium state, and there is an interface exchange of mass, momentum, and energy. Each of these process is physically characterized by its relaxation time. About this issue, Young et al. introduced 3 different relaxation process: thermal equilibrium of droplets, interface velocity slip, and thermal equilibrium of the whole medium. Young et al. discussed that relaxation

time of thermal equilibrium of droplets is the fastest one. Thus, droplet temperature approaches to its equilibrium value fast. Second, for the interface velocity slip, Young et al. argued that velocity difference of relatively small droplets ($r \ll 10^{-6}m$) can be neglected. Third, the thermal equilibrium of the whole medium (i.e. gas phase temperature reaches to its equilibrium value) is relatively slow. Thus, when the flow experiences high cooling rates, (about order of $0.1K/\mu s$), the variations driven by flow field are faster than the thermal variations due to condensation. The mechanics and thermodynamics of the gas and liquid phase are uncoupled and the gas phase flow behaves like that of a simple single phase gas (i.e. it can be considered as frozen flow). Therefore, the mixture behavior characteristics can be described by the system of conservation laws, momentum, energy equation, and additional equation for describing the formation of the condensate mass fraction.

Consider a infinitesimally small mixture element which volume is V , and mass is M . It consists of air, water vapor, and droplets. Then, the mixture mass is divided by mass of air M_a , mass of vapor M_v , and mass of droplets M_l .

$$M = M_a + M_v + M_l \quad (2.12)$$

The sum of the mass of vapor and droplets are constant for a specific inlet condition, thus, it is represented M_{v0} which states total vapor mass without condensation (subscript 0 represents a value without condensation).

$$M_{v0} = M_v + M_l \quad (2.13)$$

Then, the condensate mass fraction g can be defined by the ratio between the mass of liquid phase and the mass of total mixture.

$$g \equiv \frac{M_l}{M} \quad (2.14)$$

The maximum value of the liquid mass fraction is defined by follows.

$$g_{max} \equiv \frac{M_{v0}}{M} \quad (2.15)$$

The density of mixture defined by follows.

$$\rho = \frac{M}{V} \quad (2.16)$$

So that, the density of air, density of vapor, and density of droplets are

$$\rho_a = \frac{M_a}{V} = \rho(1 - g_{max}) \quad (2.17)$$

$$\rho_v = \frac{M_v}{V} = \rho(g_{max} - g) \quad (2.18)$$

$$\rho_l = \frac{M_l}{V} = \rho g \quad (2.19)$$

The isochoric and isobaric specific heat constants c_{v0} , c_{p0} and the specific gas constant of mixture R_0 are:

$$c_{v0} = (1 - g_{max})c_{va} + g_{max}c_{vv} \quad (2.20)$$

$$c_{p0} = (1 - g_{max})c_{pa} + g_{max}c_{pv} \quad (2.21)$$

$$R_0 = (1 - g_{max})R_a + g_{max}R_v \quad (2.22)$$

The static pressure of the mixture is the sum of the partial pressure of the gas components:

$$P = P_a + P_v \quad (2.23)$$

From the thermal equilibrium assumption, temperature of air, vapor, and droplets are same:

$$T = T_a = T_v = T_l \quad (2.24)$$

Under the assumption of perfect gas, each gaseous component pressure are:

$$P_a = \rho_a R_a T \quad (2.25)$$

$$P_v = \rho_v R_v T \quad (2.26)$$

The specific enthalpy of the mixture is the sum of the each components:

$$h = (1 - g_{max})h_a + (g_{max} - g)h_v + gh_l \quad (2.27)$$

The latent heat L is defined as the difference between the specific enthalpy of vapor and liquid. Thus latent heat L is defined as:

$$L \equiv h_v - h_l \quad (2.28)$$

Thus, eq. (2.3.16) can be expressed as follows.

$$h = (1 - g_{max})h_a + g_{max}h_v + gL \quad (2.29)$$

For the specific internal energy of mixture, it can be expressed as:

$$\begin{aligned} e &= (1 - g_{max})e_a + (g_{max} - g)e_v + ge_l \quad (2.30) \\ &= c_{v0}T + g(R_vT - L) \end{aligned}$$

Using the definition of enthalpy, $h = e + P/\rho$, eq. (2.3.18) can be written as:

$$e = (1 - g_{max})e_a + (g_{max} - g)e_v - gL + g\left(\frac{P_v}{\rho_v} - \frac{P_l}{\rho_l}\right) \quad (2.31)$$

Under the assumption of $P = P_l$, which is reasonable assumption because pressure acting on the droplet is equal to mixture pressure, and using c_{v0} , and definition of internal energy, $e = c_vT$, eq. (2.3.20) is written as:

$$e = c_{v0}T - gL + g\left(R_v - \frac{\rho}{\rho_l}R\right)T \quad (2.32)$$

Because $\rho \ll \rho_l$ (ρ_l is about 100 kg/m^3), last term in the eq. (2.3.21) can be

neglected as:

$$e = c_{v0}T - g(R_vT - L) \quad (2.33)$$

The last physical quantity is a speed of sound. The speed of sound is an important quantity because it determines the speed of infinitesimally small disturbances propagation. In condensing flow, its composition is not constant, thus, the frozen speed of sound is used instead of speed of sound. The difference between two speed of sound is that in frozen speed of sound, its values is calculated with fixed composition, and eliminates the amount of liquid mass for calculating speed of sound. The definition of frozen speed of sound is as follow, and its derivations are found in Put [47].

$$a_{frozen}^2 = RT \left[1 + \frac{R}{c_{v0} + g(R_v - L_1)} \right] \quad (2.34)$$

Where, L_1 is the first order coefficient of latent heat respect to the temperature. The value of L_1 and the other physical quantities such as R_a , R_v , c_{av} , c_{vv} , L etc. are provided at the end of this chapter.

2.3.2. Governing equation

In this section, for simulating the condensing flow in the compressor cascade, Euler equations with Hill's Method of Moments [48] is introduced. Viscous effects on the blade have been considered, however, the drag due to droplets has not been considered because following Young et al.[45], velocity slip between droplets and

flow can be neglected in case of small droplets ($r < 1\mu\text{m}$). In addition, ideal and calorically perfect gas has been assumed. The Governing equations are as follows.

$$\frac{\partial U}{\partial t} + \frac{\partial F}{\partial x} + \frac{\partial G}{\partial y} + \frac{\partial H}{\partial z} = Q \quad (2.35)$$

$$U = \begin{bmatrix} \rho \\ \rho u \\ \rho v \\ \rho w \\ \rho e \end{bmatrix} \quad F = \begin{bmatrix} \rho u \\ \rho u^2 + P - \tau_{xx} \\ \rho uv - \tau_{xy} \\ \rho uw - \tau_{xz} \\ (\rho e + P)u \end{bmatrix} \quad G = \begin{bmatrix} \rho v \\ \rho uv - \tau_{xy} \\ \rho u^2 + P - \tau_{yy} \\ \rho vw - \tau_{yz} \\ (\rho e + P)v \end{bmatrix} \quad H = \begin{bmatrix} \rho w \\ \rho uw - \tau_{xz} \\ \rho vw - \tau_{yz} \\ \rho w^2 + P - \tau_{zz} \\ (\rho e + P)w \end{bmatrix}$$

$$Q = \begin{bmatrix} 0 \\ 0 \\ 0 \\ 0 \\ \frac{d(\rho g L)}{dt} \end{bmatrix}$$

Where U is the vector of the dependent variables, and F , G and H are the conservative flux vectors. Q is the source vector which contains the effect of adding latent heat, L , from the condensation process. To calculate the condensate mass fraction g , below explicit equation have to be solved.

$$\frac{dg}{dt} = \frac{4\pi}{3} \rho_l r(t)^3 \frac{J(t)}{\rho(t)} + \int_{-\infty}^t 4\pi \rho_l \frac{J(\tau)}{\rho(\tau)} \frac{\partial r(t,\tau)}{\partial t} r(t,\tau)^2 d\tau \quad (2.36)$$

The first term represents a condensate mass formation at time t , and the second term represent a droplet growth which formulated time before. Hill [48] solved this equation adopting 4 auxiliary parameters Q_i ($i = 0,1,2,3$), and this method is called ‘‘Hill’s Method of Momentum’’. Deriving this equations is over the scope of

this research, thus, see Hill [48] or Put [47] for detail. The results of the Hill's Method of Momentum for liquid phase calculation is as follows.

$$\frac{\partial A}{\partial t} + \frac{\partial B}{\partial x} + \frac{\partial C}{\partial y} + \frac{\partial D}{\partial z} = K \quad (2.37)$$

$$A = \begin{bmatrix} \rho g \\ \rho Q_2 \\ \rho Q_1 \\ \rho Q_0 \end{bmatrix} \quad B = \begin{bmatrix} \rho u g \\ \rho u Q_2 \\ \rho u Q_1 \\ \rho u Q_0 \end{bmatrix} \quad C = \begin{bmatrix} \rho v g \\ \rho v Q_2 \\ \rho v Q_1 \\ \rho v Q_0 \end{bmatrix} \quad D = \begin{bmatrix} \rho w g \\ \rho w Q_2 \\ \rho w Q_1 \\ \rho w Q_0 \end{bmatrix}$$

$$K = \begin{bmatrix} \frac{4}{3} \pi \rho_l (J r^{*3} + 3 \rho Q_2 \dot{r}) \\ J r^{*2} + 2 \rho Q_1 \dot{r} \\ J r^* + \rho Q_0 \dot{r} \\ J \end{bmatrix}$$

Where, Q_i is an auxiliary parameter defined as

$$\rho Q_i = \int_{-\infty}^t \rho(t) r(t, \tau)^n J(\tau) / \rho(\tau) d\tau \quad \text{where, } i = 0, 1, 2, 3 \quad (2.38)$$

Hill's average droplet radius is defined by as follow from the definition of auxiliary parameter.

$$r_{Hill} = \sqrt{\frac{Q_1}{Q_0}} \quad (2.39)$$

So that, droplet radius can be calculated from the auxiliary parameters.

2.4 Material properties

2.4.1. Surface tension

At the beginning of condensation process, the formation of stable nuclei (which is composed of n molecules) is a major process. In order for the nuclei generated to be stable, the free energy must be changed favorably over the increase in the number of molecules. Surface tension is an important factor affecting the order of 3 in determining free energy. Despite its importance, experimental results are not available at low temperature below 250K. Therefore, in many previous studies [49, 34] on condensation, surface tension data at low temperature were approximated by linear extrapolation based on the experimental data of Hacker [50]. His data go down to roughly 250K and are plotted in Fig. 2.4 with other extrapolation fits. In the other hand, there are many different fits for surface tension in the other forms. Schnerr and Dohrmann [26] proposed the following surface tension fit through a condensation experiment in airfoil, and argued that CFD results predicted most well with this surface tension fit.

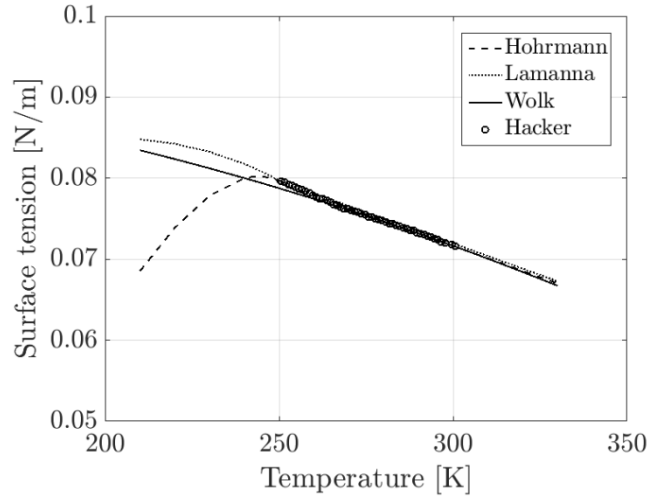


Figure 2. 4. Surface tension of liquid water and its extrapolations.

Schnerr – Dohrmann’s surface tension fit (2.40)

$$\sigma^{SD} = \begin{cases} (76.1 + 0.155 \cdot (273.15 - T)) \cdot 10^{-3} [N/m] & \text{for } T \geq 249.39K \\ (1.1313 - 3.7901 \cdot 10^{-3}T)T^4 \cdot 10^{-10} [N/m] & \text{for } T < 249.39K \end{cases}$$

Lammana [37] proposed different expression for the surface tension at low temperatures based on a supersonic nozzle experiment. This expression gives good correlation with experimentally obtained density distributions following the nozzle axis. Lammanna’s expression is as follows.

Lamanna’s surface tension fit (2.41)

i) for $T \geq 250.0K$

$$\sigma^L [N/m] = (76.1 + 0.155 \cdot (273.15 - T)) \cdot 10^{-3}$$

ii) for $T < 250.0$

$$\begin{aligned} \sigma^L [N/m] \\ = 8.52 \cdot 10^{-2} - 3.54236 \cdot 10^{-4}T + 3.5083 \cdot 10^{-6}T^2 - 8.7169 \cdot 10^{-9}T^3 \end{aligned}$$

In this study, since the correction factor of Wölk et al. [21] is applied to the nucleation rate model, the surface tension fit used in the Wölk et al.'s study is applied.

The fit [51] is as a follow.

Wölk et al.'s surface tension fit (2.42)

$$\sigma^{\text{Wölk}} = 0.001 * (93.6635 + 0.009133 \times T - 0.000275 \times T^2) \text{ [N/m]}$$

2.4.2. Liquid density

The density of water is a function of the temperature, and is obtained from Pruppacher and Klett [52]. The equation is as follows, and is plotted in Fig. 2.5.

i) *for* $T \geq T_{tr}$

$$\rho_l \text{ [kg/m}^3\text{]} =$$

$$\rho_{tr} \frac{A_0 + A_1 (T/T_{tr}) + A_2 (T/T_{tr})^2 + A_3 (T/T_{tr})^3 + A_4 (T/T_{tr})^4 + A_5 (T/T_{tr})^5}{B_0 + B_1 (T/T_{tr})}$$

ii) *for* $T < T_{tr}$

$$\rho_l \text{ [kg/m}^3\text{]} = \rho_{tr} \times (A_6 + A_7 (T/T_{tr}) + A_8 (T/T_{tr})^2)$$

Where, $\rho_{tr} = 999.84 \text{ kg/m}^3$, which is a liquid density at the triple point temperature, $T_{tr} = 273.15\text{K}$. The other constants are given in table 2. 2.

Table 2. 1. Constants for liquid density equation

$A_0 = -2.0079$	$A_3 = -10.447$	$A_6 = 0.17058$	$B_0 = -3.9603$
$A_1 = -3.5552$	$A_4 = 3.8244$	$A_7 = 1.6353$	$B_1 = 4.9603$
$A_2 = 13.784$	$A_5 = -0.59812$	$A_8 = -0.80593$	

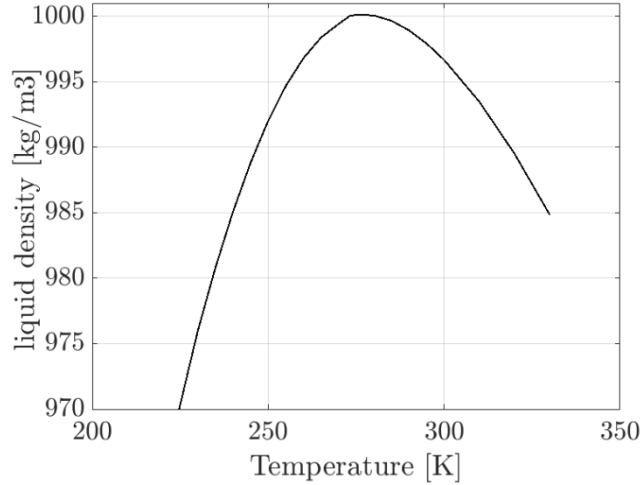


Figure 2. 5. Liquid density of water.

2.4.3. Vapor pressure

For the calculation of equilibrium vapor pressure, Sonntag and Heinze's formation [53] is adopted, and equation is as follows.

$$p_{v,eq} = \exp(A_9 + A_{10}T + A_{11}T^2 + C_0 \ln(T) + C_1/T) [N/m^2]$$

Table 2. 2. Constants for equilibrium vapor pressure

$A_9 = 21.125$	$C_0 = 2.4576$
$A_{10} = -2.7246 \times 10^{-2}$	$C_1 = -6094.4642$
$A_{11} = 1.6853 \times 10^{-5}$	

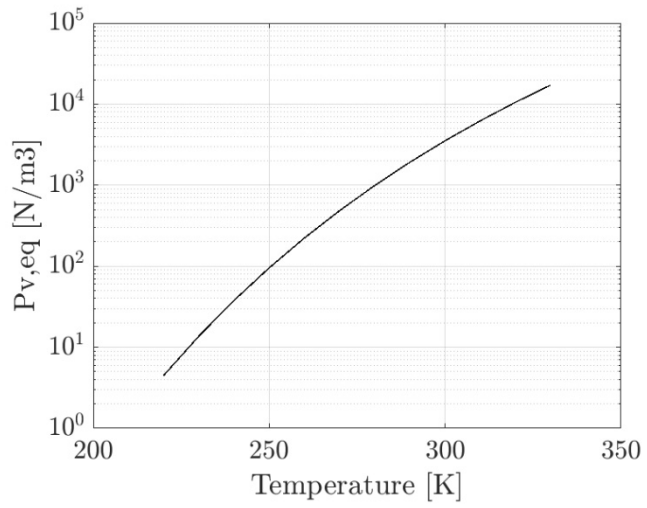


Figure 2. 6. Equilibrium vapor pressure of water.

Chapter 3. Experimental Facility

3.1 Transonic compressor cascade tunnel

A new transonic cascade wind tunnel has been design and built in Agency for Defense Development (ADD). This facility has been design for the compressor/fan cascade experiments for Mach number range 0.3 to 1.4. This chapter covers the specifications of wind tunnel, test section, test blade geometry, and wind tunnel flow qualities.



Figure 3. 1. A new transonic cascade wind tunnel.

3.2. Transonic wind tunnel

3.2.1. Wind tunnel facility

A new transonic cascade wind tunnel is a two-dimensional, open-loop type linear

cascade wind tunnel and its schematic is shown in Figure 3.2. Air is supplied at up to 10 bar by a 4-stage centrifugal compressor (750 kW), and its mass flow rate is about 11 kg/s. Flow is then throttled by a pressure regulator valve down to 5 bar, and another control valve is used for fine control of the inlet total pressure downstream of the regulator valve. Inlet total temperature is controlled via intercoolers which are located between the compressor stages. Thus, total pressure and total temperature can be independently controlled. Downstream of the pressure valves, there are four nozzles for water droplet injection. Thus, the flow is humidified by evaporation of droplets. The humidified flow is then stabilized in the settling chamber (dimensions of 1m × 1m) before being directed to the test section. The inlet Mach number is controlled via throttle valve which is located downstream of the test section. Flow is then directed to the silencer, and out. The detailed descriptions and pictures of each parts are listed in the Appendix A.

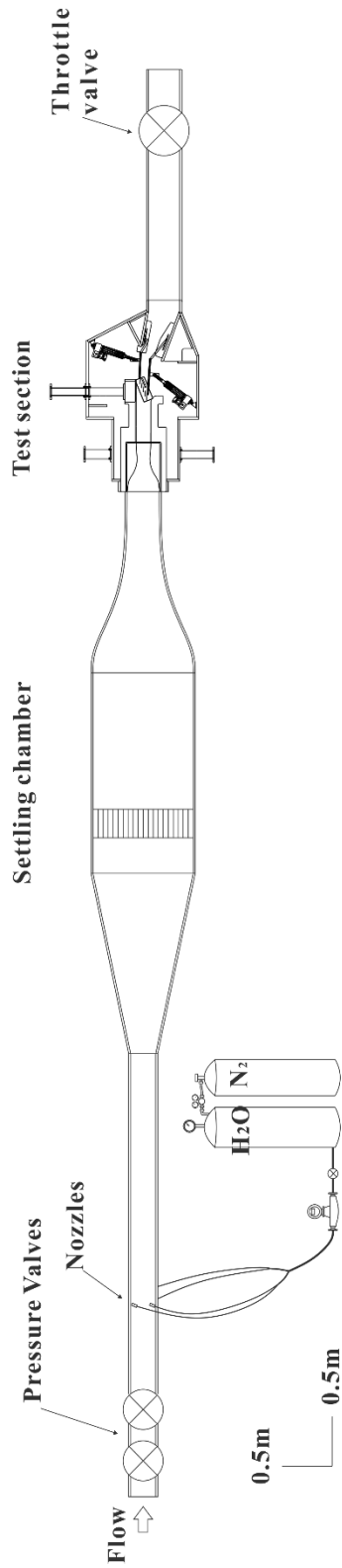


Figure 3. 2. Schematic of wind tunnel.

3.2.2. Water supply system

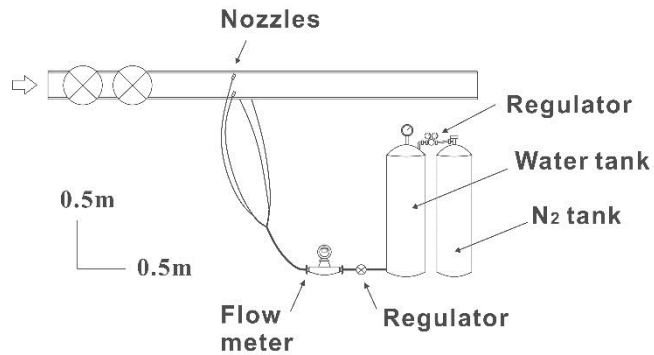
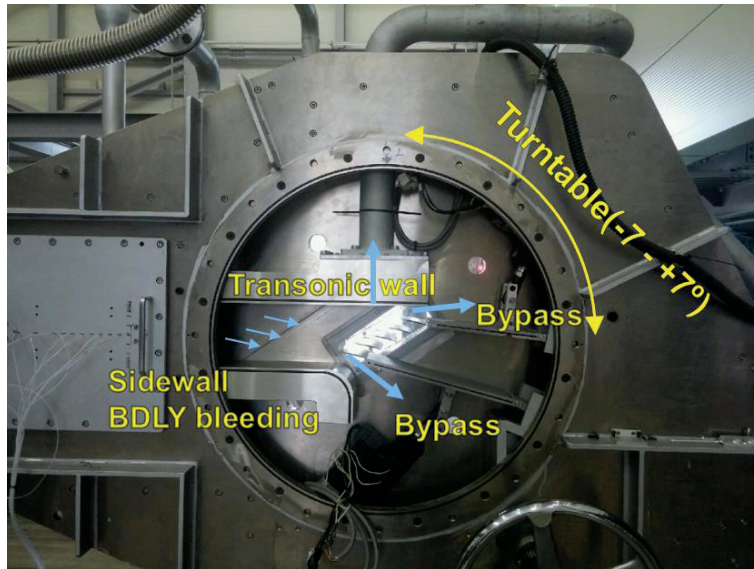


Figure 3. 3. Schematic of water supply system

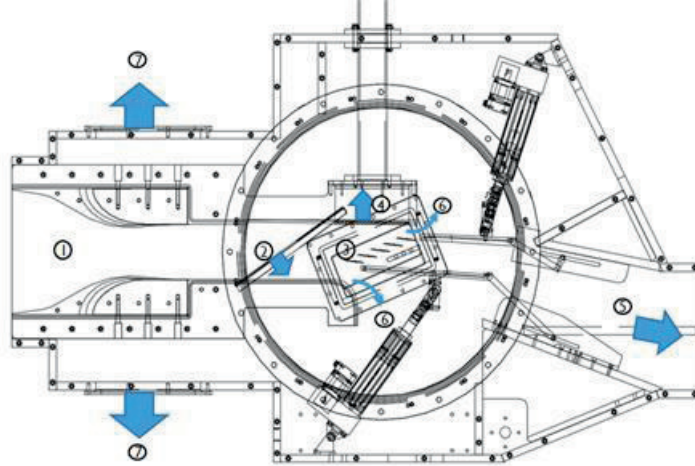
There is a water supply system upstream of a settling chamber. The water supply system is constructed to humidify the air, and it is composed of 4 nozzles (which are mounted on the duct (\varnothing 255mm) at 90° intervals), a water tank, a regulator, and a flow meter. The type of nozzle is an air-atomizing nozzle. Pressurized air (about 4 bar) is supplied from a separate line, and it atomizes water droplets to a micron size. Therefore, all the droplets can evaporate in a short time, thus, there are not remaining droplets in the test section. Also, to supply the desired flow rate, water have to be pressurized. Therefore the water tank (36 liter) is pressurized to 10 bar by connecting the nitrogen gas container, and the flow rate is controlled by a regulator and monitored via a flow meter. The detailed specifications and pictures are shown in Appendix A.

3.3. Test section

The test section (Figure 3.4) is composed of supersonic nozzle, parallel section, sidewall boundary layer bleeding slot, transonic wall, cascade, and tailboards, and it is designed based on the transonic cascade tunnel in German Aerospace Center (DLR) [54, 55, 56]. The test section has 120 mm X 140 mm dimension, and 5 blades are mounted on a turntable to enable incidence variation from -7 to +7 degree. There is a sidewall boundary layer bleeds system upstream of the cascade to minimize the side wall boundary layer effects on the cascade flow field. It is designed based on Harloff et al. [57]'s results with considering the expected boundary layer thickness (the designed shape is shown in the Appendix A). For a transonic operation, the upper wall of the test section is porous and equipped with a bleeds system. It is referred to as the "transonic wall", and enables a continuous transition from a subsonic flow to supersonic one, and facilitates stable test condition at inlet Mach number of 1.0. In addition, the transonic wall enables periodic flow by minimizing shock reflection from the test section ceiling. The transonic wall is designed based on the Grunet [58]'s results, and the designed shape is shown in Appendix A. There are two bypass passages on the upper and lower parts of the cascade. These passages are separated from the main flow, and controlled via valves to achieve a periodic flow.



(a)



- ① Nozzle,
- ② Boundary layer bleed slot
- ③ cascade
- ④ Transonic wall
- ⑤ Main flow going to throttle valve
- ⑥ Bypass passage
- ⑦ bypass flow

(b)

Figure 3. 4. Test section: (a) picture, (b) schematic.

3.4. Test blade

The test blade was designed by Hanwha Aerospace as a rotor tip shape of the 1st stage of the transonic compressor (Figure 3.5), and the blade geometry parameters are summarized in Table 3.1. The blades aspect ratio is 2.4 to minimize the side wall effects, and the blades are supported by plexiglass sidewalls which enable optical access.



Figure 3. 5. Test blades.

Table 3. 1. Blade geometry parameters

Number of blades	5
Chord length (c)	50 mm
Aspect ratio (Z/c)	2.4
Solidity (c/S)	1.326
Stagger angle	144.5°

3.5. Instrumentation

3.5.1. Data reduction and measuring method

For the cascade experiments, inlet Mach number, incidence, and relative humidity have been simulated as the inlet conditions. To estimate the cascade performance, pressure coefficient, deviation, and loss coefficient have been measured. The results of data reduction are listed in Table 3.2 with its definition.

Table 3. 2. Data reduction

Inlet Mach number, M	$\sqrt{5 \left[\left(P_{t,1} / \overline{P_{s,1}} \right)^{\gamma-1/\gamma} - 1 \right]}$
Incidence, i	$\alpha_1 - \beta_1$
Relative humidity, RH	$P_v / P_{v,eq}$
Pressure coefficient, C_p	$(P - P_{s,1}) / (P_{t,1} - P_{s,1})$
Loss coefficient, Y_p	$(P_{t,1} - P_{t,2}) / (P_{t,1} - P_{s,1})$
Deviation, δ	$\alpha_2 - \beta_2$

The inlet Mach number, M , is calculated from the inlet total pressure $P_{t,1}$ which is measured in the settling chamber with a Kiel probe (AEROPROBE, tip diameter 4.76 mm, E-type thermocouple) and the inlet static pressure $\overline{P_{s,1}}$ which is measured by averaging pressure values from the 16 static holes (\varnothing 0.5 mm) which are located at $x/Cx = -0.5$. Another 16 static holes are located at $x/Cx = 1.4$ (downstream of cascade), thus, periodicities of inlet and outlet flows can be checked. These static

taps cover the 2nd ~ 4th passages, thus, periodicity in the vicinity of the measurement passage (3rd passage) can be verified. Following a Steinert et al. [59]’s method, incidence is calculated by comparing the blade loading of the leading edge region of the suction surface with CFD results. For the blade loading measurement, 10 static pressure taps (\varnothing 0.3 mm) are distributed each on the suction surface of the 3rd blade and on the pressure surface of the 4th blade, and normalized with pressure coefficient, C_p . The location of blade static taps are listed in Appendix B. A 3-hole probe (VECTOR FLOW, bent type, tip diameter of 1.6 mm) is located at $x/C_x=1.4$ and traversed by 1mm intervals in pitch-wise direction by connecting a traverse system (Velmex). Thus, the distributions of total pressure, $P_{t,2}$ and flow angle, β_2 at $x/C_x= 1.4$ can be measured. The instrumentations and its measuring variables are listed in Table 3.3.

Table 3. 3. Measurement variables and method

Variable	Instrumentation	location
Inlet total pressure, $P_{t,1}$	Kiel probe	Settling chamber
Inlet total temperature, T_t	Kiel probe	Settling chamber
Inlet static pressure, $P_{s,1}$	Static taps	at $x/C_x = -0.5$
Static pressure, P_s	Static taps	on the blade surface
Outlet total pressure, $P_{t,2}$	3-hole probe	at $x/C_x=1.4$
Deviation, δ	3-hole probe	at $x/C_x=1.4$

For the shock image capturing, Schlieren method has been adopted. The Schlieren method is a method to visualize density variations in transparent media. It records gradients in the refractive index of transparent media, such as air. A schematic of this method is given in Figure 3.6. In this experiment, Schlieren setup is composed of a light source (Zenon lamp, 500W), two concave mirrors (\varnothing 150 mm, focal length 1.5 m) one flat mirror, knife edge, and camera (1/3 inch CCD camera). The light source is a point light source (a small orifice is located in front of the Zenon lamp), and it is located 1.5 m (focal length of concave mirror) away from the concave mirror. Thus, the light is changed to the parallel beam from the first concave mirror, then, it penetrates the test section through optical window. The penetrated parallel beam converges to a point from the second concave mirror. In this experiment, another plane mirror is used due to spatial constraint, and the camera is located right after the focal point.

Density gradients in the test section in the direction perpendicular to the direction of light cause the light to deflect. This deflection cause a light cannot be converged in a point. Thus, it records the change in refractive index due to the air density difference upstream and downstream the shock as contrast of light. Knife edge is located between the focal point and camera for magnifying the contrast by blocking the deflected light. The detailed pictures of Schlieren device are shown in the Appendix B.

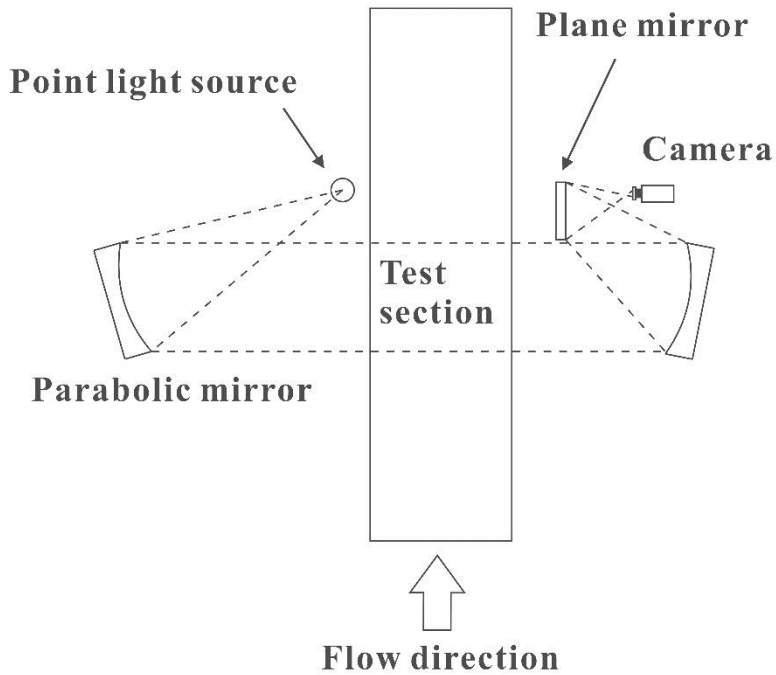


Figure 3. 6. Schematic of Schlieren device.

3.5.2. Sensors

For the pressure measurement in Kiel probe, 3-hole probe, and static taps, three Netscanner PSI 9116 16-channel sensors (accuracy of 0.05% of full scale: 0.1 kPa / 206 kPa) have been used, thus, all the measurement data are acquired in a same time. For the steady measurement, it gives a pressure by averaging the 2000 data in a sampling rate of 500Hz. To measure relative humidity in the settling chamber, an HMT331 (VAISLA, accuracy: 1% of reading) sensor has been adopted. For the flow rate measurement, flowmeter of PROMASS 80F (Endress Hauser, accuracy: 0.15% of reading) has been adopted.

3.5.3. Uncertainty

Uncertainty of measured parameters are calculated following the Coleman et al.

[60] and Taylor [61]’s methods based on the sensor accuracy. Detailed methods are described in the Appendix D, and the results of calculated uncertainty with 95% confidence interval are summarized in Table 3.4.

Table 3. 4. Uncertainty of measurement variables

Inlet Mach number, Ma	$\pm 0.1\%$
Incidence, i	$\pm 0.5^\circ$
Loading coefficient, C_p	$\pm 1\%$
Loss coefficient, Y_p	$\pm 2.5\%$
Deviation, δ	$\pm 0.5^\circ$
Relative humidity, RH	$\pm 1\%$

3.6. Wind tunnel flow quality

The transonic cascade wind tunnel is a newly designed and built for this experiments. Therefore, before conducting the cascade experiments, flow quality test has been conducted. To check the flow symmetry about tunnel centerline, static pressure is measured in the nozzle part. For the flow uniformity check in the test section (parallel part), the total/static pressure are measured in the test section without cascade. Following sections show the test results of wind tunnel flow quality.

3.6.1. Flow in the nozzle part

Due to the symmetric geometry of test section about the centerline, flow should be symmetric. Therefore, to verify the flow symmetry in the nozzle part, static

pressure taps are located on the nozzle cover at inlet and outlet of nozzle as shown in Figure. 3.7, and the locations of static taps are listed in Table 3.5. The test has been conducted for the two Mach number cases ($Ma= 0.6, 1.0$), and the measured static pressure is converted to the Mach number by isentropic equation and plotted in Figure 3.8. The result shows the symmetric flow about the centerline, thus, it is concluded that the nozzle flow is symmetric.

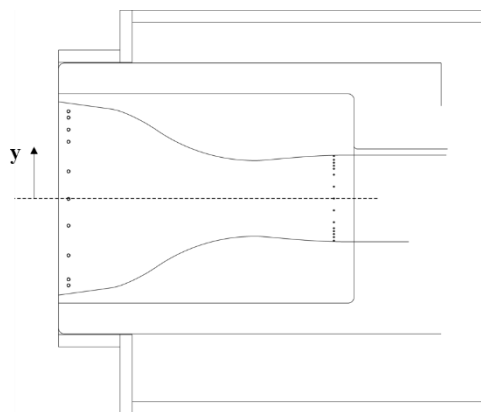
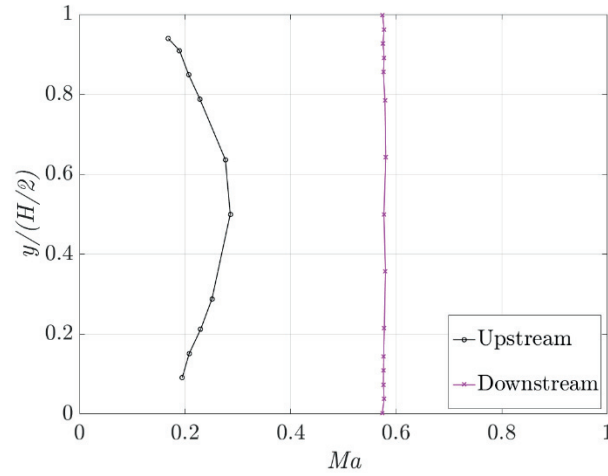


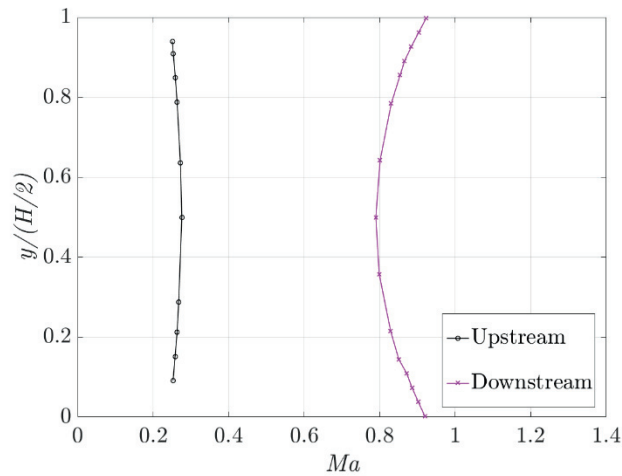
Figure 3. 7. Static tap location.

Table 3. 5. Location of static taps

Static tap #	Nozzle inlet	Nozzle outlet
1	0.09	0.0025
2	0.15	0.038
3	0.21	0.074
4	0.29	0.109
5	0.50	0.144
6	0.64	0.215
7	0.79	0.358
8	0.85	0.500
9	0.91	0.642
10	0.94	0.784
11		0.855
12		0.891
13		0.926
14		0.962
15		0.998



(a)



(b)

Figure 3. 8. Flow quality at the nozzle inlet & outlet: (a) Ma=0.6, (b) Ma=1.0.

3.6.2. Flow in the test section

There is a parallel section after the nozzle, thus, uniform flow have to be constructed at the end of parallel section where the cascade will be positioned. Thus, to check the flow uniformity, static/total pressure have been measured via pitot probe at 5 different locations, and the probe has been traversed in the spanwise (normal to the sidewall) to cover the whole test section. The measurement locations of pitot probe are shown in Figure 3.9 and listed in Table 3.6. The measured static/total

pressure are converted to Mach number as shown in Figure 3.10. For 5 different location, Mach number distribution shows identical values, thus, flow uniformity is verified.

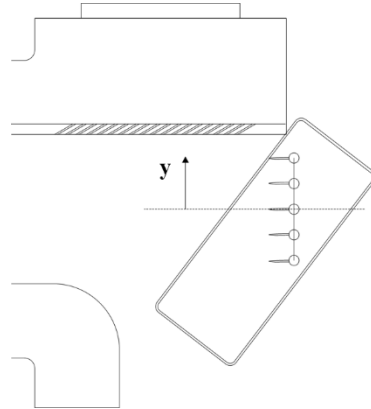
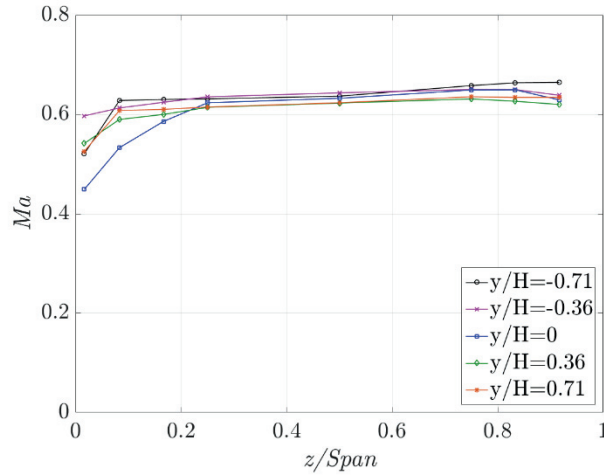


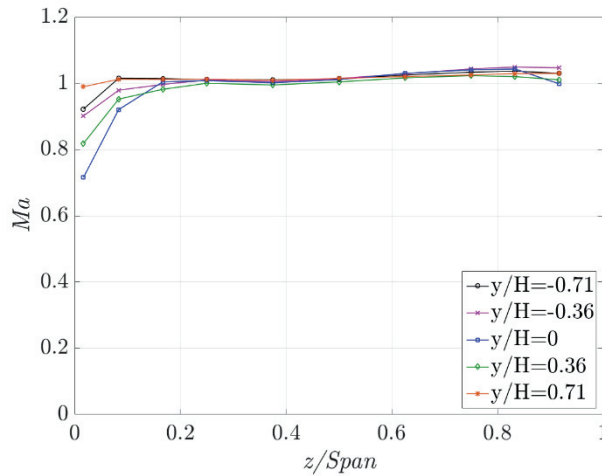
Figure 3. 9. Measurements location at test section.

Table 3. 6. Location of static/total pressure measurement

Probe number	Location, $y/(H/2)$
1	0.71
2	0.36
3	0
4	-0.36
5	-0.71



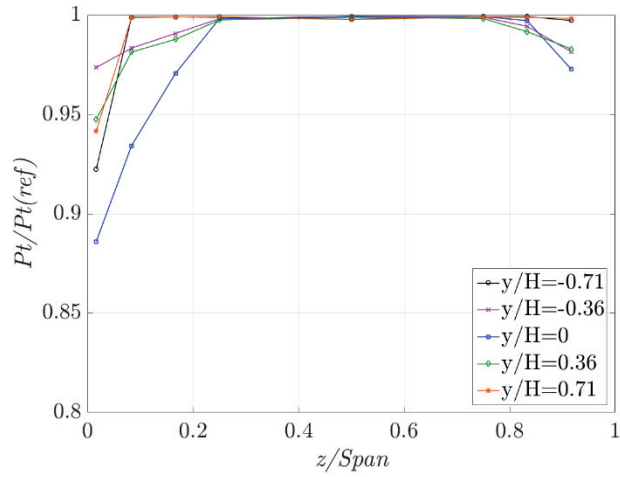
(a)



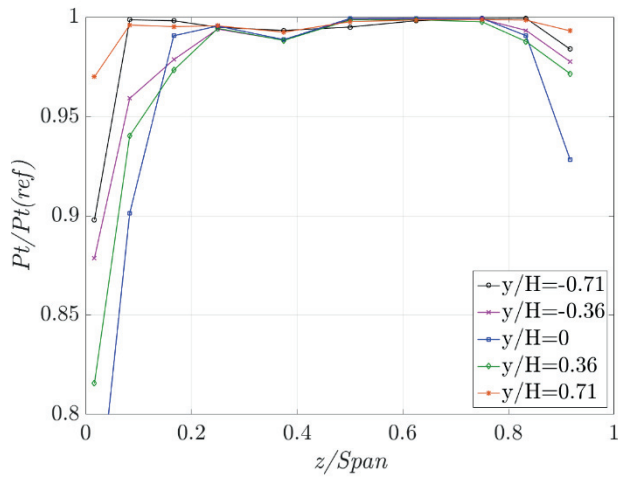
(b)

**Figure 3. 10. Span wise Mach number distribution at test section: (a) Ma=0.6
(b) Ma=1.0.**

In addition, to verify the validity of using total pressure in the settling chamber as inlet total pressure of cascade, total pressures measured at test section are compared with a total pressure measured at settling chamber. Figure 3.11 shows the normalized total pressure distribution following the span-wise location at 5 different locations. The result verifies the validity of using total pressure measured at settling chamber as a cascade inlet total pressure.



(a)



(b)

Figure 3. 11. Span-wise normalized total pressure distribution at test section:
 (a) Ma=0.6 (b) Ma=1.0.

Chapter 4. Experimental Results

4.1 Test matrix

The compressor cascade performance is measured at the inlet condition of Mach number 1.11, and incidence angle of $+5^\circ$. The inlet Mach number 1.11 represents the typical tip Mach number of a modern transonic compressor and the relatively high incidence angle of $+5^\circ$ represents the operating point near stall. As the incidence angle increases, strong expansion occurs near the suction surface. Thus, to show the strong effects of condensation near the suction surface, the high incidence angle has been selected. The humidity effects have been studied for 6 different relative humidity conditions at a fixed total pressure, P_t , and total temperature, T_t . Test conditions are listed in Table 4.1.

Table 4. 1. Test conditions

Total Pressure, P_t	210 kPa
Total Temperature, T_t .	309K
Mach Number, M	1.11
Incidence, i	$+ 5^\circ$
Relative humidity, RH	20, 32, 42, 45, 49, 53%

4.2 Cascade flow quality

4.2.1. Upstream and downstream periodicities

In the cascade experiments, it is essential to verify the periodicity of upstream and

downstream flow because the cascade simulates the compressor flow field (i.e. periodic incoming/outgoing flows). The upstream and downstream periodicities have been measured via each 16 static taps which are located at $x/Cx = -0.5$ and 1.4 . These static taps cover 2nd to 4th passages, thus, flow periodicity can be checked around the measurement passage (3rd passage). Figure 4.1 shows the pressure coefficient distributions at inlet static taps showing the repeated peaks and lows (i.e. periodic flow). Although the peak values are slightly decreasing as pitch increases, its absolute value is relatively small when it is converted to Mach number: lower than 0.02. Thus, it can be concluded that the periodicity of inlet flow is verified.

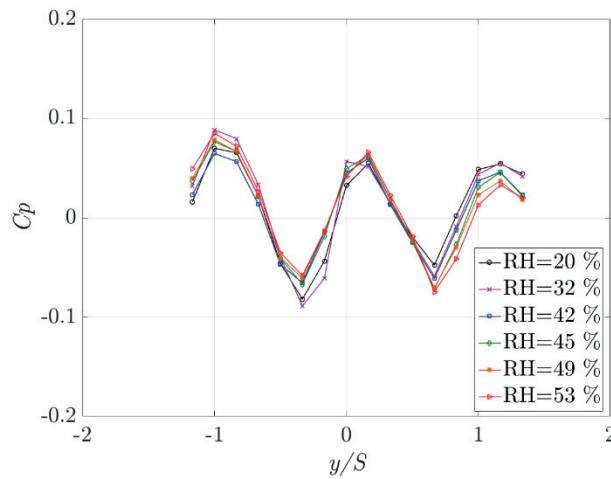


Figure 4. 1. Inlet periodicity.

The outlet flow of compressor shows the almost uniform static pressure distributions following a pitch-wise location. Therefore, making the periodic outlet flow is relatively easy one once the inlet periodicity is verified by adjusting the tail board. Figure 4.2 shows the pressure coefficient distribution measured at outlet static taps. The results show almost uniform static pressure distributions with relatively

small peaks and lows. The low value at $y/S=1.25$ shows relatively small compared to neighboring low values, however, when it is converted to Mach number, the difference of its absolute value is lower than 0.01. Thus, as same as inlet flow, outlet flow periodicity is verified.

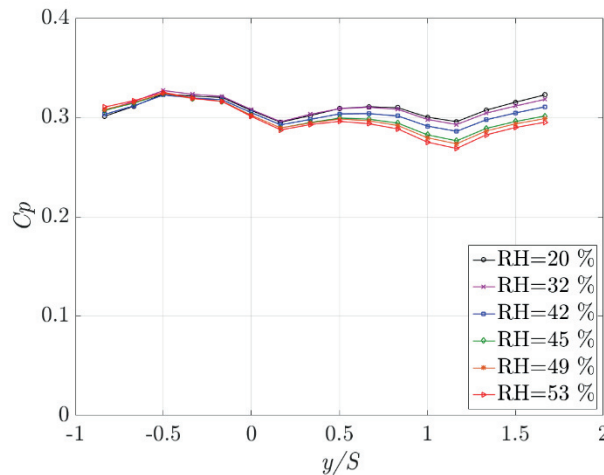


Figure 4. 2. Outlet periodicity.

4.2.2. Axial Velocity Density Ratio

The compressor cascade is the device that simulates the compressor flow field at a specific span location. Thus, the cascade is designed for the 2 dimensional flow. However, in the experiment, due to the boundary layer on the sidewalls, the flow is not 2-dimensional due to the stream tube contraction. Especially, in case of the compressor cascade where the adverse pressure gradient exists, its effects become strong and affects the cascade performance. The Axial Velocity Density Ratio (AVDR) represents how much the stream tube is contracted. The AVDR is defined by the ratio between the axial velocity density ratio of inlet and outlet flows as a follow.

$$AVDR = \frac{V_{ax,2}\rho_2}{V_{ax,1}\rho_1} \quad (4.1.)$$

The thickened boundary layer changes the cascade flow field and cascade performance. Schreiber et al. [31] measured the deviation and loss coefficient for various AVDR values and found that as AVDR value increases from 1 to 1.12, deviation and loss coefficient decreases up to 2°, and 10% for each. Therefore, to see only the humidity effects on the cascade performance, keeping the AVDR value constant is important. The measured AVDR values for various humidity conditions are listed in Table 4.2 (detailed measurement methods are represented in Appendix E). For the 6 humidity conditions, the AVDR values almost keep constant around a value of 1.07. Thus, it is concluded that the experimental results of humidity effects on the cascade performance are free from the AVDR effects.

Table 4. 2. AVDR values

RH	AVDR
20%	1.07
32%	1.08
42%	1.08
45%	1.08
49%	1.07
53%	1.07

4.3 Blade loading distribution

Blade loading is represented by pressure coefficient distribution on the suction and pressure surface. It is an important factor not only for designing the blade, but also for analyzing the flow field because it represents the flow characteristics in the passage. Figure 4.3 shows measured pressure coefficient distributions on the suction surface of 3rd blade and on the pressure surface of 4th blade for varying the relative humidity. The lowest relative humidity condition is 20%, thus, it is referred to as baseline flow. For the baseline flow, on the suction surface, slight acceleration (decrease of C_p) from $x/C_x = 0.2$ to 0.4 , shock at $x/C_x = 0.4$, and flow diffusion (increase of C_p) downstream of the shock are the characteristics. On the pressure surface, the continuous diffusion (increase of C_p) is shown. Schlieren images in Fig. 4.4 (a) help the understandings of the flow field. Schlieren images covers the flow field from 2nd blade to 5th blade, and the 3rd blade is marked with a white line. Since the optical window was machined so that the blade can be inserted, a change in the refractive index was caused. Therefore, parallel light passing through this region could not be collected in a focus again in front of the camera, thus this regions are appeared with black in the images. However, the other regions are shown clearly (inlet static taps and tubing, tubing of static taps on the 3rd blade of the suction surface and the 4th blade of the pressure surface).

For a RH 32% condition, there are negligible changes on the blade pressure coefficient distribution, however, as relative humidity increases further, 1) pressure coefficient on the suction surface increases, 2) shock location shifts to downstream, and 3) pressure coefficient on the pressure surface decreases. These changes are

come from the effects of condensation and similar results have been observed in the previous researches – in the researches of converging–diverging nozzle [21], single airfoil [26, 27, 62], steam turbine [63, 64], and compressor cascade [32]. As the flow experiences strong expansion near the leading edge of suction surface (where, from $x/Cx= 0$ to 0.4), temperature decreases abruptly, thus, equilibrium vapor pressure $P_{v,eq}$ decreases. Therefore, supersaturation rate s of vapor becomes increase; the vapor becomes supersaturated (i.e. $s > 1$); and the non-equilibrium condensation occurs. When the condensation occurs, latent heat is added to the supersonic flow increasing static pressure (the pressure drop due to condensation-inducing vapor mass reduction is negligible compared to the pressure increase due to heat addition from condensation - Appendix G. The flow property change due to heat addition follows the Rayleigh equation - Appendix F). Thus, from the increase of pressure coefficients upstream of the shock on the suction surface, it can be concluded that the condensation has been occurred. Furthermore, as the condensation increases the static pressure upstream of the shock, shock is pushed downstream. (the effect of increasing mass flow rate due to the water injection on the shock location shift is negligible - Appendix H). The shifts in shock location can be seen in the Schlieren images by comparing it with the shock at baseline flow. The shock location shifts from $x/Cx= 0.41$ at RH 20% condition to $x/Cx= 0.54$ at RH 53% condition. On the other hand, since condensation decreases the shock front Mach number (i.e. C_p value upstream of the shock increases), shock strength decreases. Thus, pressure coefficient near the leading edge of pressure surface decreases as relative humidity increases.

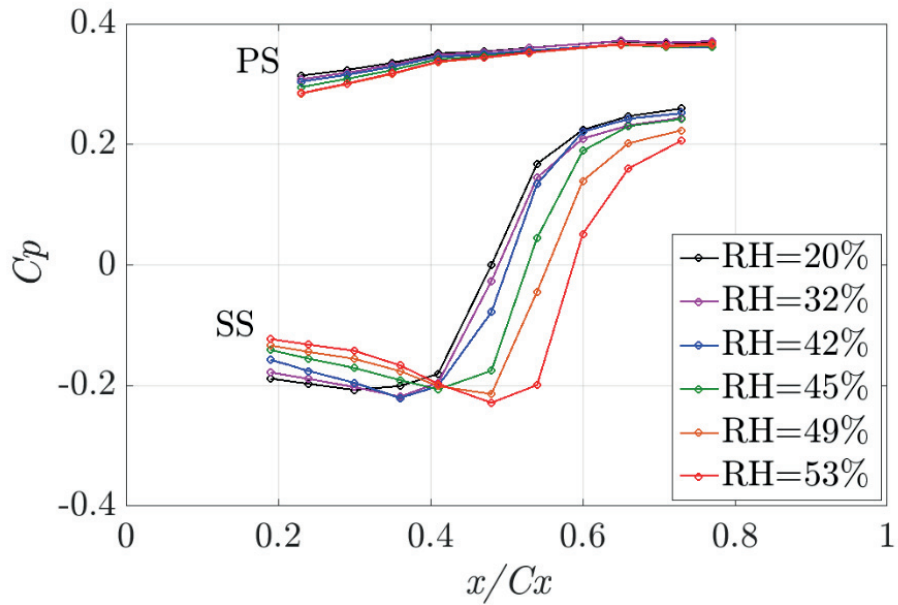
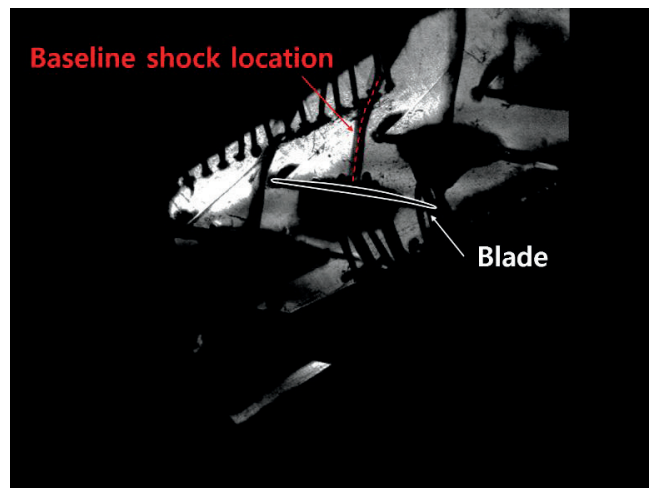
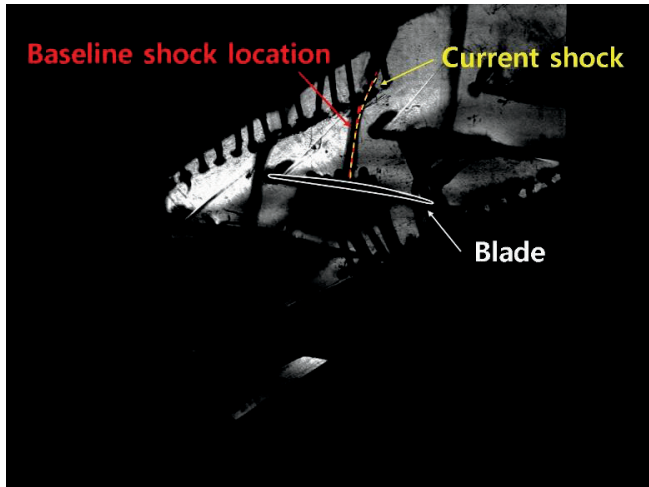


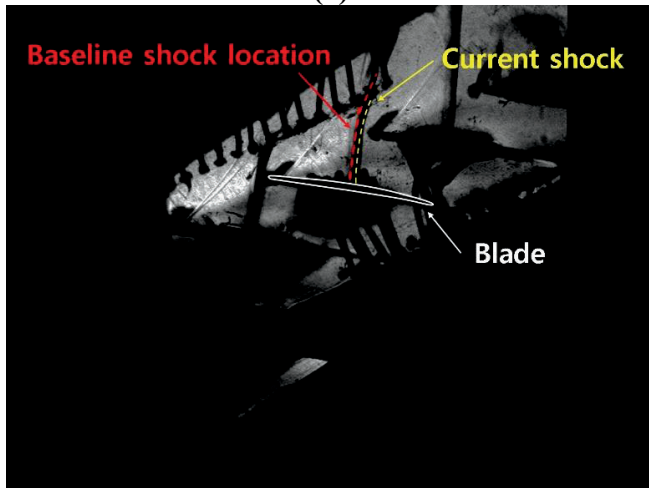
Figure 4. 3. Pressure coefficient distribution vs. axial location.



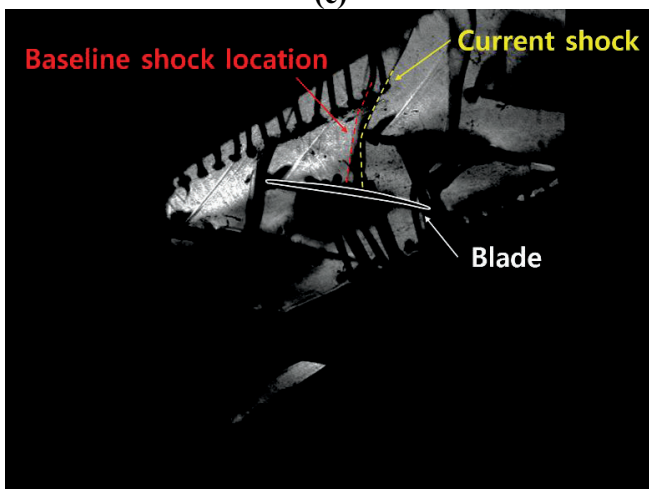
(a)



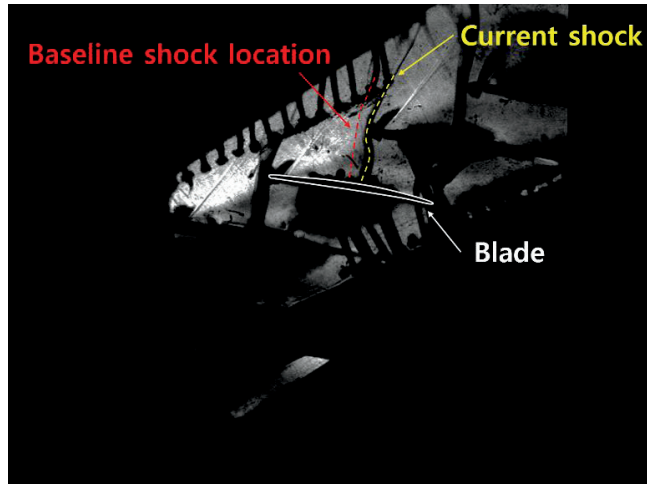
(b)



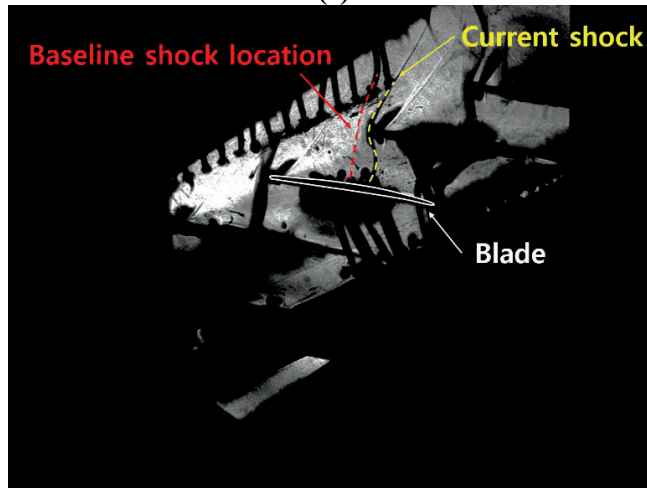
(c)



(d)



(e)



(f)

Figure 4. 4. Schlieren images: (a) RH= 20%, (b) RH=32%, (c) RH= 42%, (d) RH= 45%, (e) RH= 49% (f) RH= 53%.

4.4 Deviation

Deviation, δ , is a variable which shows the difference between the flow angle, α_2 and the blade angle, β_2 at the trailing edge. In the compressor blade designing, deviation represents how effectively energy is delivered to the flow. Furthermore, since it is the inlet angle of stator, it is an important factor deciding the stage matching. Figure 4.5 shows the mid-span deviation distribution measured at

$x/C_x=1.4$ following the pitch-wise direction (intervals of $\Delta y/S = 0.026$). As relative humidity increases, the decrease of deviation can be expected because condensation decreases the shock strength and decreases the shock-induced boundary layer separation, thereby. However, in the experimental results, humidity has negligible effects on deviation. Mass-averaged value of deviation (Table 4.3) also shows negligible changes under the uncertainty (uncertainty of deviation is 0.5°).

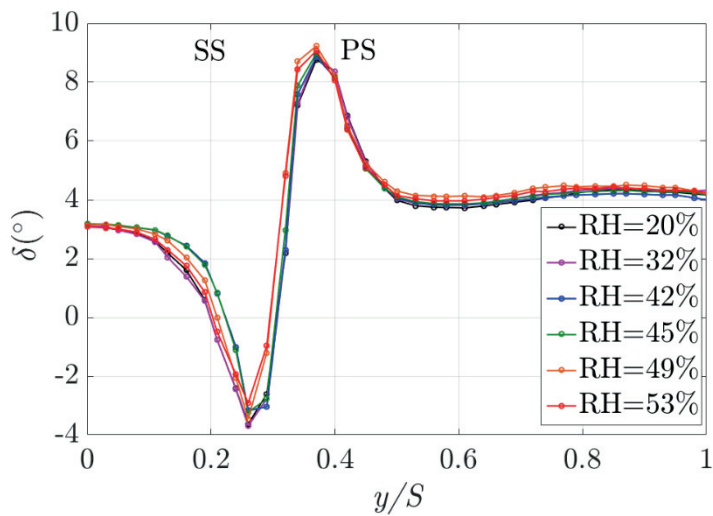


Figure 4. 5. Mid-span deviation distribution vs. pitch at $x/C_x=1.4$.

Table 4. 3. Mass averaged deviation.

RH (%)	δ ($^\circ$)
20	3.4
32	3.4
42	3.5
45	3.6
49	3.7
53	3.6

To figure out the negligible humidity effects on the deviation, wake displacement thickness has been calculated and listed in Table 4.4. The normalized wake displacement thickness value is 0.022 which represents the negligible shock-induced boundary layer separation. Thus, it can be concluded that due to the negligible shock-induced boundary layer separation in the baseline case, the effects of humidity decreasing the shock-induced boundary layer separation has been shown negligible.

Table 4. 4. Normalized wake displacement thickness.

RH (%)	δ^*/S
20	0.022
32	0.022
42	0.020
45	0.020
49	0.022
53	0.022

4.5 Loss coefficient

4.5.1. Humidity effects on the loss coefficient distribution

The loss coefficient, Y_p , along with the deviation, is one of the main parameters which shows the cascade performance. It directly represents the decrease in total pressure across the cascade. Figure 4.6 shows the mid-span loss coefficient distribution measured at $x/Cx=1.4$ following the pitch-wise direction. The mid-span loss coefficient can be divided with two regions - wake region (from $y/S= 0.2$ to 0.4) and main passage region (where, outside of wake region). The wake region is where the blade boundary layer mix with the main passage flow. Therefore, blade boundary

layer governs the wake loss. However, as shown in the wake displacement thickness in Table 4.4, relative humidity has negligible effects on the boundary layer thickness, thus, wake loss shows negligible changes. On the other hand, the loss coefficient in the main passage increases with relative humidity increases, especially, noticeable changes near the suction surface (where, $y/S= 0 \sim 0.3$). The reason of increasing loss in the main passage is caused by a heat addition from condensation and this type of loss has been known in the steam turbine researches [30, 31]. When condensation occurs, latent heat is added to the flow increasing entropy and decreasing total pressure. Consequently, due to the condensation in the cascade passage, the loss coefficient increases as relative humidity increases. Especially, near the suction surface (where, $y/S= 0 \sim 0.3$) where the intensive condensation occurs, the loss increase is shown clearly. As a result, mass-averaged loss coefficient (listed in Table 4.5) has increased as relative humidity increases, and it at 53% relative humidity has increased about 29% compared to 20% relative humidity.

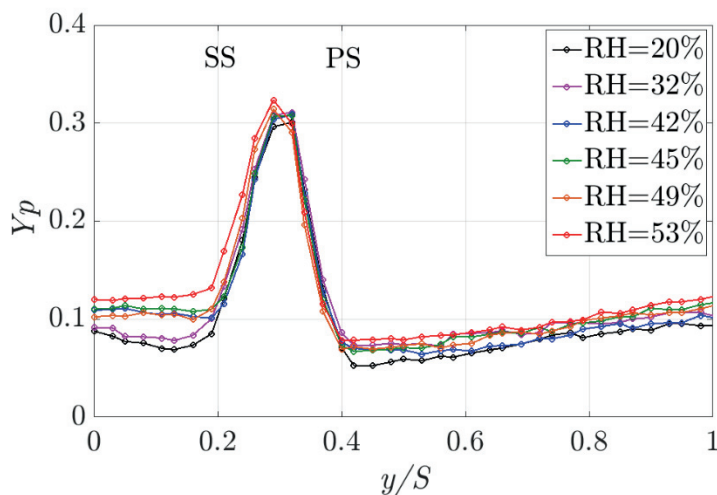


Figure 4. 6. Mid-span loss coefficient distribution vs. pitch at $x/C_x=1.4$.

Table 4. 5. Mass averaged loss coefficient.

RH (%)	Y_p^m
20	0.098
32	0.110
42	0.107
45	0.114
49	0.115
53	0.123

4.5.2. Cascade loss composition

The cascade loss measured at $x/C_x = 1.4$ can be divided by wake loss region and main passage loss region. Following the Geist et al. [32], the wake region is defined by the location up to where the velocity reaches 99% of the averaged velocity value in the main passage. The mass-averaged wake loss coefficient is calculated as a follow.

$$Y_{P, wake}^m = \frac{\int_{V \rightarrow 0.99\bar{V}} (\rho V_x Y_P) d(y/S)}{\int_0^1 (\rho V_x) d(y/S)} \quad (4.2)$$

The main passage loss is defined by subtracting the mass averaged wake loss coefficient, $Y_{P, wake}^m$, from the total mass averaged loss, Y_P^m . The definition is as a follow.

$$Y_{P, main}^m = Y_P^m - Y_{P, wake}^m \quad (4.3)$$

Figure 4.7 shows a cascade loss composition. In the baseline case, the cascade loss

is composed of 54% of wake loss and 46% of main passage loss. As relative humidity increases, profile loss shows negligible changes, however, main passage loss increases, and it comprises 52% of total loss at 53% RH condition. Thus, it can be concluded that a main factor increasing loss coefficient is the main passage loss increase. The detailed analysis of the increased main passage loss is discussed in the Chapter 6 using the CFD results.

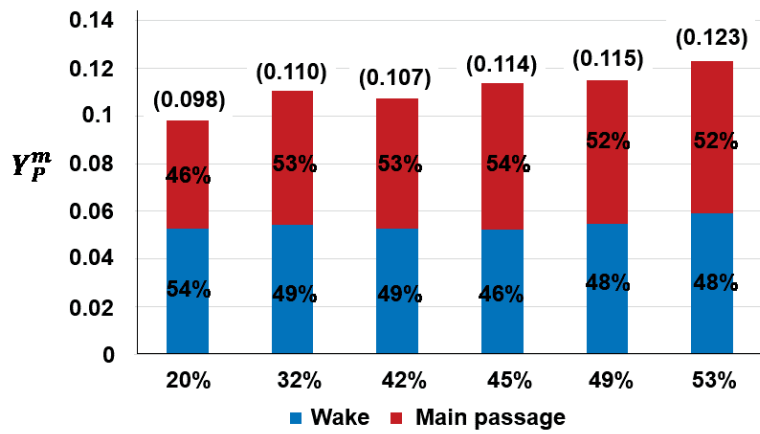


Figure 4. 7. Loss composition.

Chapter 5. Numerical Method

5.1 Introduction

In the transonic compressor cascade experiments, directly measuring the flow properties, such as pressure, and temperature, is restricted because inserting a measuring device (ex. probe) causes a shock disturbing the flow field. As an alternative, non-intrusive measuring method (ex. LDV, PIV) can be adopted, however, it is very time consuming, and its measurement variables are also very limited (usually only the velocity). Therefore, for the detailed analysis of the humidity effects on the compressor cascade flow field, numerical study has been conducted. Numerical calculation has been conducted via commercial program ANSYS FLUENT v. 17.0 by adopting the classical nucleation theory (CNT) and Hertz-Knudsen droplet growth model to simulate the non-equilibrium condensation. Calculation has been conducted with the identical inlet conditions as in the experiment.

5.2 Mesh construction

Mesh is constructed via ANSYS ICEM as shown in Figure 5.1. The calculation have been conducted with a one passage by imposing the periodic condition on the top and bottom of the calculation domain. Thus, it can simulate the flow of infinite rows of blade (i.e. cascade). The inlet domain is located at $x/Cx = -1$, thus, two shocks

which are generated from neighboring blades are positioned upstream of leading edge such as experiments (in experiments, measuring blade is a 3rd blade, thus, there are two shocks upstream of leading edge which are come from the neighboring blades). The outlet domain is located at $x/Cx= 2.5$ for the stable calculation residual control. For the fast calculation speed, the calculation domain covers from one side wall to mid span, thus, symmetry condition has been imposed at the mid span location. Furthermore, to match the AVDR value as in the experiments, span-wise length has been increased 1.5 times, thus, aspect ratio is changed to 3 (aspect ratio is 2 in experiment).

The O-grid has been adopted around the blade and H-grid has been adopted in the other part. The grid independence test has been conducted from the mesh number from 0.7 to 4.5 million, and the mass-averaged loss coefficient at $x/Cx= 1.4$ has been compared. Figure 5.2 shows a result of grid independence test. The mesh number of 1.5 Million has been adopted for the calculation.

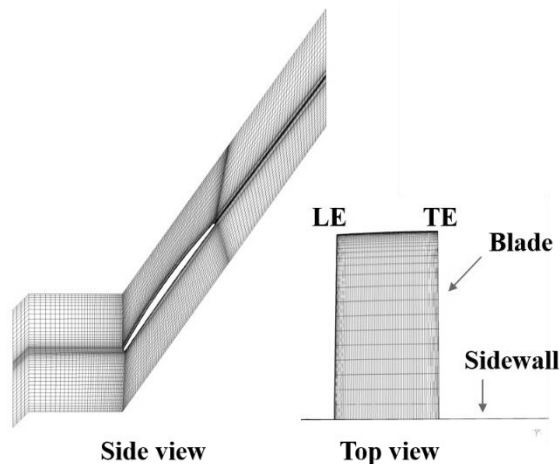


Figure 5. 1. Mesh.

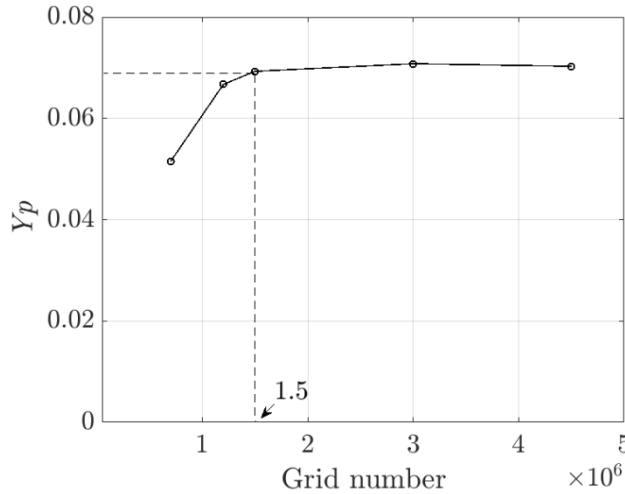


Figure 5. 2. Grid independence test.

5.3 Solver setting

The calculations have been conducted with ANSYS FLUENT v. 17.0. Steady state calculation conducted with Density-Based solver, thus, flow variables such as velocity, pressure and temperature have been calculated implicitly. SST turbulence model has been adopted for the viscous model, and ideal gas law and calorically perfect gas assumption have been adopted. For the Convective flux type, the Advection Upstream Splitting Method (AUSM) has been adopted. For the gradient, Green-Gauss cell based discretization method has been adopted, and for the flow discretization method, second order upwind scheme has been adopted.

For the boundary conditions, total pressure, total temperature, and flow angle have been imposed on the inlet, static pressure has been imposed on the outlet, and no slip wall condition with zero heat flux has been imposed on the walls. Periodic condition has been imposed on the top and bottom surface to simulate the cascade flow, and the symmetry condition has been imposed at mid-span to reduce the calculation time.

The boundary conditions are listed in Table 5.1.

Table 5. 1. Boundary condition

Boundary condition		Value
Inlet	P_t	210 kPa
	T_t	309K
	Mixing ratio	0.0035, 0.0056, 0.00746, 0.0080, 0.0087, 0.00945
Outlet	P_s	135 kPa

5.4 Strategy of condensation modelling

To simulate the condensation model which has been discussed in the Chapter 2, the function of User Defined Scalar (UDS) and User Defined Memory (UDM) have been adopted. For an arbitrary scalar, ϕ , the UDS function solves the below equations.

$$\frac{\partial \rho \phi}{\partial t} + \frac{\partial \rho u_i \phi}{\partial x_i} = S \quad i= 1, 2, 3. \quad (5.1)$$

Where S represents a source term, u_i represents a Cartesian velocity at x_i -direction. Thus, the Hill's method of momentum which representing the liquid phase (Eq. 2.37) can be calculated by solving 4 UDS equations. The UDM function has been used to making new thermodynamic parameters. Thus, the thermodynamic parameters, such as equilibrium vapor pressure, surface tension, latent heat,

nucleation rate, droplet growth rate, and etc. have been calculated, and used in the source term, S .

Figure 5.3 shows the calculation loop. From the previous calculation results (liquid mass fraction, g , temperature, T), the energy source term in the Navier-Stokes equation is calculated. Therefore, by adding the energy source term to the energy equation, the heat addition effects from the condensation to the compressor cascade flow field are calculated. After solving the Navier-Stokes equation, flow properties such as velocity, temperature, and pressure are updated. Then, to calculate the source terms in the liquid phase equation (i.e. Hill's method of momentum) from these new properties, all the thermodynamic parameters and the variables concerning condensation phenomenon are calculated. First, the partial pressure, density of each air and vapor are calculated, and stored in the UDMs (The temperature of air, droplets, and vapor are not calculated again under the assumption of identical temperature). Also, from the temperature information, the thermodynamic properties such as surface tension σ , latent heat L , liquid density property ρ_l , and equilibrium vapor pressure $P_{v,eq}$ are calculated and stored in the UDMs. Then, from these UDMs, the variables directly connected to condensation such as supersaturation rate s , critical droplet radius r^* , nucleation rate J , droplet radius r , and droplet growth rate \dot{r} are calculated, and stored in the UDMs. From these new information, liquid phase equation is calculated, thus, liquid mass fraction, g , is calculated. This process is repeated until the calculation converges.

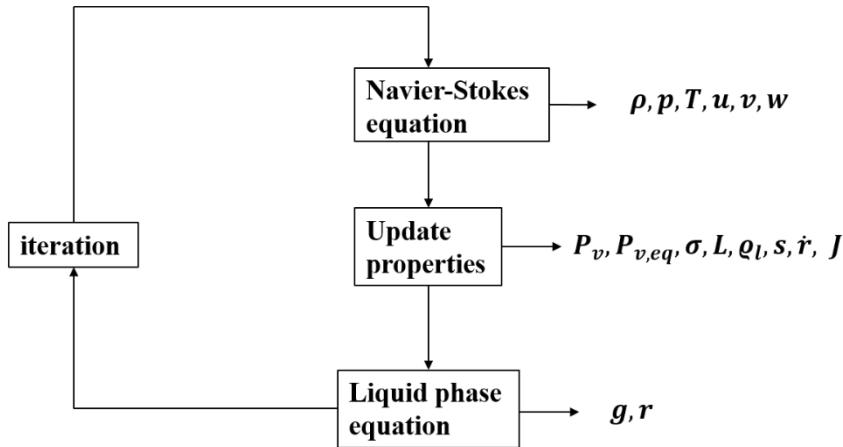


Figure 5. 3. Calculation strategy.

5.5 Validation of Numerical Method

The calculation strategy in the section 5.4 which simulates the non-equilibrium condensation phenomenon has been verified its accuracy by comparing it with previous numerical researches. Following the Schnerr et al. [27]’s research which studied the humidity effects on the transonic flow field of a NACA0012 airfoil, the nucleation rate distribution and the pressure coefficient distribution have been calculated, and compared.

The mesh which has been constructed with ANSYS ICEM v. 17.0 shows a 2-dimensional half symmetric NACA0012 airfoil geometry as shown in Fig. 5.4. The chord length of airfoil is 0.1m and the calculation domain size is 20 X 10 chord length. At inlet location, pressure-far-field condition has been adopted with total pressure, total temperature, inlet Mach number, and vapor mass fraction. The inlet parameters are listed in Table 5.2. Calculation has been conducted with inviscid condition same as Schnerr et al., and the other solver setting methods are same as in the section 5.3.

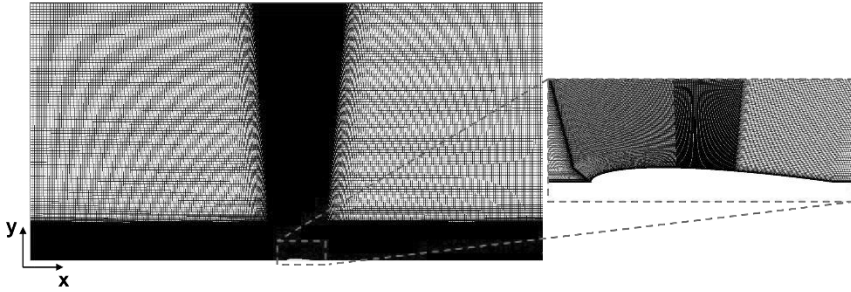


Figure 5. 4. Mesh geometry – NACA0012.

Table 5. 2. Inlet conditions

Variable	Value
Total pressure	100 kPa
Total temperature	293.15K
Inlet Mach number	0.8
Relative humidity	0, 50%

Figure 5.5 shows the nucleation rate distribution following the chord-wise location. The difference of maximum nucleation rate is lower than order of 1 and the difference of its location is lower than 0.025 chord length. Figure 5.6 shows the pressure coefficient distributions for 0 and 50% RH conditions. Y-axis represents minus C_p value and x-axis represents a chord wise location. For both RH conditions, pressure coefficient distributions follow Schnerr et al.'s results well including shock location, shock location shift, and the increase in C_p value upstream of the shock. In conclusion, author's numerical results show good agreements with previous researcher's results, therefore, author's calculation strategy is validated.

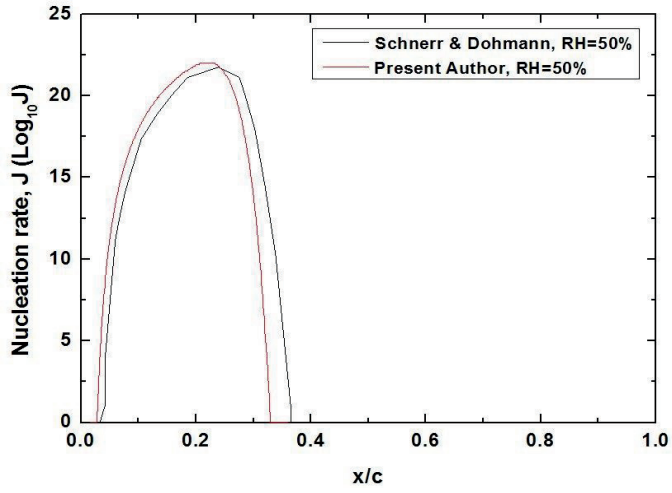


Figure 5. 5. Nucleation rate distribution at 50% RH condition.

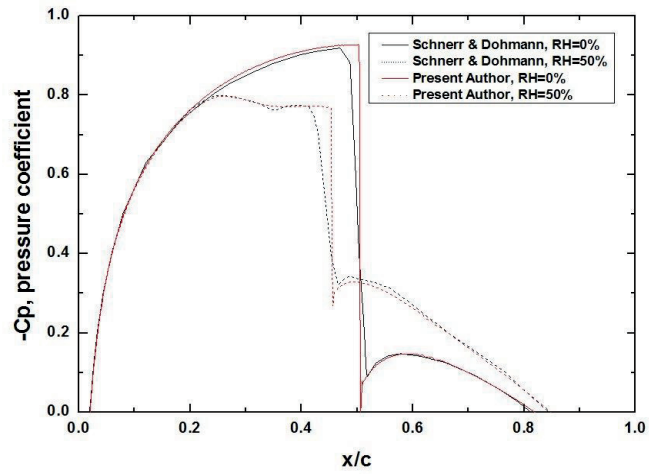


Figure 5. 6. Pressure coefficient distribution (RH= 0, 50%).

Chapter 6. Numerical Results

6.1 Introduction

This chapter covers the numerical results of the humidity effects on the transonic compressor cascade performance. From the experimental results in Chapter 4, the humidity effects on the aerodynamic performance of a transonic compressor cascade have been realized. However, due to the limitations in measurements, all the effects of humidity have been shown as the accumulated results of condensation. For example, in the main passage, although there are some contributions concerning the loss coefficient increase (ex. shock, heat addition from condensation, and mixing), each contribution cannot be distinguishable. Furthermore, it is necessary to confirm that the change in the cascade aerodynamic performance is caused by the humidity change (i.e. due to the condensation/evaporation phenomenon). Therefore, numerical calculation has been conducted to support the experimental results, and for the detailed analysis of the cascade flow field. This chapter is composed with as follows. First, the numerical results are validated by comparing with experimental results. Then, the humidity effects on the loading distribution, deviation, and loss coefficient are discussed by showing the detailed flow field contours.

6.2 Validation Results

Before discussing the humidity effects on the cascade flow fields, numerical results should be validated with experimental results. Since numerical results show monotonically increasing effects as relative humidity increases, two extreme relative humidity conditions (20, 53%) are compared with experimental results. For the validation, the pressure coefficient distribution, deviation, and loss coefficient distribution results are compared with experimental ones.

Figure 6.1 shows the loading distributions of CFD and EXP results. CFD results are plotted with lines and EXP results with symbols. In the 20% relative humidity condition, CFD result shows a good agreement with EXP result. However, in 53% relative humidity condition, CFD result overestimates the humidity effects on the suction surface. Thus, C_p values on the suction surface show higher values than experimental ones. On the other hand, the difference in the shock location and C_p values on the pressure surface are relatively low. In conclusion, although CFD results predict relatively large effects of humidity on the pressure coefficients of suction surface, CFD qualitatively well predicts the characteristics of humidity effects on the pressure coefficient distribution – 1) pressure coefficient increases on the suction surface upstream of the shock, 2) shock location shifts downstream, and 3) pressure coefficient decreases on the pressure surface.

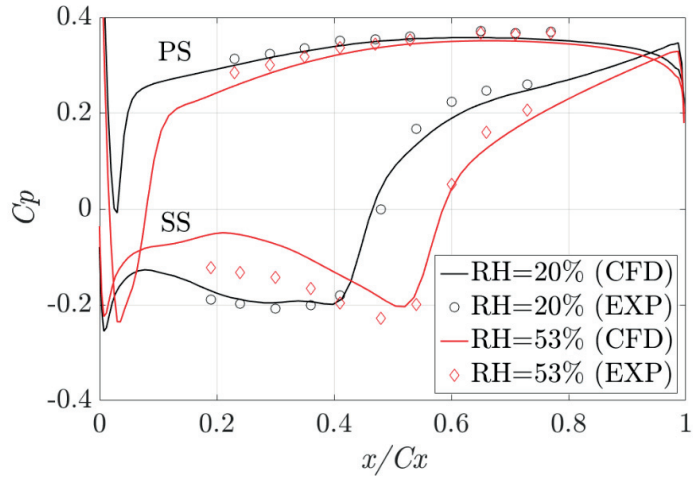


Figure 6. 1. CFD validation results - pressure coefficient distributions.

Figure 6.2 shows the deviation distributions of CFD and EXP results at $x/C_x=1.4$. Comparing to the EXP results, CFD results show relatively low peak and low intensity in the wake region (where, $y/S= 0.3, 0.4$) and relatively low values (about 2°) in the main passage region. However, as in the EXP results, CFD results show negligible effects of humidity on the deviation (the limitations of CFD predicting the exact deviation distribution are discussed in the Appendix I).

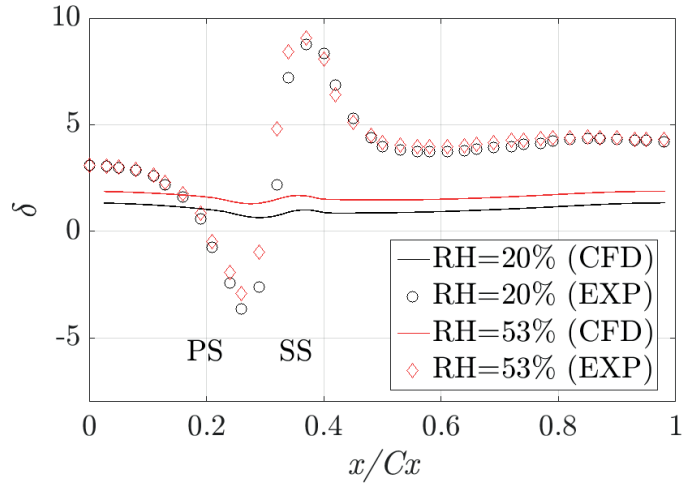


Figure 6. 2. CFD validation results - deviation distribution.

Figure 6.3 shows the loss coefficient distributions of CFD and EXP results at $x/Cx=1.4$. CFD results predict relatively low loss coefficient values compared to the EXP results (shifts in absolute value of 0.02, in percentage of 20%). However, the characteristics of the humidity effects on loss coefficient distribution shown in EXP results are also captured in the CFD results - 1) the increase of loss coefficient in the main passage as relative humidity increases, especially, noticeable changes near the suction surface, and 2) negligible changes on the wake region. Therefore, it can be concluded that except the shift in absolute value, CFD qualitatively well predicts the humidity effects on the loss coefficient distribution.

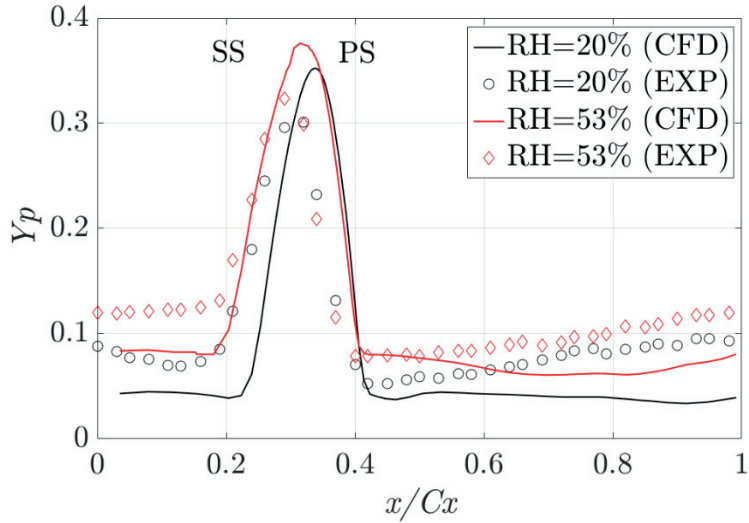


Figure 6. 3. CFD validation results - loss coefficient distribution.

In conclusion, although there are little differences in the absolute values, CFD qualitatively well captures the characteristics of humidity effects on the transonic compressor cascade performance. Thus, it can be concluded that the CFD results are validated, therefore, CFD results can be used as a tool for analyzing the experimental results.

6.3 Blade loading distribution

Figure 6.4 shows the CFD results of the pressure coefficient distributions for varying the relative humidity. First, negligible changes are shown between 20% and 32% relative humidity conditions. These negligible changes which are also shown in the experimental results, can be explained in terms of condensate mass fraction contour shown in Figure 6.5. For the 20% relative humidity condition, although supersaturation ($p_v/p_{v,eq}$) is higher than 10 upstream of the cascade, condensate mass fraction is negligible in the cascade passage because the calculated nucleation

rate from Eq. 2.9 is too low (order of 11) to trigger a condensation in the cascade passage. Hence, in 20% RH condition, the humidity effects can be neglected, thus, this condition is referred to as the baseline case. For 32% RH condition, condensation occurs in the cascade passage (Figure 6.5. (b)). However, due to the low condensate mass fraction ($< 30\%$) and condensation location near the trailing edge, condensation shows negligible effects on the pressure coefficient distribution. Therefore, there are negligible changes for 32% RH condition compared to the 20% RH condition. From the 42% relative humidity condition, humidity effects become noticeable. As the relative humidity increases, 1) pressure coefficient values on the suction surface upstream of the shock increase, 2) shock shifts to downstream, and 3) pressure coefficient values on the pressure surface decrease. All these effects can be explained from the condensation in the cascade passage as follows. First, from the 42% RH condition, condensation occurs upstream of the leading edge (i.e. condensate mass fraction starts to increase from the leading edge) and its onset location moves to upstream. Also, the larger amount of vapor condenses (i.e. condensate mass fraction increases) as relative humidity increases. When condensation occurs, latent heat is released from the vapor to the ambient flow. Following the Rayleigh flow theory (see Appendix F), when the heat is added to the supersonic flow, static pressure increases. Thus, C_p values upstream of the shock on the suction surface increase and these effects become strong as relative humidity increases (due to more condensation). In addition, the increase of pressure upstream of the shock pushes the shock downstream, thus, shock location shifts downstream as relative humidity increases. At the same time, condensation also affects shock strength decreasing the shock-front Mach number (shock strength is defined by the static pressure ratio

$p_{shock,2}/p_{shock,1}$ between upstream and downstream of the shock, and it is listed in Table 6.1). For 20% and 32% RH condition, it shows negligible changes which are consistent with the previous argument. From the 42% RH condition, shock strength monotonically decreases as relative humidity increases. Therefore, due to the decreased shock strength, the pressure coefficient values on the pressure decrease as relative humidity increases.

From the condensate mass fraction contour in Fig. 6.5, the other characteristic is also captured: droplet evaporation. Compressor cascade geometry is similar to the converging diverging nozzle. Therefore, from the leading edge to passage shock, flow is accelerated. Thus, condensation can occur as flow accelerates following the suction surface (when the temperature decreases below a dew point). On the other hand, downstream of the shock, temperature increases abruptly from the shock diffusion and the geometrical diffusion. Thus, the condensate mass fraction start to decrease downstream of the shock which represents the droplet evaporation. During the evaporation, heat is removed from the flow to the vapor. Again, following the Rayleigh flow, heat removal in the subsonic flow (the subsonic flow downstream of the shock) reduces the Mach number and increases the pressure. Thus, the evaporation phenomenon explains the negligible variation of shock strength between 49% and 53% RH conditions: larger amount of evaporation for 53% RH condition increases the downstream static pressure, $p_{shock,2}$, thus, negligible changes in shock strength, $p_{shock,2}/p_{shock,1}$. Furthermore, with the same logic, the negligible changes of the pressure coefficient values on the pressure side near trailing edge can be explained.

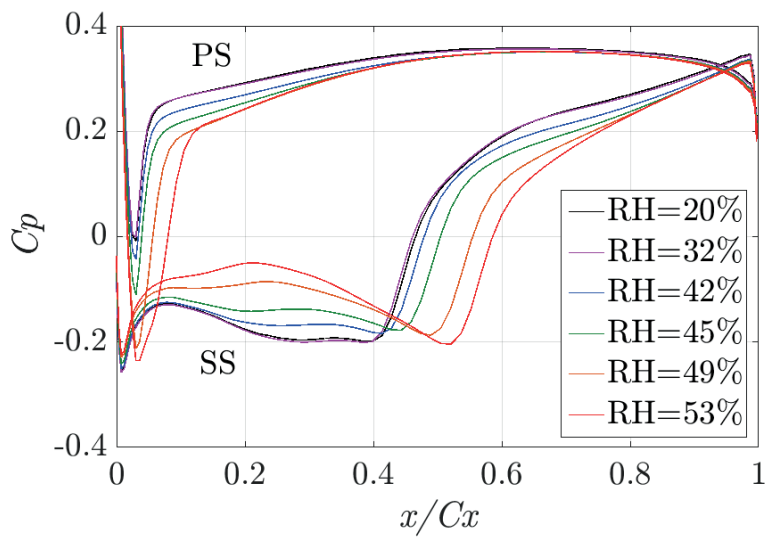
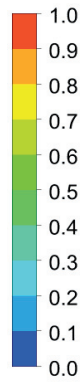
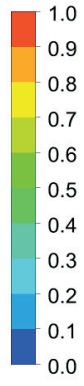


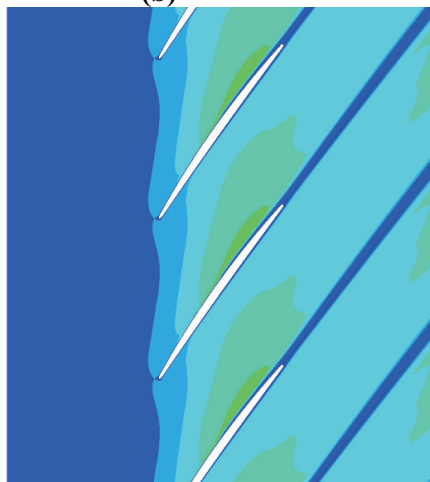
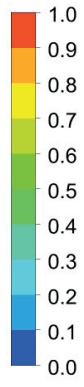
Figure 6. 4. CFD result – pressure coefficient distribution vs axial chord wise location.



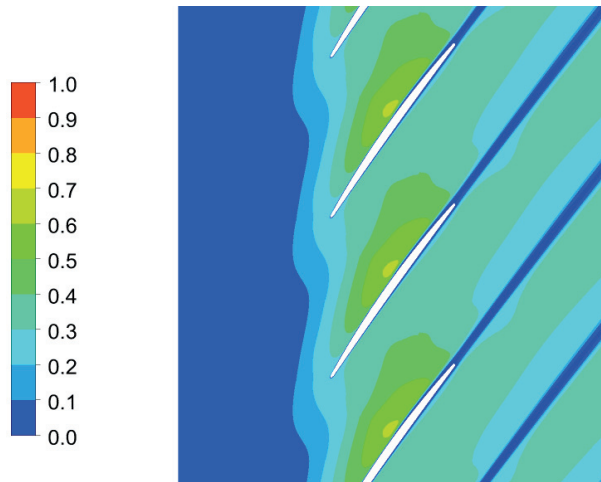
(a)



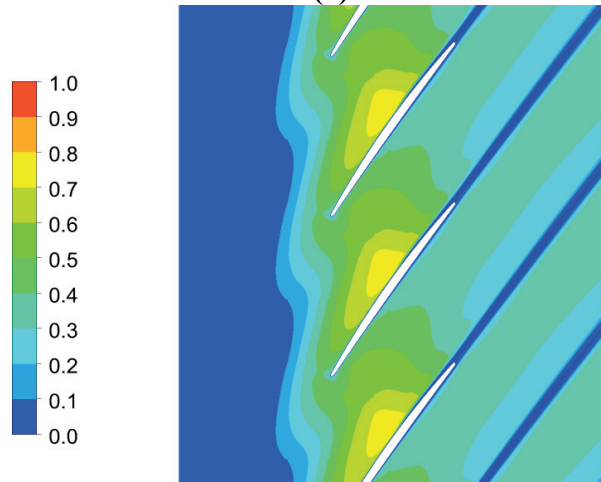
(b)



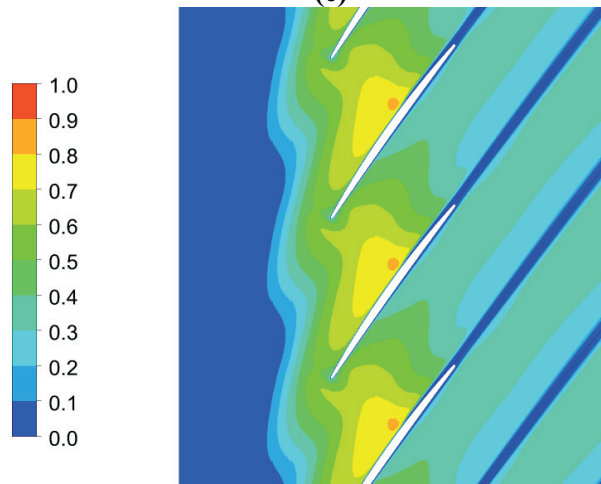
(c)



(d)



(e)



(f)

Figure 6. 5. CFD result – condensate mass fraction contour: (a) RH=20%, (b) RH=32%, (c) RH=42%, (d) RH=45%, (e) RH=49%, (f) RH = 53%.

Table 6. 1. Shock strength

RH (%)	Shock strength
20	1.54
32	1.54
42	1.50
45	1.46
49	1.45
53	1.45

6.4 Deviation

Figure 6.6 shows the CFD results of deviation distribution following a pitch-wise location at $x/C_x=1.4$ and the mass averaged values are listed in Table 6.2. Both results well capture the negligible effects of humidity on deviation as in the experimental results except the difference of the absolute value of 2° . The deviation is the parameter that how well the flow follows the blade geometry. Thus, it is directly affected by the boundary layer thickness on the blade, and in case of presence of the shock, shock-induced boundary layer separation is a major factor which affects the boundary layer thickness. Figure 6.7 shows the Mach number contours for various relative humidity conditions. Following the effects of condensation on the shock strength (i.e. reduced shock strength in Table 6.1), reduced shock-induced boundary layer separation can be expected. Thus, as relative humidity increases, deviation should be decreased. However, as shown in Mach number contours, the shock-induced boundary layer separation is negligible even in the baseline flow case (i.e. 20% RH condition). Thus, due to the absence of noticeable boundary layer separation in the baseline case, the reduction of the shock

strength due to condensation does not affect the boundary layer thickness and deviation thereby.

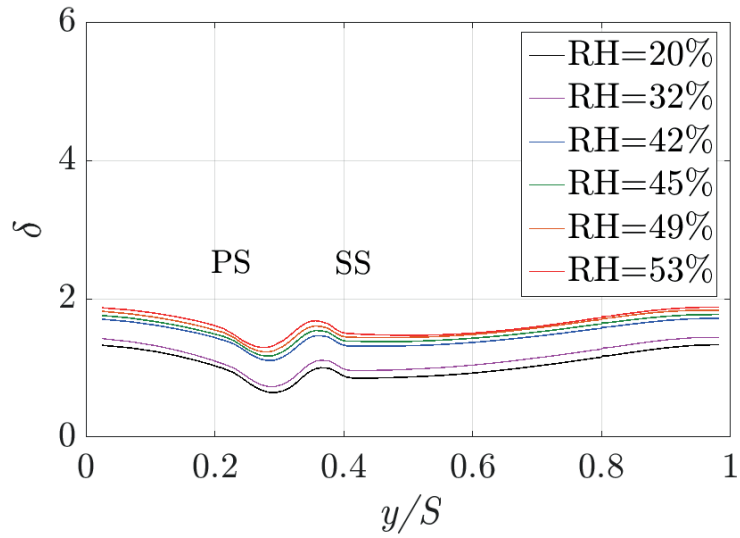
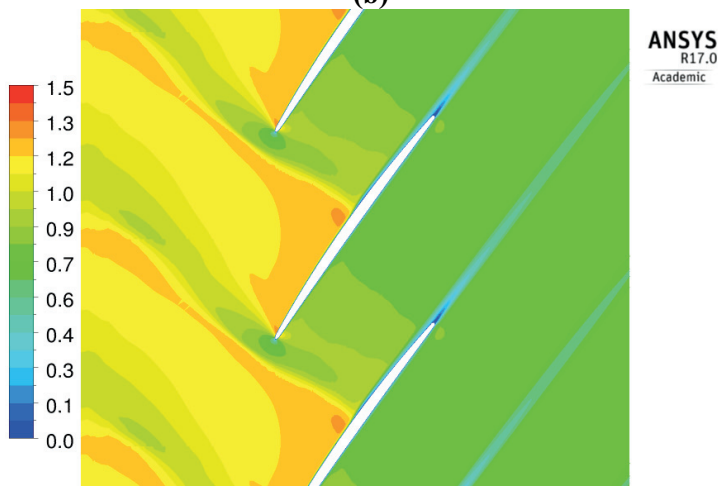
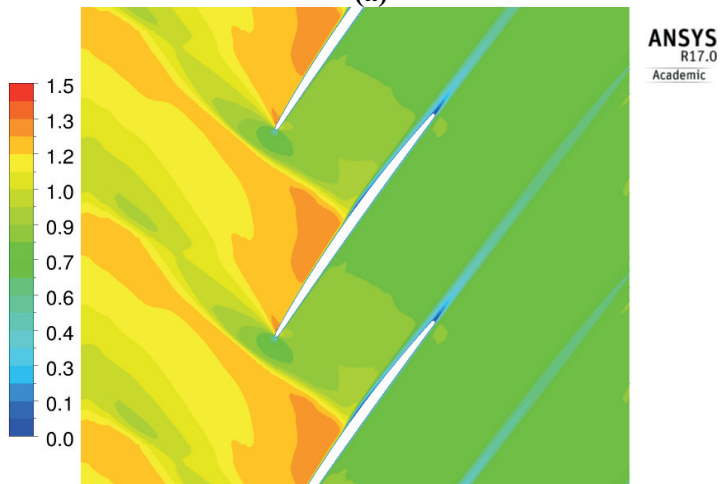
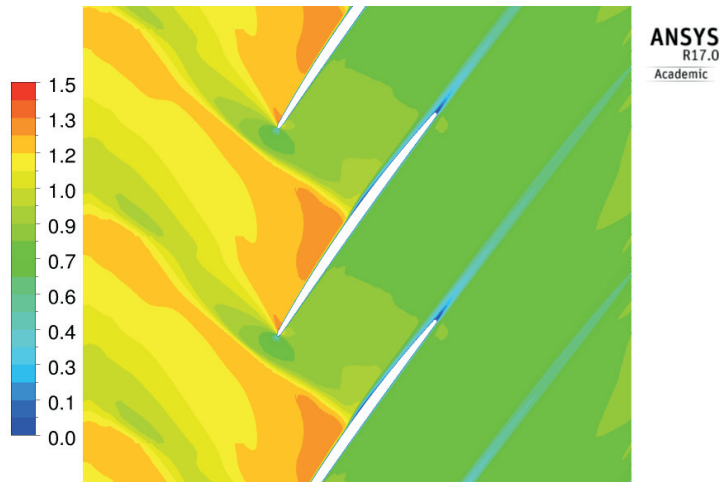


Figure 6. 6. CFD result – deviation distribution vs pitch-wise location

Table 6. 2. Mass averaged deviation

RH (%)	Mass averaged deviation
20	1.1
32	1.1
42	1.4
45	1.4
49	1.6
53	1.7



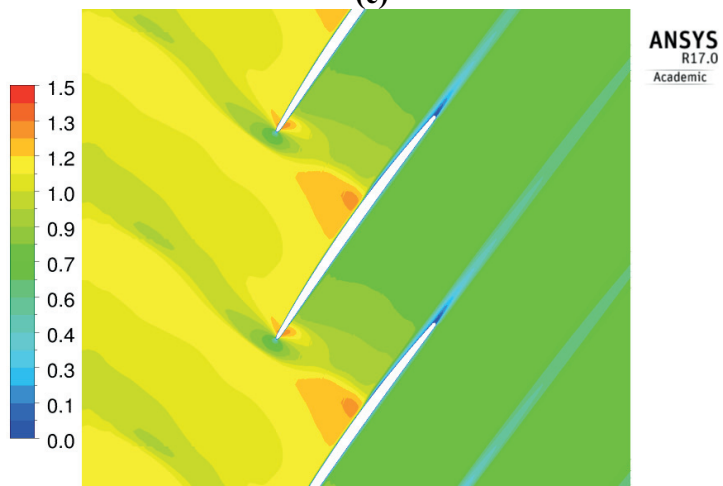
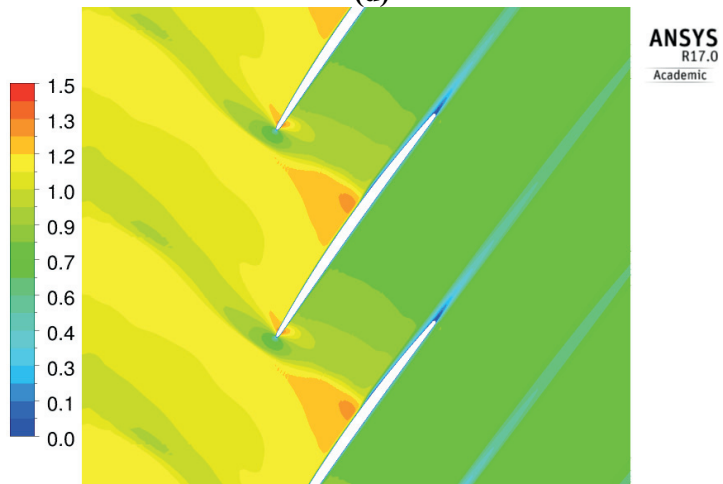
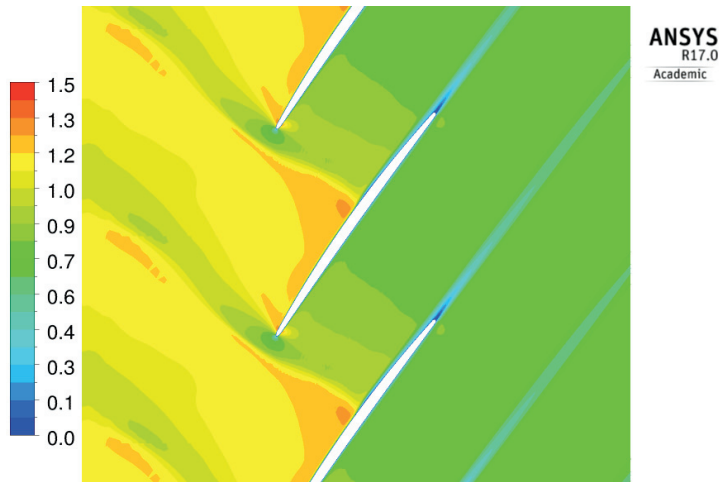


Figure 6. 7. CFD result – Mach number contour: (a) RH=20%, (b) RH=32%, (c) RH=42%, (d) RH=45%, (e) RH=49%, (f) RH = 53%.

6.5 Loss coefficient

6.5.1. Humidity effects on the loss coefficient distribution

Figure 6.8 shows the CFD results of loss coefficient distribution following a pitch-wise location at $x/Cx=1.4$ and the mass averaged values are listed in Table 6.3. Except the shift in absolute value about 0.02, the CFD results qualitatively well predict the characteristics of humidity effects on the loss coefficient distribution shown in the experimental results – 1) changes in the wake loss are negligible; 2) loss coefficient in the main passage increases as relative humidity increases, especially near the suction surface ($y/S= 0 \sim 0.3$); and 3) mass-averaged loss coefficient increases as relative humidity increases.

First, as argued in the previous section (in the section of 6.4), humidity (i.e. the condensation effect) has negligible effects on the boundary layer thickness. Thus, there are negligible changes in the wake region for all humidity conditions. However, in the main passage, as the relative humidity increases from 42% RH condition, the loss coefficient increases, especially, noticeable changes are shown near the suction surface ($y/S= 0 \sim 0.3$) where the condensation occurs intensively. In the Chapter 4, it is argued that the increase in loss coefficient is mainly due to the condensation which decreases the total pressure by a heat addition. Figure 6.9 supports that argue by showing the cascade entropy contours (reference condition is inlet condition) for various relative humidity conditions. For 20% RH condition, entropy in the main passage increases mainly from the passage shock. However, for 32% RH condition, another entropy increase is shown near the trailing edge where the condensate mass fraction increases in Fig. 6.5. For the higher relative humidity conditions, the entropy

increases from the upstream of leading edge where condensate mass fraction increases and the amount of entropy increase increases as relative humidity increases. Thus, it can be concluded that the loss increase in main passage shown in the experimental results is mainly come from the condensation effects.

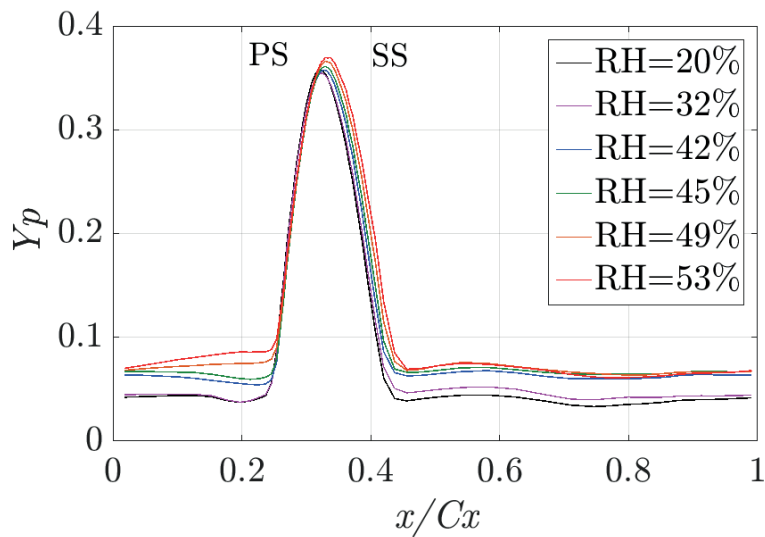
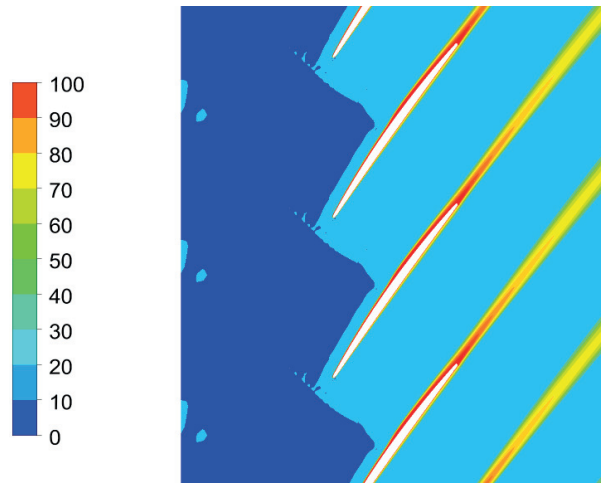


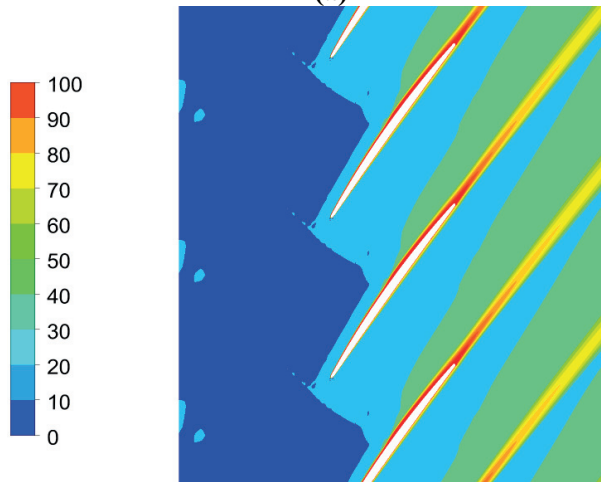
Figure 6. 8. CFD result – loss coefficient distribution vs pitch-wise location.

Table 6. 3. Mass-averaged loss coefficient

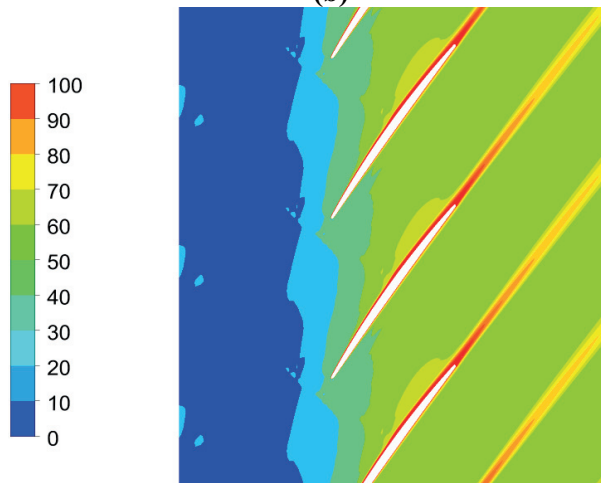
<i>RH</i> (%)	Mass averaged loss coefficient
20	0.0693
32	0.0738
42	0.0833
45	0.0882
49	0.0952
53	0.1024



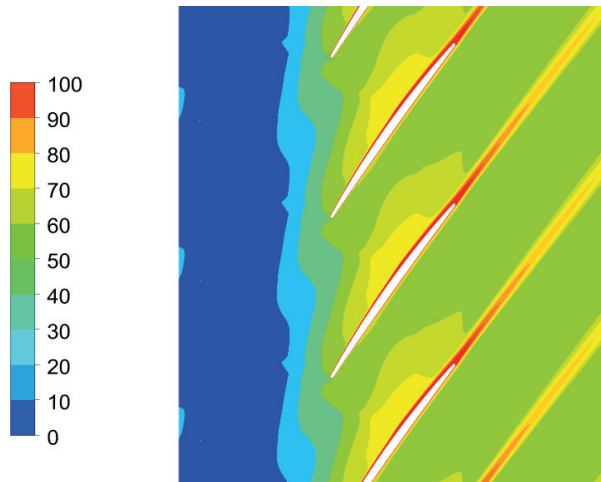
(a)



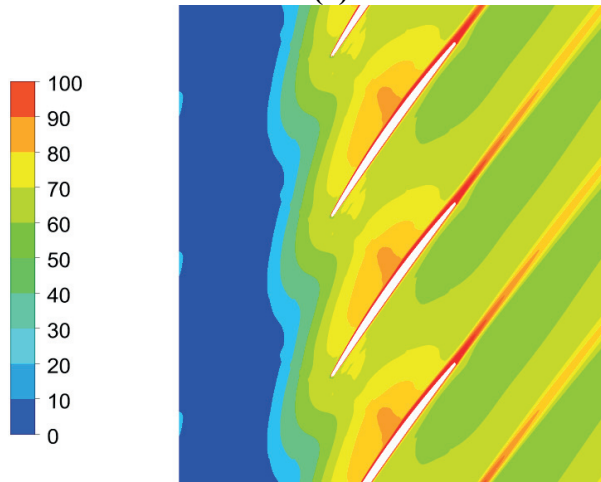
(b)



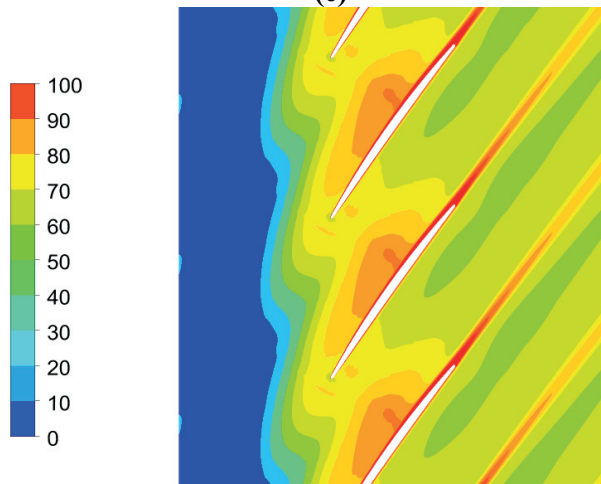
(c)



(d)



(e)



(f)

Figure 6. 9. CFD result – entropy contours: (a) RH= 20%, (b) RH= 32%, (c) RH= 42%, (d) RH= 45%, (e) RH= 49%, (f) RH= 53%.

6.5.2. Main passage loss contribution

The factors concerning the loss coefficient increase in the main passage are shock, heat addition from condensation, and mixing. In this section, main passage loss is decomposed with each factors and see the changes of each composition.

To distinguish the contributions of shock loss, condensation loss, and mixing loss in the main passage, the loss coefficient evolutions following a streamline are shown in Fig. 6.10. For 20% RH condition, the loss coefficient abruptly increases due to the two shocks - a bow shock (upstream of LE, at $x/Cx = -0.15$) and a passage shock (at $x/Cx = 0.4$). In the other region, the loss coefficient increase is negligible. For 32% RH condition, there are negligible changes on the loss coefficient evolution from $x/Cx = -0.5$ to 0.5 location comparing to the 20% RH condition. However, loss coefficient slightly start to increase at $x/Cx = 0.5$ due to the condensation near the trailing edge. From the 42% RH condition, the loss coefficient continuously increases from the upstream of leading edge and its onset location moves to upstream as relative humidity increases (loss coefficient start to increase at $x/Cx = -0.1$ for RH 42% condition, and $x/Cx = -0.5$ for RH 53% condition). The main reason of the continuous loss coefficient increase can be found in the condensate mass fraction contour of Fig. 6.5. As relative humidity increases, the condensation onset location moves to upstream and a larger amount of vapor is condensed. Thus, due to the heat addition from condensation, loss coefficient increases. On the other hand, downstream of the passage shock, loss coefficient start to decrease due to the evaporation caused by the temperature increase from the shock diffusion and geometrical diffusion and, downstream of trailing edge, it keeps constant values because the geometrical diffusion ends and no more evaporation occurs. Therefore,

the main passage loss composition can be distinguishable. The shock loss can be estimated by adding the amount of loss increase from the bow shock and passage shock. However, the condensation loss and mixing loss cannot be distinguishable because these occurs continuously following a streamline contrary to the shock. Through the comparison of loss coefficient evolutions at 20 and 53% RH conditions, it can be only expected that condensation loss will be the major. Therefore, the main passage loss is decomposed with the shock loss and C-M loss (C-M loss describes the sum of condensation, mixing and all other losses which cause loss increase). The C-M loss can be estimated by subtracting the amount of loss increase due to the two shocks (bow shock and passage shock) from the loss coefficient value at $x/Cx = 1.4$. The estimated C-M loss increases monotonically from 0 to 0.065 as relative humidity increases from 20 to 53%. On the other hand, the shock loss decreases from 0.0172 to 0.0068 as the relative humidity increases from 20 to 53%. Contributions of each loss are listed in Table 6.4. The contribution of other losses continuously increases and, in 53% RH condition, C-M loss contributes about 80% of total loss.

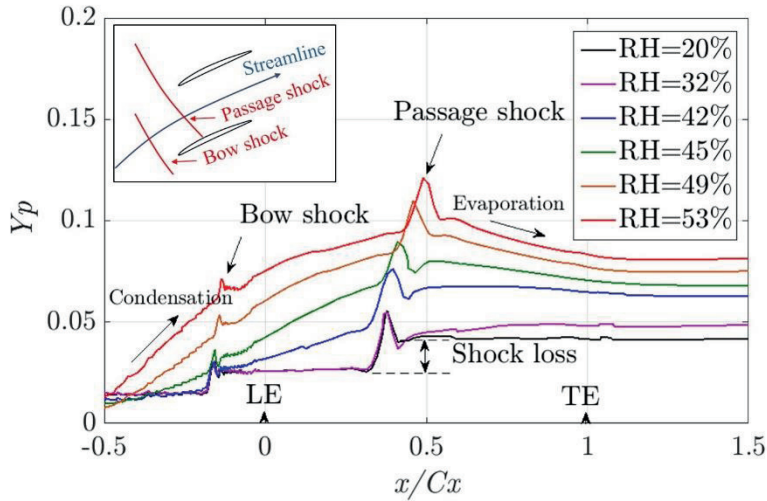


Figure 6. 10. CFD result – loss coefficient evolution following a streamline.

Table 6. 4. CFD results - Contribution of each loss in percentage.

<i>RH</i> (%)	Shock loss (%)	C-M loss (%)
20	100	0
32	79	21
42	60	40
45	37	63
49	25	75
53	21	79

6.5.3. Cascade loss composition

In this section, along with the section 4.5.2, by adopting the main passage loss contribution in Table 6.4, cascade loss is decomposed with profile loss, shock loss and C-M loss. Figure 6.11 shows the cascade loss composition change for various humidity conditions. As relative humidity increases, contribution of shock loss decreases from 46 to 11% of total loss, however, other losses increases from 0 to 41%. Also, because C-M loss increases at a faster rate than that at which shock loss decreases, total loss coefficient increases as relative humidity increases. Therefore,

contrary to the Geist et al [32]'s, when it reflects the C-M loss, loss coefficient increases as relative humidity increases.

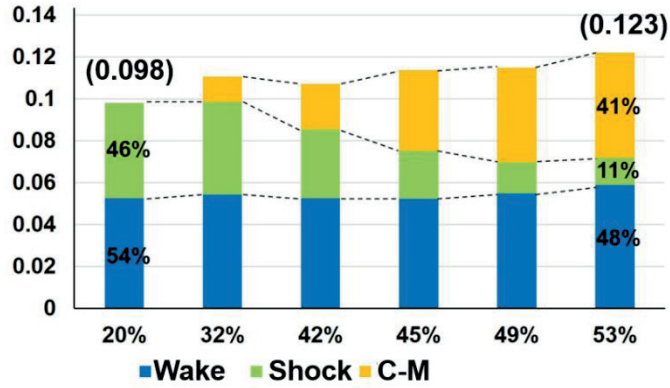


Figure 6. 11. Cascade loss composition.

Chapter 7. Conclusions

7.1 Summary

The humidity effects on the performance of a transonic compressor cascade have been investigated experimentally and numerically for the first time.

A new transonic cascade wind tunnel has been designed and built for the experiments. For the validation of the performance of a newly built transonic wind tunnel, flow symmetry about nozzle centerline and flow uniformity in the test section have been validated.

Experiments have been conducted for six different relative humidity conditions (20, 32, 42, 45, 49, 53%) at inlet Mach number 1.1, and incidence of $+5^\circ$. The humidity effects on the aerodynamic performance of a transonic compressor cascade have been investigated by measuring pressure coefficient distribution on the blade, deviation distribution, and loss coefficient distribution.

A numerical calculation has been conducted by adopting the Classical Nucleation Theory (CNT) and Hertz-Knudsen droplet growth rate model to simulate the non-equilibrium condensation phenomenon. The numerical calculation results have been validated with experimental results, and then, the CFD results have been used for the detailed analysis of the humidity effects on the transonic compressor cascade flow field.

The followings are the main conclusions of this study.

- 1) As the relative humidity increases, condensation occurs in the compressor

cascade passage (from the leading edge to the passage shock).

- 2) Condensation induces the static pressure increase upstream of the shock by releasing the latent heat to the flow. Thus, the pressure coefficient values on the suction surface increase, shock shifts downstream, and the pressure coefficient values on the pressure surface decrease.
- 3) Humidity has negligible effects on deviation in case of the baseline flow shows negligible shock-induced boundary layer separation.
- 4) The cascade loss composition has been described. Humidity has negligible effects on the wake loss. However, in the main passage, loss coefficient increases as relative humidity increases. In the main passage, there are competing effects between the shock loss and condensation-induced loss. As relative humidity increases, shock loss decreases because condensation decreases the shock strength, however, condensation-induced loss increases because the release of latent heat decreases total pressure. However, since the rate of the condensation-induced loss increase is faster than that of shock loss decrease, the loss coefficient increases as relative humidity increases.

7.2 Recommendations

This study is the first step for investigating the humidity effects on the aerodynamic performance of a transonic compressor cascade. In this study, humidity effects at a single inlet Mach number and a single incidence condition have been investigated. Thus, in order to expand the scope of this research, the following

researches are recommended.

- 1) The study about the humidity effects at various inlet conditions – various inlet Mach numbers and incidence angles.
- 2) The study about the humidity effects on the real transonic compressor. In the real compressor flow field, lots of 3-dimensional flow features are exist, such as hub corner separation and tip clearance flow. Especially, the blade loading change due to the condensation can change the compressor performance much by affecting the characteristics of tip clearance flow.
- 3) The study about the humidity effects on the compressor stage mismatch. A compressor is a set of a rotor and a stator, thus, the outgoing flow from the rotor is the incoming flow in the respect of a stator. Therefore, when the condensation on the rotor disturbs outgoing flow, the performance of a stator can be changed.

References

- [1] Chaker, M. and Meher-Homji, C. B., 2011, Gas turbine power augmentation: parametric study relating to fog droplet size and its influence on evaporative efficiency, *J. Eng. Gas Turbines Power* 133 pp. 1316–1326.
- [2] Zheng, Q., Sun, Y. F., Li, S. Y., and Wang, Y. H., 2003, Thermodynamic analyses on wet compression process in the compressor of gas turbine, *J. Turboma.* 125 pp. 489–496.
- [3] Jonsson, M. and Yan, J., 2005, Humidified gas turbines—a review of proposed and implemented cycles, *Energy* 30 pp. 1013–1078.
- [4] Rahim, M. A., 2012, Performance and sensitivity analysis of a combined cycle gas turbine power plant by various inlet air-cooling systems, *P. I. Mech. Eng. A-Journal of Pow.* 226 pp. 922–931.
- [5] Alhazmy, M. M. and Najjar, Y. S. H., 2004, Augmentation of gas turbine performance using air coolers, *Appl. Therm. Eng.* 24 pp. 415–429.
- [6] Garetta, R., Romeo, L. M., and Gil, A., 2004, Methodology for the economic evaluation of gas turbine air cooling systems in combined cycle applications, *Energy* 29 pp.1805–1818.
- [7] Al-Ibrahim, A. M. and Varnham, A., 2010, A review of inlet air-cooling technologies for enhancing the performance of combustion turbines in Saudi Arabia, *Appl. Therm. Eng.* 30 pp. 1879–1888.
- [8] Bhargava, R. K., Meher-Homji, C. B., and Chaker, M., 2005, Gas turbine fogging technology: a state-of-the-art review—Part I: Inlet evaporative fogging-analytical and experimental aspects, *J. Eng. Gas Turb. Power* 129 pp. 71–82.
- [9] Chaker, M. 2005, Key parameters for the performance of impaction pin nozzles

used in inlet fogging of gas turbine engines, *J. Eng. Gas Turb. Power* 129 pp. 473–477.

[10] White, A. J. and Meacock, A. J., 2004, An evaluation of the effects of water injection on compressor performance, *J. Eng. Gas Turb. Power* 126 pp. 728–736.

[11] Roumeliotis, I. and Mathioudakis, K. 2006, Water injection effects on compressor stage operation, *J. Eng. Gas Turb. Power* 129 pp. 453–461.

[12] Kerrebrock, J. L., 1981, Flow in Transonic Compressors, *AIAA Journal* 19(1), pp. 4-19

[13] Gostelow J. P. 1984, *Cascade aerodynamics*, Pergamon Press.

[14] Samuels, J.C. and Gale B.M., 1950, Effects of humidity on performance of turbojet engines, National Advisory Committee for Aeronautics, Washington, D.C., Technical note 2119.

[15] Fishbeyn B.D. and Pervyshin N.V., 1970, Determination of the effects of atmospheric humidity on the characteristics of a turbofan engine, Translation by foreign technology division, Wright-Patterson AFB, OH, FTD-HT-23,290-68 (AD 715232).

[16] Spencer, J. H., and Archer D. C., 1971, The effect of condensation within an aircraft inlet duct on installed turbofan engine performance, Proceedings of the Tenth National Conference on Environmental Effects on Aircraft and Propulsion systems, Philadelphia.

[17] Blake, J.C., 1975, Effects of condensation in the JT9D turbofan engine bellmouth inlet, AIAA Paper No. 75-1325, AIAA/SAE 11th Propulsion Conference, Anaheim, California.

[18] Bird, J. and Grabe, W., 1991, Humidity effects on gas turbine performance,

International Gas turbine and Aeroengine congress and exposition, ASME, 91-GT-329.

[19] AGARD advisory report, Recommended practices for the assessment of the effects of atmospheric water ingestion on the performance and operability of gas turbine engines, AGARD advisory report No. 332.

[20] Oswatitsch, 1941, Die Nebelbildung in Windkanlen und ihr Einflub auf Modellversuche. Jahrbuch d. Deutschen Lnftfahrtforschung I, pp. 692—703.

[21] Wegner, P.P., 1975, Nonequilibrium flow with condensation, *Acta Mechanica* 21, pp. 65-91.

[22] Schnerr, H.G., and Dohrmann, U. 1988, Theoretical experimental investigation of 2-D diabatic transonic and supersonic flow fields, IUTAM Symposium Gottingen 24.

[23] Frank, W. 1985, Condensation phenomena in supersonic nozzles, *Acta Mechanica* 54, pp. 135-156.

[24] Lamanna, G., 2000, On nucleation and droplet growth in condensing nozzle flows. PhD thesis, Eindhoven University of Technology.

[25] Huang J.C. and Gault, R.I., 2008, Effect of humidity on transonic flow, *Journal of aircraft* 45 (6).

[26] Schnerr, G.H. and Dohrmann, U. 1990, Transonic flow around airfoils with relaxation and energy supply by homogeneous condensation, *AIAA journal* 28 (7)

[27] Schnerr, G.H. and Dohrmann, U. 1994, Drag and lift in nonadiabatic transonic flow, *AIAA journal* 52 (1).

[28] Yashiro, S., Satoru, Y. 2003. Numerical prediction of humid effect to transonic flows in turbomachinery, international gas turbine congress

- [29] Sun, X., Li, L., and Li, Guojun, 2014, Transonic moist air flows with release of latent heat by non-equilibrium condensation, Proc. IMechE Part G: Journal of Aerospace engineering 228 (7) pp. 1083-1094.
- [30] Yamamoto, S. Moriguchi, S. Miyazawa, H. Furusawa, T., 2018, Effect of inlet wetness on transonic wet-steam and moist air flows in turbomachinery, International journal of heat and mass transfer 199 pp. 720-732.
- [31] Schreiber, H. A., and Starken, H. 1984, Experimental cascade analysis of a transonic compressor rotor blade section, Journal of engineer for gas turbines power 106(2) pp. 288-294.
- [32] Geist, S., Neupert, N., and Joos, F., 2017, Measuring the effect of moist droplet-laden flow on transonic compressor cascade performance, ISROMAC
- [33] Heiler, M., Winkler, G., and Schnerr, G. H., 2000, Homogeneous/heterogeneous condensation in transonic nozzle flows, ZAMM Vol.80.
- [34] Luijten, C.C.M., 1998, Nucleation and droplet growth at high pressure, PhD thesis, Eindhoven university of Technology.
- [35] Volmer, M., 1939, Kinetic de phasenbildung. Dresden: Steinkopff-Verlag
- [36] Becker, R. and Döring, W., 1935 Kinetische ehandlung derKeimbildung in übersattingten damfen. Annln derPhysik, 24, pp. 719–752.
- [37] Lamanna, G., 2000, On nucleation and droplet growth in condensing nozzle flows. PhD thesis, Eindhoven University of Technology.
- [38] Wölk, J. and Strey, R., 2001, Homogeneous nucleation of H₂O and D₂O in comparison: The isotope effect, J. Physical Chemistry B 105 (47) pp. 11683-11701.
- [39] Abraham, F. 1974, Homogeneous nucleation theory, Academic press.
- [40] Gyarmathy, G., 1982, The spherical droplet in gaseous carrier streams: review

and synthesis, *J. Multiphase science and Technology* 99-279,.

[41] Young, J. B., 1993, The condensation and evaporation of liquid droplets at arbitrary Knudsen number in the presence of an inert gas, *J. Heat Mass Transfer* 36 (11) pp. 2941-2956.

[42] Hertz, H., 1882, Ueber die Verdunstung der Flüssigkeiten, insbesondere des Quecksilbers, im luftleeren Raume, *Annalen der Physik* 253 (10) pp. 177-193.

[43] Knudsen, M., 1915, Die maximale Verdampfungsgeschwindigkeit des Quecksilbers, *Annalen der Physik* 352 (13) pp. 697-708.

[44] Peeters, P., Luijten, C.C.M., and Dongen, M.E.H. van, 2001, Transitional droplet growth and diffusion coefficients, *International Journal of Heat and Mass Transfer* 44, pp. 181-193.

[45] Young, J. B., and Guha, A., 1991, Normal shock-wave structure in two-phase vapour droplet flows, *Journal of Fluid Mechanics* 228 pp. 243-274.

[46] Marble, F. E., 1960, Some gasdynamic problems in the flow of condensing vapors, *Astronautica Acta* 14, pp. 104-111.

[47] Put. F., 2000, Numerical simulation of condensation in transonic flows. PhD thesis, University of Twente.

[48] Hill, P. G., 1966, Condensation of water vapour during supersonic expansion in nozzles, *Journal of Fluid Mechanics* 25 (3) pp.593-620.

[49] Prast, B., Numerical modelling of condensation processes in Laval nozzle flows, PhD thesis, Eindhoven university of Technology.

[50] Hacker, P. T., Experimental values of the surface tension of supercooled water, Technical Note 2510, National Advisory Committee for Aeronautics.

[51] Handbook of Chemistry and Physics, 72nd ed.; CRC Press: Boston, 1991-1992.

- [52] Pruppacher, H.R., and Klett, J.D., 1980, *Microphysics of Clouds and Precipitation*, D. Reidel Publishing Company.
- [53] Sonntag, D. and Heinz, D., *Sättigungsdampfdruck- und Sättigungsdampfdichte tafeln für Wasser und Eis*, VEB Deutscher Verlag für Grundstoffindustrie (1982).
- [54] Tweedt, D.L., Schreiber, H. A., and Starke, H., 1988, Experimental investigation of performance of a supersonic compressor cascade, NASA Technical Memorandum 100879.
- [55] AGARDograph 328, 1993, Advanced methods for cascade testing, AGARD-AG-328.
- [56] Kusters, B., and Schreiber, H. A., 1998, Compressor cascade flow with strong shock-wave/boundary-layer interaction, *AIAA Journal* 36 (11).
- [57] Harloff, G. J. and Smith, G. E., 1996, supersonic inlet boundary layer bleed flow, *AIAA Journal* 34 (4).
- [58] Grunnet, J. L., 1984, Transonic wind tunnel wall interference minimization, *Journal of Aircraft* 21 (9).
- [59] Steinert, W., Fuchs, R., and Starke, H., 1991, Inlet flow angle determination of transonic compressor cascades, *Journal of Turbomachinery* 144(3).
- [60] Coleman, H. W., and Steele, W. G., 1989, *Experimentation and Uncertainty analysis for engineers*, John Wiley & Sons.
- [61] Taylor, J. R., 1982, *An introduction error analysis – the study of uncertainties in physical measurements*, University science books.
- [62] Schnerr, G. H., 1988, 2-D transonic flow with energy supply by homogeneous condensation: Onset condition and 2-D structure of steady Laval nozzle flow. *J. Experiments in Fluids* 7 (3) pp. 145-156.

[63] Schnerr, G. H., 2005, Unsteadiness in condensing flow: dynamics of internal flows with phase transition and application to turbomachinery. Proceedings of the Institution of Mechanical Engineers, Part C: J. Mechanical Engineering Science 219 (12) pp. 1369–1410.

[64] Št'astný, M. and Šejna, M., 2015, Thermodynamic losses of hetero and homogeneous condensation in steam turbine cascades, Proceedings of the Institution of Mechanical Engineers, Part A: J. Power and Energy 229 (1) pp. 33-43.

Appendix A. Test Facility

A.1. Transonic wind tunnel

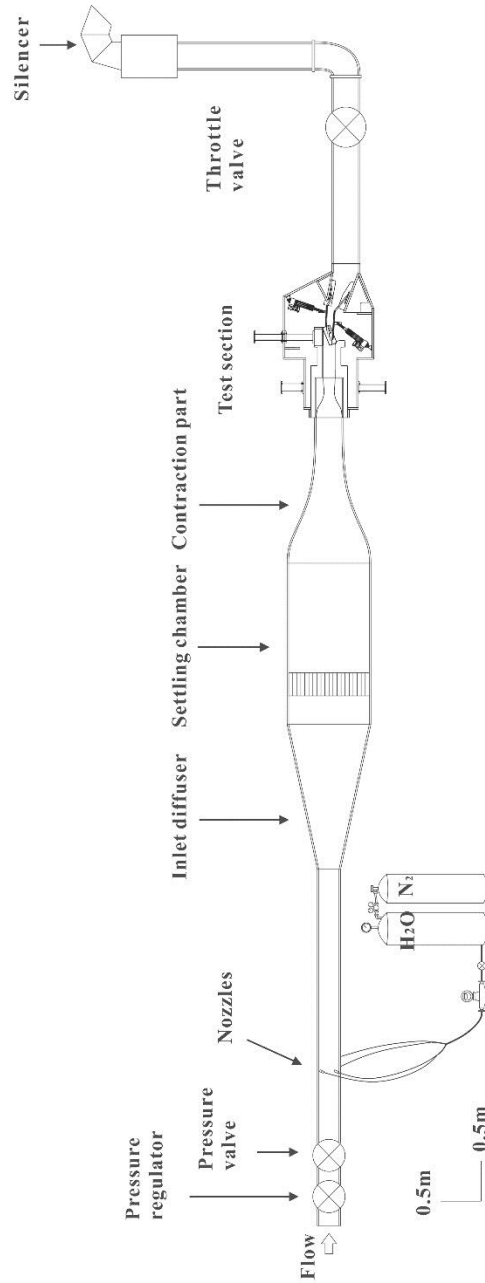


Figure A. 1. Schematic of transonic wind tunnel.



Figure A. 2. Pressure regulator.



Figure A. 3. Pressure valve.



Figure A. 4. Inlet duct.



Figure A. 5. Water nozzles.

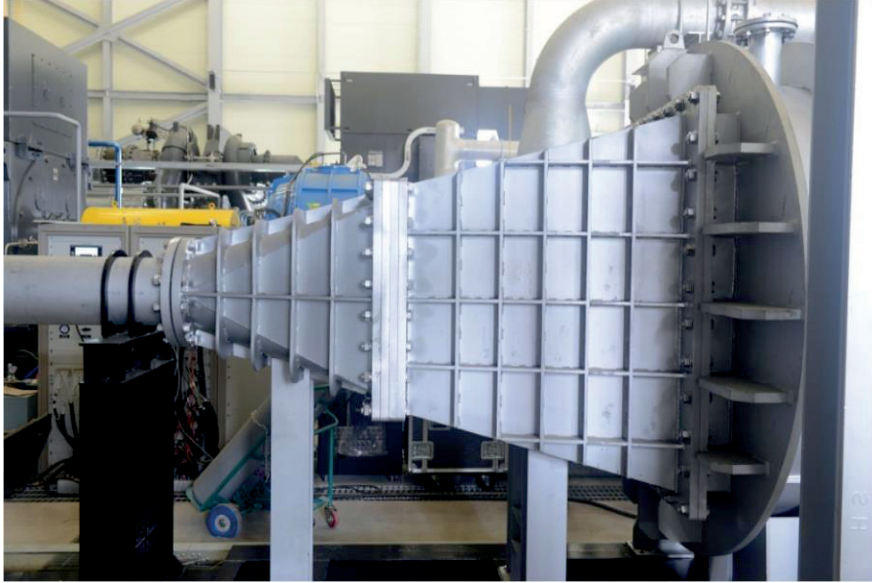


Figure A. 6. Inlet diffuser.



Figure A. 7. Settling chamber,

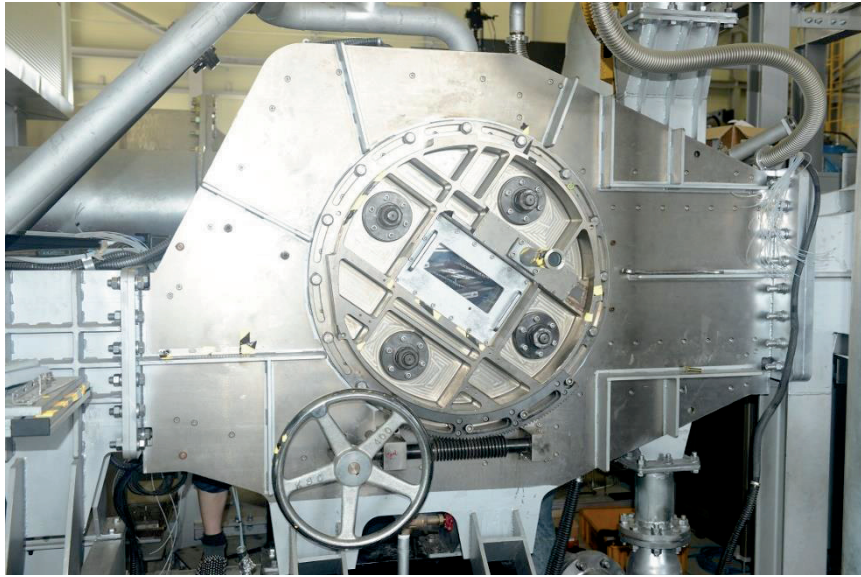


Figure A. 8. Test section,



Figure A. 9. Throttle valve,



Figure A. 10. Silencer.

A.2. Test section

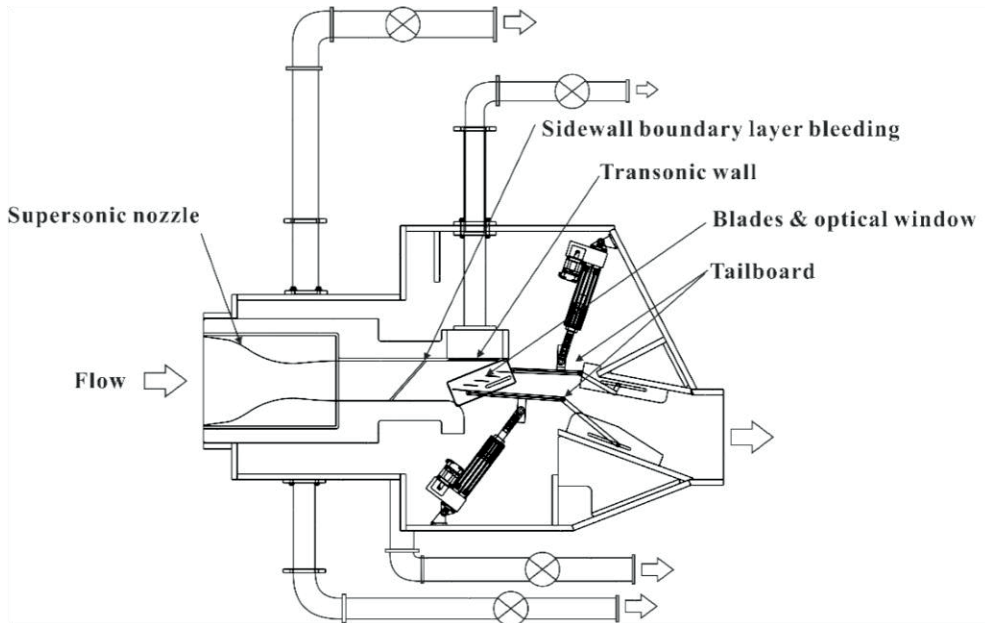


Figure A. 11. Schematic of test section.

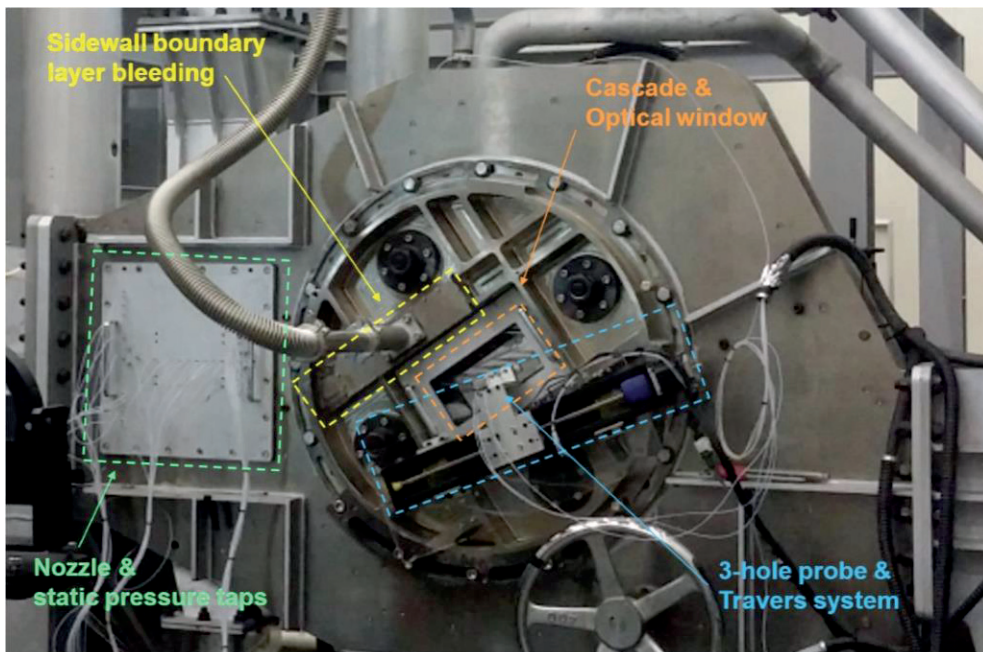


Figure A. 12. Test section.

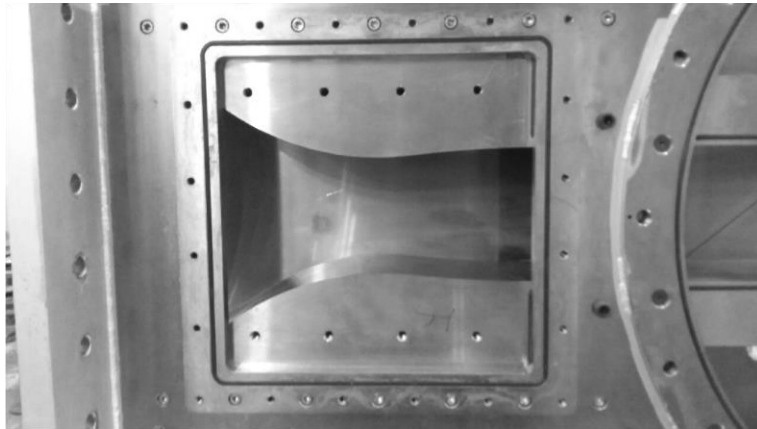


Figure A. 13. Supersonic nozzle.

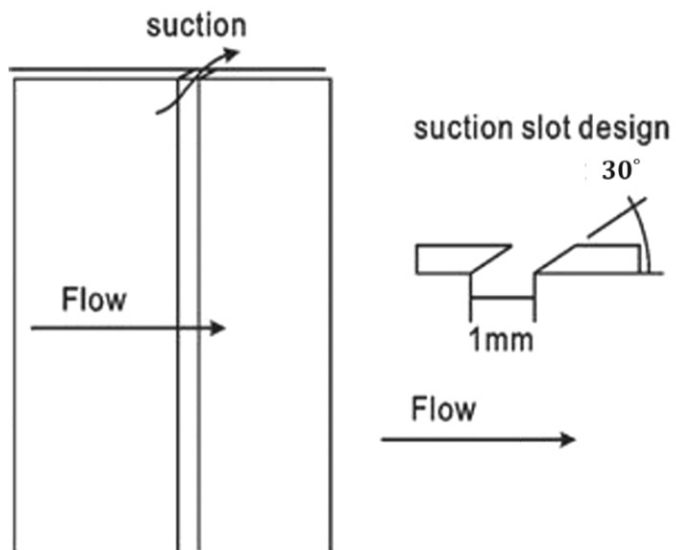


Figure A. 14. Schematic of sidewall boundary layer bleeding slot

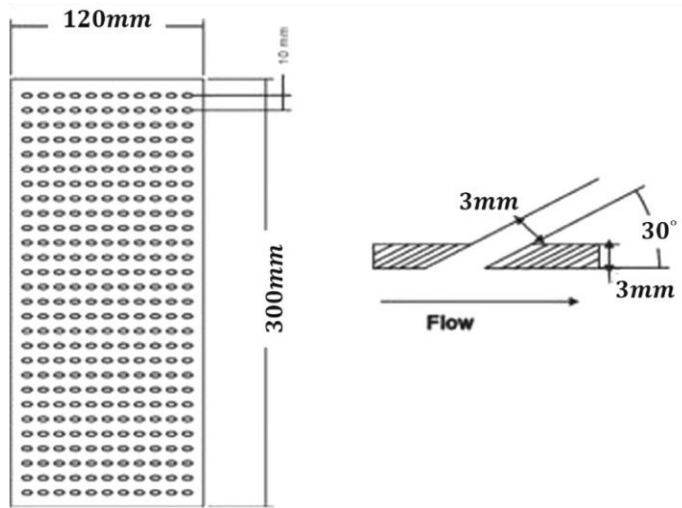


Figure A. 15. Schematic of transonic wall

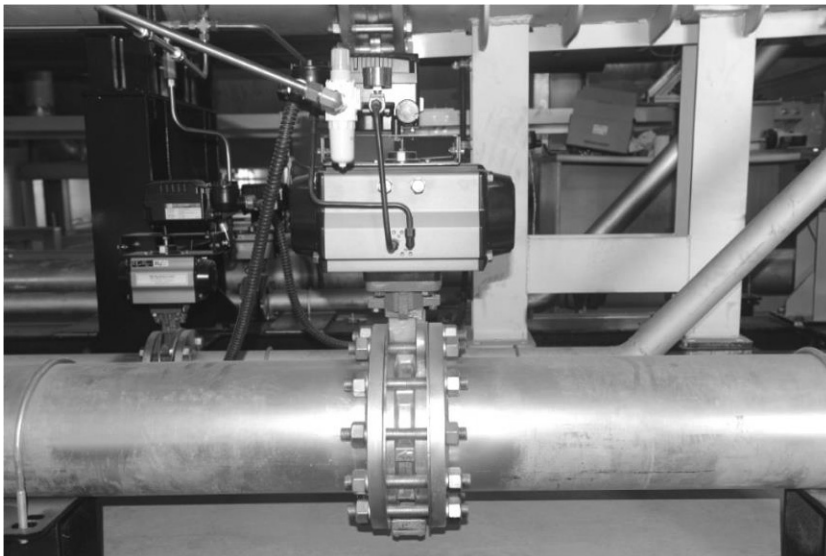


Figure A. 16. Lower bypass flow valve.

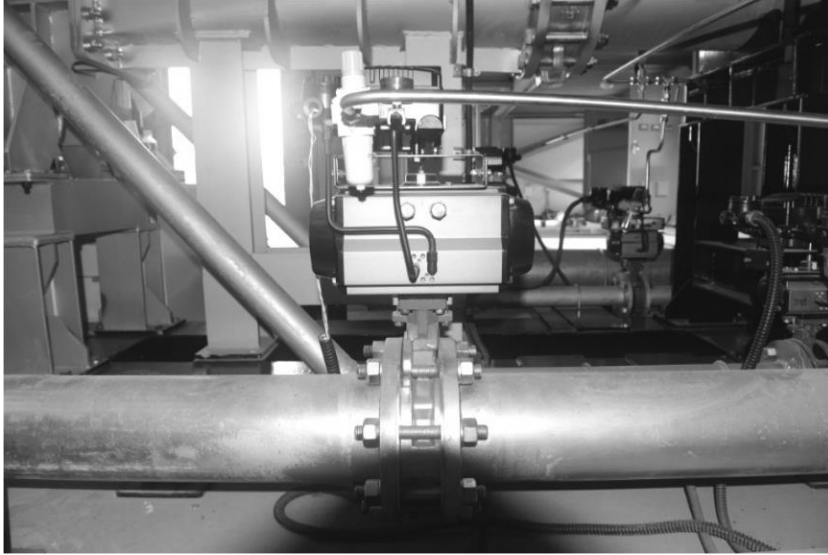


Figure A. 17. Upper bypass flow valve.



Figure A. 18. Sidewall boundary layer bleeding flow valve.

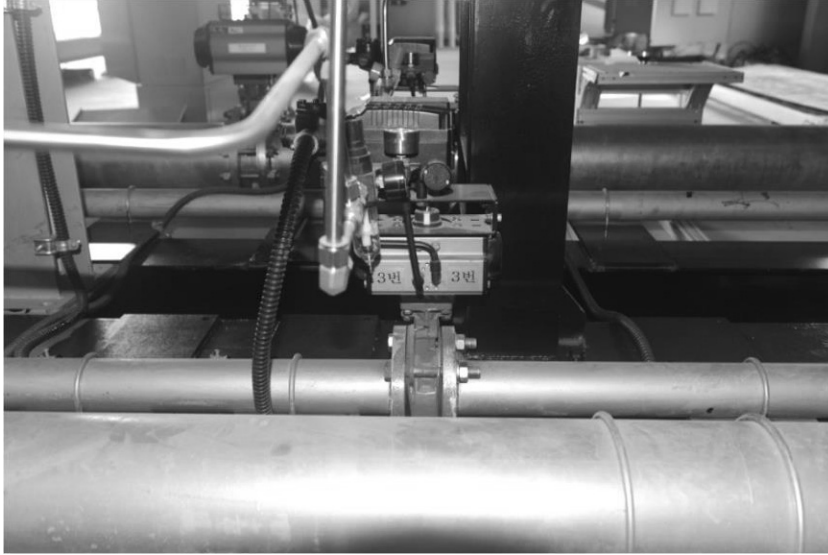


Figure A. 19. Transonic wall flow valve.

Appendix B. Instrumentation

B.1. Blade static tap location

Table A. 1. Blade static tap location

Static hole number	Suction surface, x/Cx	Pressure surface, x/Cx
1	0.19	0.23
2	0.24	0.29
3	0.3	0.35
4	0.36	0.41
5	0.41	0.47
6	0.48	0.53
7	0.54	0.59
8	0.6	0.65
9	0.66	0.71
10	0.73	0.77

B.1. Schlieren method device.



Figure A. 20. Light source & parabolic mirror.

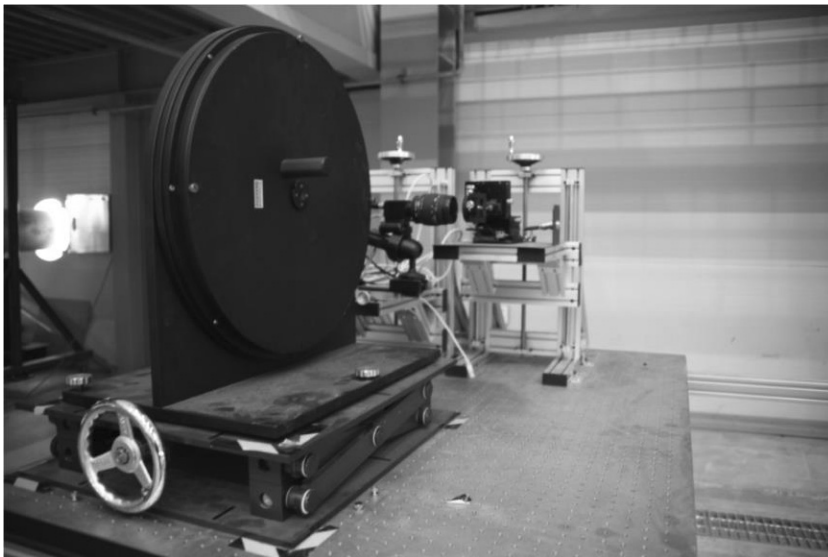


Figure A. 21. Parabolic mirror.

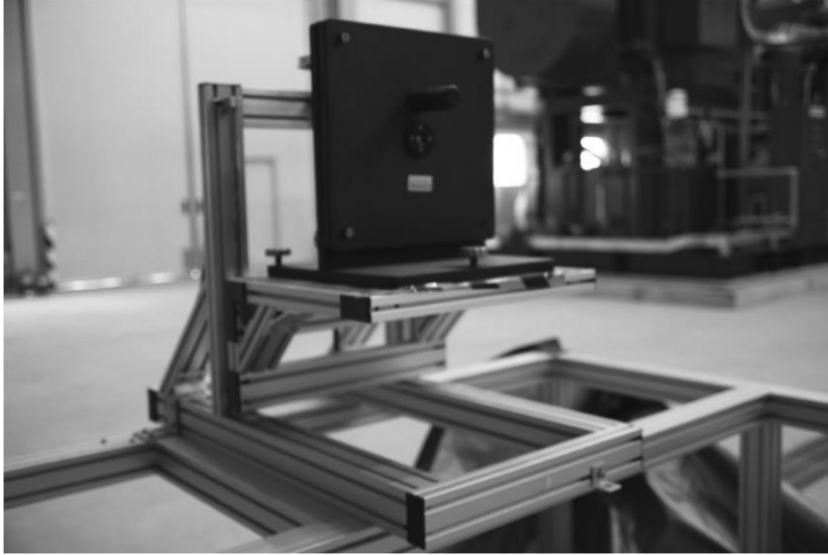


Figure A. 22. Plane mirror.

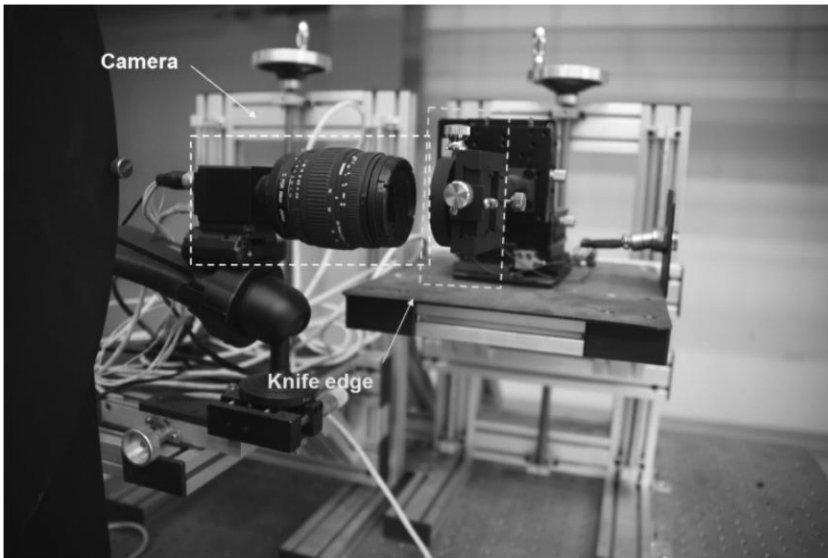


Figure A. 23. Camera & Knife edge.

Appendix C. 3-hole Probe Calibration

C. 1. Flow angle calculation

A 3-hole probe (Product of Vectorflow) is calibrated for three different Mach number (Ma= 0.6, 0.8, 0.95), and for pitch angle from -40° to $+40^\circ$ for 1° intervals. First, for the flow angle changes, flow angle coefficient C_b . Thus, in experiments, flow angle coefficient C_b can be calculated is calculated from the raw data, then flow angle is calculated from the fitting curve. The definition of flow angle coefficient, calibration data and fitting curves for three different Mach numbers are as follows.

$$C_b = \frac{P_2 - P_3}{P_1 - (P_2 + P_3)/2}$$

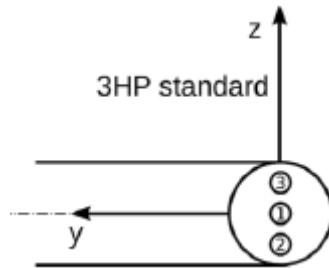


Figure A. 24. 3-hole probe geometry

$P_{1,2,3}$: pressure measured at hole number of 1, 2, 3.

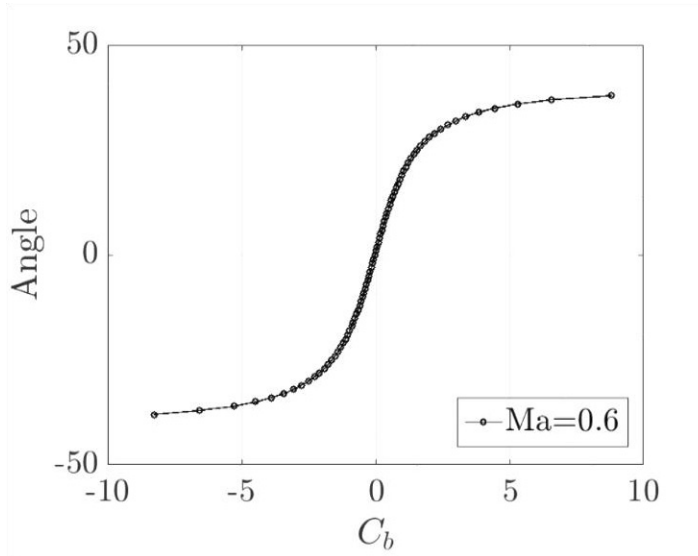


Figure A. 25. Flow angle vs. flow angle coefficient (Ma=0.6).

$$\text{Angle} = 0.2258C_b^5 + 0.0324C_b^4 - 2.9374C_b^3 - 0.2782C_b^2 + 21.835C_b^1 + 0.9235$$

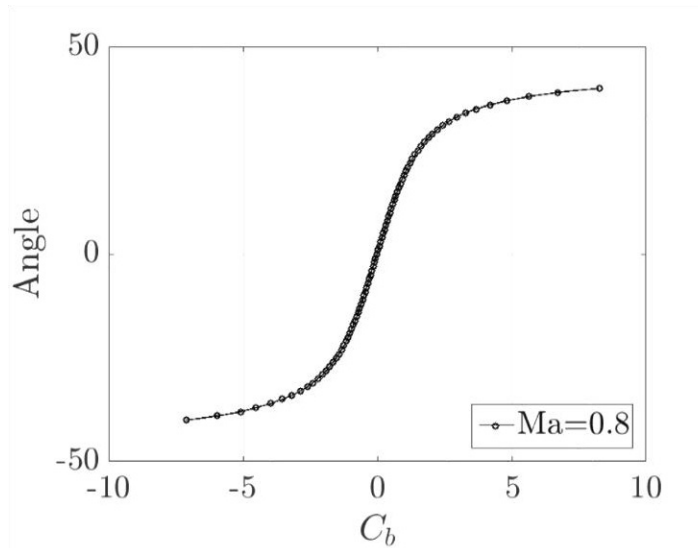


Figure A. 26. Flow angle vs. flow angle coefficient (Ma=0.8).

$$\text{Angle} = 0.1887C_b^5 + 0.0346C_b^4 - 2.4891C_b^3 - 0.3127C_b^2 + 21.246C_b^1 + 0.7717$$

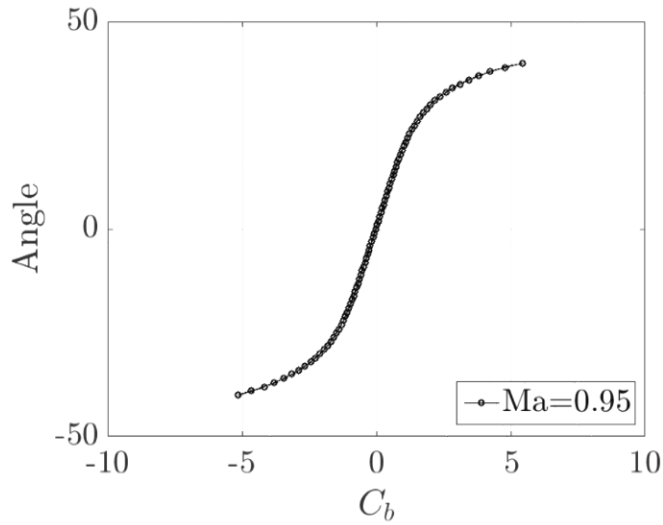


Figure A. 27. Flow angle vs. flow angle coefficient (Ma=0.95).

$$\begin{aligned} \text{Angle} = & -1.4496C_b^3 - 0.167C_b^2 \\ & + 20.477C_b^1 + 0.8923 \end{aligned}$$

C. 2. Total & static pressure calculation

To calculate total pressure, and static pressure, total pressure coefficient C_t and static pressure coefficient C_s are calculated after flow angle coefficient being calculated from the raw data. Each definition, calibration data, and fitting curves are as follows.

Total pressure

$$C_t = \frac{P_1 - P_t}{P_1 - (P_2 + P_3)/2}$$

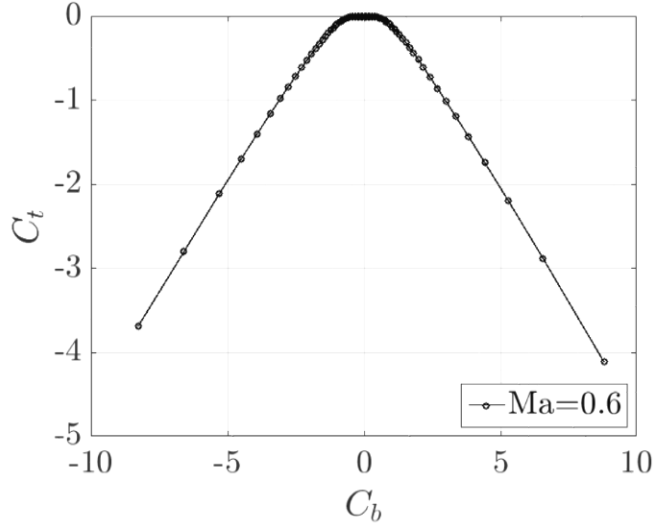


Figure A. 28. C_t vs. C_b ($Ma=0.6$).

$$C_t = 0.0016C_b^6 + 0.0004C_b^5 - 0.0111C_b^4 - 0.0029C_b^3 - 0.1111C_b^2 - 0.0065C_b^1 + 0.0101$$

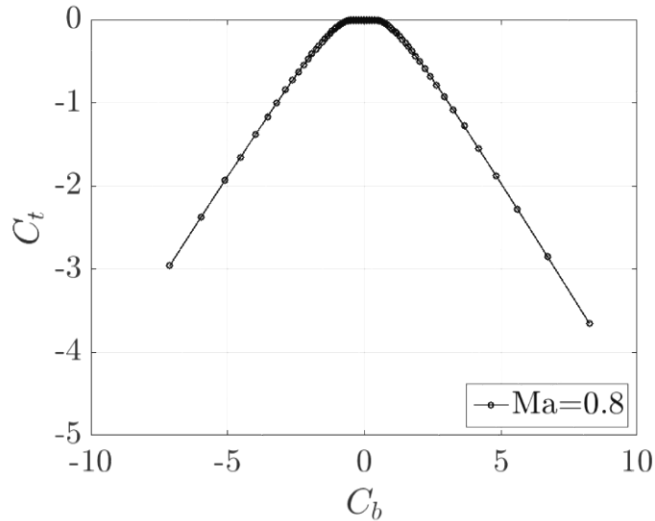


Figure A. 29. C_t vs. C_b ($Ma=0.8$).

$$C_t = 0.0034C_b^6 + 0.0006C_b^5 - 0.023C_b^4 - 0.0037C_b^3 - 0.084C_b^2 - 0.00585C_b^1 + 0.0085$$

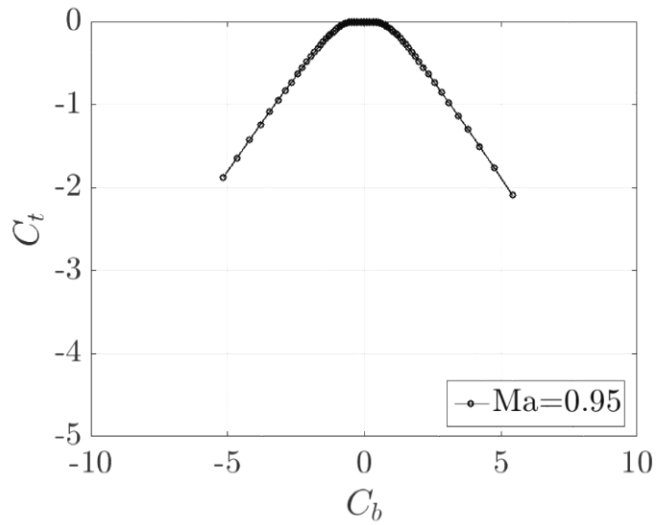


Figure A. 30. C_t vs. C_b (Ma=0.95).

$$C_t = 0.0056C_b^6 + 0.0015C_b^5 - 0.0354C_b^4 - 0.007C_b^3 - 0.0649C_b^2 - 0.0034C_b^1 + 0.0065$$

Static pressure

$$C_s = \frac{P_1 - P_s}{P_1 - (P_2 + P_3)/2}$$

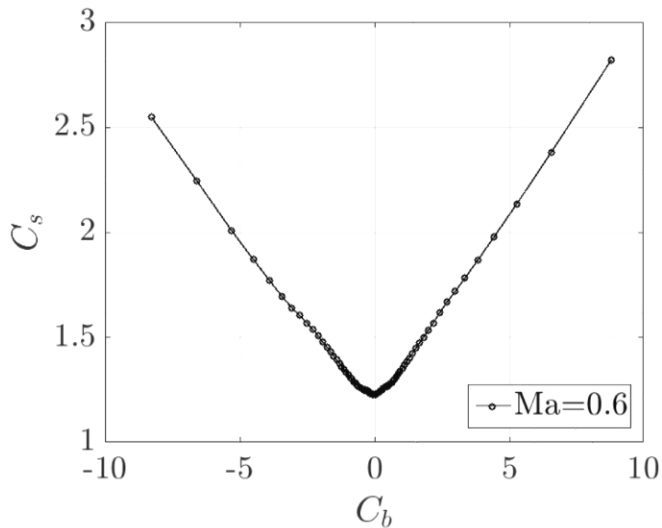


Figure A. 31. C_s vs. C_b (Ma=0.6).

$$C_t = -0.0068C_b^4 - 0.00006C_b^3 + 0.0978C_b^2 + 0.0116C_b^1 + 1.2411$$

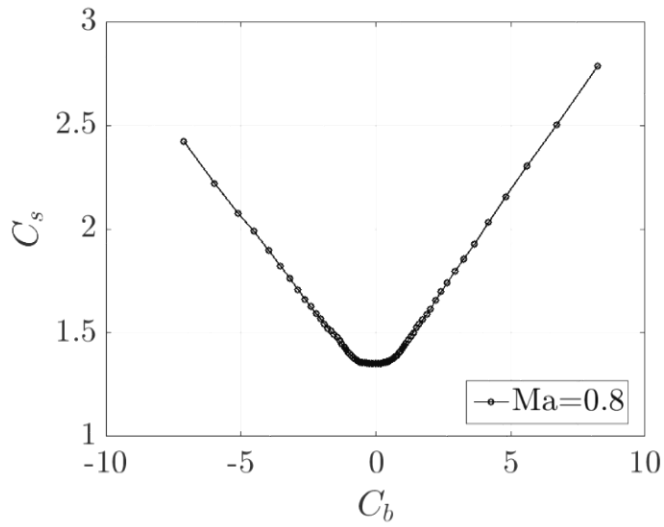


Figure A. 32. C_s vs. C_b (Ma=0.8).

$$C_t = -0.0041C_b^4 + 0.0007C_b^3 + 0.0768C_b^2 + 0.011C_b^1 + 1.3466$$

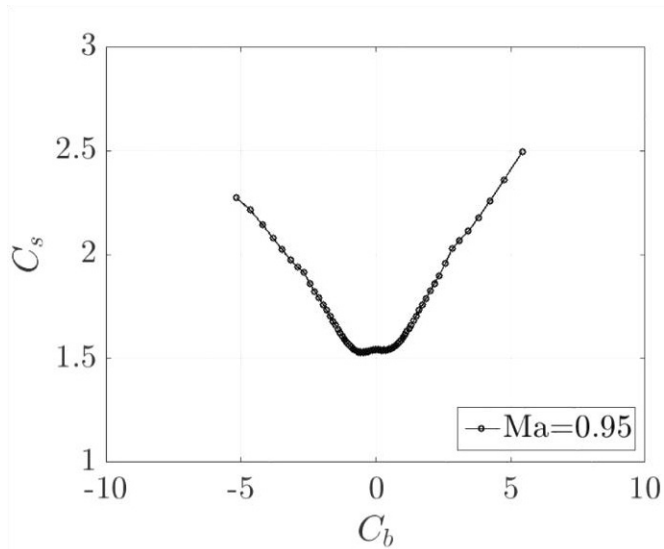


Figure A. 33. C_s vs. C_b (Ma=0.95).

$$C_t = 0.0025C_b^4 - 0.0004C_b^3 + 0.0588C_b^2 + 0.0165C_b^1 + 1.5289$$

Appendix D. Uncertainty Analysis

In calculating the uncertainties of measured variables, Coleman et al.[61] and Taylor [62]'s methods have been adopted. For the Mach number, downstream, pressure coefficient, and loss coefficient, uncertainty analysis has been conducted with following equations. S in the equation represents the pressure sensor accuracy of 0.1kPa.

D.1 Mach number

$$\frac{S_{Ma}}{Ma} = \sqrt{\left(\frac{1}{7(1 - (P_t/P_s)^{-1/3.5})}\right)^2 \left(\frac{S_{P_t}}{P_t}\right)^2 + \left(\frac{1}{7(1 - (P_t/P_s)^{-1/3.5})}\right)^2 \left(\frac{S_{P_s}}{P_s}\right)^2}$$

D.2 Downstream total pressure

$$S_{C_t} = \sqrt{\left(\frac{\partial \beta}{\partial C_b} S_{C_b}\right)^2}$$

$$P_t = P_1 - C_t(P_1 - \bar{p})$$

$$\bar{p} = (P_2 + P_3)/2$$

$$\frac{S_{P_t}}{P_t} = \frac{1}{P_t} \sqrt{\left(\frac{\partial P_t}{\partial P_1} S_{P_1}\right)^2 + \left(\frac{\partial P_t}{\partial C_t} S_{C_t}\right)^2 + \left(\frac{\partial P_t}{\partial \bar{p}} S_{\bar{p}}\right)^2}$$

D.3 Downstream Static pressure

$$S_{C_S} = \sqrt{\left(\frac{\partial \beta}{\partial C_b} S_{C_b}\right)^2}$$

$$P_S = P_1 - C_S(P_1 - \bar{p})$$

$$\bar{p} = (P_2 + P_3)/2$$

$$\frac{S_{P_S}}{P_S} = \frac{1}{P_S} \sqrt{\left(\frac{\partial P_S}{\partial P_1} S_{P_S}\right)^2 + \left(\frac{\partial P_S}{\partial C_S} S_{C_S}\right)^2 + \left(\frac{\partial P_S}{\partial \bar{p}} S_{\bar{p}}\right)^2}$$

D.4 Static pressure coefficient

$$\frac{S_{C_p}}{C_p}$$

$$= \sqrt{\left(\frac{(-P + P_{S1})}{(P_{t1} - P_{S1})(P - P_{S1})} S_{P_{t1}}\right)^2 + \left(\frac{1}{P - P_{S1}} S_{C_S}\right)^2 + \left(\frac{(P - P_{t1})}{(P_{t1} - P_{S1})(P - P_{S1})} S_{P_{S1}}\right)^2}$$

D.5 Loss coefficient

$$\frac{S_{Y_p}}{Y_p} = \sqrt{\left(\frac{(P_{t2} - P_{S1})}{(P_{t1} - P_{S1})(P_{t1} - P_{t2})} S_{P_{t1}}\right)^2 + \left(\frac{1}{P_{t1} - P_{t2}} S_{P_{t2}}\right)^2 + \left(\frac{1}{P_{t1} - P_{S1}} S_{P_{S1}}\right)^2}$$

Appendix E. Axial Velocity Density Ratio

The Axial Velocity Density Ratio (AVDR) represents the stream tube contraction which comes from the sidewall boundary layer growth. The AVDR is affected by the incoming boundary layer thickness, blade aspect ratio, inlet Mach number, inlet flow angle, and etc. AVDR affects the compressor flow field in various way, such as flow turning, pressure ratio, shock-boundary layer interaction, shock location, and etc. For example, Kusters (compressor cascade flow with strong shock wave/boundary layer interaction, AIAA, 1998) measured the AVDR effects on the loss coefficient at Mach number 1.5 condition, and found that the loss coefficient decreased from 0.136 to 0.109 as AVDR increase from 0.94 to 1.04. Thus, in compressor cascade experiments, keeping the AVDR value constant is important to see the independent effects from AVDR. The AVDR definition as a follow.

$$AVDR = \frac{V_{ax,2}\rho_2}{V_{ax,1}\rho_1}$$

The inlet value of $V_{ax,1}$, ρ_1 are calculated by isentropic equation using the measured values of total pressure $P_{t,1}$, total temperature $T_{t,1}$, and inlet static pressure $\overline{P_{s,1}}$. First, Mach number is calculated from the equation A.2, and the static temperature is calculated from the equation A.3. Then, the inlet density ρ_1 and inlet axial velocity are calculated by A.4, and A.5 each.

$$\frac{P_s}{P_t} = \left(1 + \frac{\gamma - 1}{2} Ma^2\right)^{\gamma/1-\gamma}$$

$$\frac{T_s}{T_t} = \left(1 + \frac{\gamma - 1}{2} Ma^2\right)^{-1}$$

$$\frac{\rho_s}{\rho_t} = \left(1 + \frac{\gamma - 1}{2} Ma^2\right)^{1/\gamma}$$

$$V_{ax,1} = Ma\sqrt{\gamma RT_s} \cdot \cos \theta$$

The outlet value of $V_{ax,2}$, ρ_2 are calculated by the same equations, but its values are measured via 3-hole probe. 3-hole probe gives pitch-wise distributions of static pressure $P_{s,2}$, total pressure $P_{t,2}$, and flow angle α_2 . Thus, $V_{ax,2}$, ρ_2 can be calculated at each point, then, averaged with mass. The mass averaged value is calculated with following equation, A.6.

$$\bar{\phi}^{mass} = \frac{\int_0^S \rho V \phi dS}{\int_0^S \rho V dS}$$

Where, $\bar{\phi}^{mass}$ represents a mass average value of a scalar ϕ .

Appendix F. Rayleigh Flow

Rayleigh flow refers to frictionless, non-adiabatic flow through a constant area duct where the effect of heat addition or rejection is considered. Therefore, the heat addition effects from the condensation on the flow parameters, static/total pressure, Mach number and etc., can be analyzed by Rayleigh flow equation. The Rayleigh equation is derived by differential equations, and the results of static/total pressure P , P_t , total temperature T_t , entropy s are represented as follows.

$$\frac{dT_t}{T_t} = \frac{\Delta q}{c_p T_t}$$

$$\frac{dP_t}{P_t} = -\frac{\gamma}{2} Ma^2 \frac{dT_t}{T_t}$$

$$\frac{dP}{P} = \frac{-\gamma Ma^2}{1 + \gamma Ma^2} \frac{dMa^2}{Ma^2}$$

$$\frac{ds}{c_p} = \frac{1 - Ma^2}{1 + \gamma Ma^2} \frac{dMa^2}{Ma^2}$$

Heat addition effects on these variables can be summarized in Table A.2 for subsonic/supersonic flow.

Table A. 2. Heat addition effects on flow properties

Variable	Subsonic	Supersonic
T_t	↑	↑
P_t	↓	↓
P	↓	↑
s	↑	↑

Appendix G. The effects of vapor mass reduction on the static pressure field

During the condensation, vapor is condensed, thus, static pressure decreases by amount of the vapor mass reduction. In this section, the effects of vapor mass reduction on the static pressure field are discussed. Following the Rayleigh equation, the effects of vapor mass reduction and heat addition on the static pressure field are calculated and compared. For the Mach number 1.1 and relative humidity of 53% condition (as in the experiment), control volume is set and it is assumed that 5% of vapor is condensed in the control volume. The calculation results are listed in Table A.4. Due to the condensation, static pressure increases about 8 kPa, however, the static pressure reduction due to the vapor mass reduction is only about 0.07 kPa. Therefore, it can be concluded that the effects of condensation on the static pressure field are not mainly come from the effects of vapor mass reduction but heat addition effects.

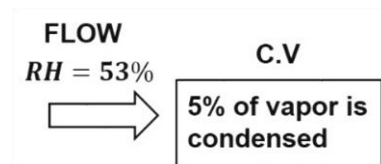


Figure A. 34. Control volume.

Table A. 3. The effects of condensation on the flow properties

	Inlet	Outlet
P_t	210 kPa	209.4 kPa
T_t	310 K	311.2 K
M	1.1	1.06
P_s	98 kPa	103 kPa
T_s	249 K	253 K
P_v	1.4 kPa	

Appendix H. Water injection rate

During the experiments, to set the relative humidity conditions, water has been injected upstream of the settling chamber in the form of mist. Therefore, total mass flow rate is increased and it can affect the cascade flow field, especially, shock location can be shifted to downstream. Following the Steinert et al. [59], to shift the shock location $0.15C_x$ downstream (as in the EXP results), about 10% of additional mass flow rate is required. However, as listed in Table A.3, in the experiments, the maximum water injection rate is about 0.6% of air mass flow rate. Therefore, it can be concluded that the effects of additional mass flow rate on the cascade flow field are negligible.

Table A. 4. Water injection rate

RH (%)	Water injection rate (kg/s)	Water-air ratio ($M_{water}/M_{air} \times 100$)
20	0	-
32	0.010	0.1%
42	0.020	0.2%
45	0.030	0.3%
49	0.045	0.45%
53	0.060	0.6%

Appendix I. Limitations in capturing deviation distribution

In Chapter 6 numerical results, CFD does not well capture the experimental deviation distribution in two respects - 1) low peak and low intensity in the wake region and 2) low deviation values in the main passage region. Therefore, to improve the prediction, additional CFD calculations have been conducted considering the following possibilities – i) fine mesh in the shock location (see Fig. A. 34, reconstructed mesh) can capture the shock-induced boundary separation, and deviation distribution well and ii) from the slight increase of incidence, deviation distribution can be well matched. Figure A. 35 shows the deviation distributions for the experimental data, and CFD results of reference mesh, new mesh, and high incidence case ($i = +6^\circ$). For the all the CFD cases, CFD results show low intensity of peak and low in the wake region, and low deviation values compared to the EXP results. Therefore, the author leave it as the limitation of CFD prediction.

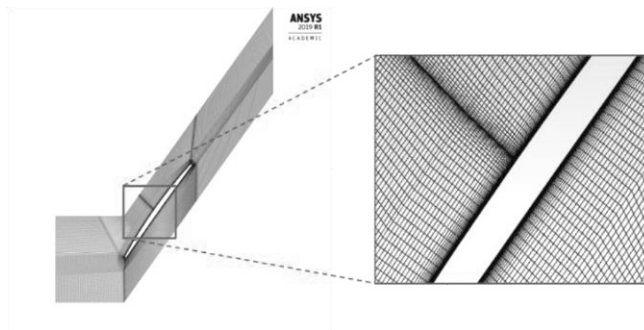


Figure A. 35. Re-constructed mesh.

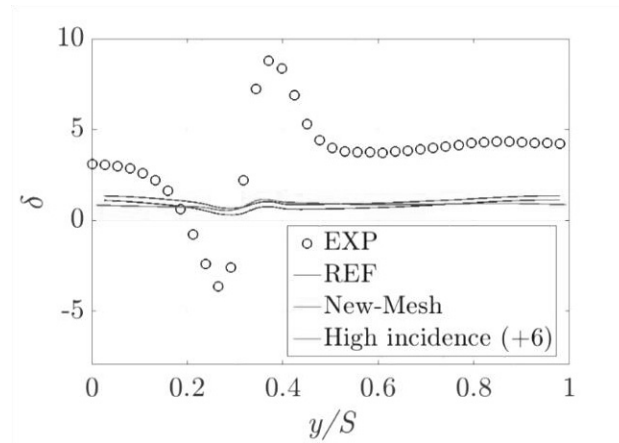


Figure A. 36. Deviation distributions for the EXP, and CFD results of reference mesh, new-mesh, and high incidence angle ($i = +6^\circ$).

요약 (국문초록)

상대습도 변화에 따른 천음속 압축기 캐스케이드의 공력 특성 변화

서울대학교 대학원

기계항공공학부

기계전공

이재민

습한 환경에서 작동하는 가스터빈의 경우, 그 성능이 설계 값과 다르게 나오는 것이 잘 알려져 있다. 공기중의 수증기 함량에 따른 공기 물성치 변화, 그리고 엔진 입구에서의 응축 현상에 따른 입구 온도 증가를 그 원인으로 하는 연구들이 많이 수행되었지만, 습한 환경에서의 압축기 내부의 유동장 변화에 대한 연구는 미미한 실정이다. 따라서 본 연구는 습한 환경에서 작동하는 천음속 압축기의 유동장 변화를 분석하기 위하여 수행되었다. 천음속 캐스케이드 장비를 설계하여 6개 상대습도 (20, 32, 43, 45, 49, 53%), 마하수 1.1, 인시던스 $+5^\circ$ 조건에 대하여 실험 및 유동해석을 수행하였고, 상대습도 변화에 따른 캐스케이드 공력 성능의 변화를 블레이드 압력계수 분포, 출구유동 편차각, 그리고 손실계수 변화로 비교하여 나타냈다.

상대습도가 증가함에 따라 블레이드 흡입면의 압력 계수가 증가하는데, 이는 블레이드 흡입면에서 유동이 가속됨에 따라 발생한 응축 현상에 기인한다. 응축이 발생함에 따라 방출되는 잠열로 인하여 충격파 상류의 압력이 증가하여 압력 계수가 증가한 것이며, 이는 또한 충격파를 하류로 이동킨다. 출구 유동편차각의 경우 상대습도 변화에 별다른 영향을

받지 않는 것으로 나타났다. 하지만, 이는 레퍼런스 조건에서 (상대습도 20%) 블레이드 표면에서의 유동 박리가 무시할 만큼 작아 응축 현상에 의한 유동 박리 감소 현상, 그리고 이에 의한 출구 유동편차각 감소현상이 미미하게 나타났기 때문이다. 손실계수의 경우 상대습도가 증가함에 따라 증가하였고, 53% 상대습도 조건에서 최대 29%의 증가를 보였다. 이는 응축과정에서 발생하는 잠열은 충격파 전단의 마하수를 낮춰 충격파의 손실을 줄이지만, 열 공급 자체로 인한 엔트로피 증가가 더 큰 폭으로 발생하기 때문이다.

.....

주요어 : 천음속 압축기, 캐스케이드, 공력 성능, 습도, 비평형 응축,

학 번 : 2013-20697

감사의 글

지난 6년 반동안 많은 분들의 고마움이 있었습니다. 우선 항상 응원해주시고 격려해주신 부모님께 감사드립니다. 긴 시간 학생 신분으로써 부모님께 의지할 수 있었기 때문에 학업을 무사히 끝맺을 수 있었습니다. 지난 감사의 말을 이 자리를 빌어 전합니다.

교수님께 감사드립니다. 짧은 글로 어찌 교수님의 감사함을 다 전할 수 있을까요. 언제나 제 편에 서서 지도해주시고 도와주시는 마음에 항상 감사했고 든든했습니다. 그동안의 가르침 잘 기억하고 이어나가겠습니다.

다음으로, 지금 이 졸업논문을 작성할 수 있게 도와주신 분들에 대한 고마움이 매우 큼니다. 지금의 실험 설비가 있기까지 많은 고생을 함께 나눈 진욱이형 고맙습니다. 언젠가 형이 가볍게 던진 한마디가 지금의 제 졸업논문 주제가 되었네요. 다음으로, 주현이 형에게 큰 감사를 드립니다. 본인의 일도 아닌데, 마지막 실험하는 날까지 저를 참 많이 도와주셨어요. 실험 준비며 장비 대여까지 어느 하나 형의 도움 없이 진행된 일이 없네요. 감사합니다. 그리고 김명완 과장님, 과장님께도 큰 감사의 인사를 드립니다. 어찌보면 그날 외부인인 저를 이뻐해주시고, 어려움이 생길때마다 도와주신점에 너무 감사했습니다. 마지막으로 해미까지 내려와서 실험 도와준 연구실 동생 지호, 홍성이에게 고마운 마음을 전합니다.

이 외에 많은 분들의 격려와 지원이 제게 큰 힘이 되었습니다. 대학원 초반, 함께 많은걸 공유했던 친구 원석이와 병윤이형, 두 분의 존재만으로도 많이 의지되었고 위로가 되었습니다. 그리고, 항상 든든한 분이셨던 유일이형, 원준이형, 많은 시간 함께 했던 영모형과 지훈이, 유학가기 전까지 큰 활력소가 되어준 해림누나까지, 모두들 감사했고 그립네요. 마지막으로 TML 연구실원들 모두에게 감사의 마음을 하나하나 전합니다. 모두 감사합니다.